Thermal history of Pyroclastic Density Currents and their deposits

A dissertation submitted to:

UNIVERSITA' DEGLI STUDI ROMA TRE

Scuola dottorale in Scienze della Terra

for the degree of

Doctor of Sciences

presented by

TROLESE MATTEO

Prof. Guido Giordano, Advisor — Università degli Studi Roma Tre

Dr. Tomaso Esposti Ongaro, Co-Advisor — Istituto Nazionale di Geofisica e Vulcanologia, Pisa

2017

Stromboli viewed from the east (750 m).

Better to be approximately correct than precisely wrong

Warren Buffet

ACKNOWLEDGMENTS

During the course of my PhD there have been many people who have helped me, without whom this thesis would not have been written, and I would like to express my gratitude to all of them.

First and foremost, I would like to thank my chief supervisor Prof. Guido Giordano for his advise, patience and encouragement through the research process. He was always available to talk to me about volcanology, advise me on all aspects of life always staying eye-to-eye and approaching supervision as a form of friendship, rather than merely academic interaction. I would also like to thank him for giving me additional funding for field work and international conferences. I also extend my deep gratitude to my second supervisor Dr. Tomaso Esposti Ongaro for introducing me to the world of numerical simulations always answering all sorts of questions and for the many insightful discussions and suggestions along the way. I must also express my immense thanks to Dr. Matteo Cerminara for providing me with all the support that I needed and for being the best sounding board anyone could ask for; I simply can not thank you enough.

Thanks to Prof. Massimo Mattei, Prof. Francesca Cifelli and Dr. Aldo Winkler for introducing me to the world of magnetism and for their fundamental role in interpreting the data. A big thank is for Prof. Jean-Christophe Komorowski for allowing me to work on his samples and for his kind support and encouragement. I would also like to thank Prof. Sveva Corrado for giving me the possibility to work at ALBA-Lab in complete freedom.

Thanks to all those who helped and advised me academically during my time at University of Roma Tre, especially Prof. Francesca Funiciello (thanks for the hard-disk!!!), Dr. Fabio Corbi and Dr. Alessandro Vona.

I must also acknowledge the support I have received from my amazing fellow PhD students and friends, Gabriele Amato, Gaia Siravo, Marco Spadi and Stefano Urbani. Having friends like you guys is a great gift. I wish you all the best in your future.

I am eternally grateful to my family for all their support and for giving me the tools to believe in myself and in what I do.

And last, but by no means least, I don’t have the worlds for how grateful I am to Silvia Brizzi for putting up with me throughout this. I could not have done any of this without you, and I am only where I am today because of you!! You are everything I could have asked for and so much more besides. Thank you, I love you.

Summary

Pyroclastic density currents (PDCs) are among the most devastating and fascinating type of explosive volcanic activity. Our capacity to observe their internal structure is prevented by their extremely dangerous nature. The complex thermo-fluid dynamics of PDCs thus remains unclear and highly debated. While velocity and concentration fields have been widely investigated to assess PDCs dynamic force (i.e. dynamic pressure) and the respective damages to the buildings, much less attention has been dedicated to the understanding of the thermal evolution of PDCs from their generation to their deposition. However, it is high time for exploring how the heat transport process occurs in their interior, as this knowledge would have great implications on future volcanic hazards. In this thesis, I combine field-based analysis and numerical models to shed light on the mechanisms influencing the heat exchange experienced by PDCs from their genesis to their emplacement. To this aim, detailed reconstructions of the thermal architecture of PDC deposits are provided based on two different methodologies. Field case studies were selected to cover the broadest range of parent PDCs, in terms of volume (from very small to several tens of cubic km), generation mechanisms (column collapse and lateral dome collapse), fragmentation mechanisms and related grain size distribution (magmatic vs phreatomagmatic vs dome explosion), magma chemistry (mafic to intermediate), topographic interactions (confined vs unconfined).

The emplacement temperature of large-volume, caldera-forming ignimbrites erupted at Colli Albani volcano were determined with the Thermal Remanent Magnetization analysis on both lithic and juvenile clasts. Results show that all the magmatic ignimbrites were deposited between the maximum blocking temperature of magnetic minerals within the clasts (600 – 630°C) and the glass transition temperature (ca. 710°C), while the phreatomagmatic one was emplaced at lower temperature (200 – 400°C). Each ignimbrite shows a significant thermal homogeneity across its areal extent, which is also maintained across topographic barriers. The outcomes confirm the efficiency of magma-water interaction as one of the eruptive mechanisms decreasing the thermodynamic state of the pyroclastic

mixture compared to its magmatic counterpart without, though, affecting significantly the mobility of PDCs, nor their tendency to retain the initial heat along flow. In addition, this work highlights the relevant role of a sustained mass discharge rate as key factor for explaining the overall conservation of thermal energy across the areal extent of the deposits, regardless of the grain size, concentration and initial temperature (i.e. magmatic vs phreatomagmatic) of their parental currents.

The optical analysis of charcoal fragments provided the emplacement temperatures of the high-energy PDC deposits generated during the paroxysmal dome explosion at Merapi volcano on 5 November 2010. Results show that the minimum charring temperature, which ranges from 240°C to 320°C, is maintained throughout most of the impact area of PDCs. This suggests that the flow transport system was thermodynamically isolated along the path, despite its dynamics evolved as it propagated over a complex terrain. The low thermal signal of PDC deposits generated by this eruption, likely characterized by high temperatures due to the high extrusion rates building up the dome, may be then associated to a sudden drop occurring during the inferred blast-like process.

Field-based observations have shown the important role of the eruptive mechanism on the thermal character of PDCs. For this reason, 3D numerical simulations were performed to unravel whether distinct thermal imprints can be recognized in PDCs depending on different column collapse regimes. Results show that the initial temperature of PDCs well correlates with the percentage of collapse, with a maximum decrease of 45% of the starting magmatic temperature, independently of the mass flux. This provides an innovative and previously not explored perspective on the large variability of PDC' emplacement temperatures observed in the field.

In conclusion, this thesis shows that at least two different thermal domains characterize PDCs, as heat transfer between the gas-particle mixture and the external environment has been shown to be essentially very limited during flow propagation, but very efficient at the source.

Contents

Introduction

Motivation and objectives

Pyroclastic density currents (PDCs) are one of the most spectacular and poorly understood phenomena associated with explosive volcanic eruptions. They represent a serious hazard to population and infrastructure surrounding volcanoes. Their devastating impact on the humankind comes from their ability to transport great masses of hot particles and gas over great distances at high velocities (up to 300 m/s), burning and burying enormous areas in a few minutes (Druitt, 1998). In recent history, the 1815 Tambora eruption (VEI 7) was responsible for more than 60,000 deaths (most of which are attributed to PDCs) on Sumbawa and neighboring islands (Auker et al., 2013). The 1902 eruption of Mount Pelée (VEI 4) in Martinique generated PDCs that invaded the city of St. Pierre causing nearly 30,000 victims (Lacroix, 1904). At Merapi, the 1930 eruption results in nearly 1,400 fatalities (Van Bemmelen, 1949), while PDCs produced throughout the 2010 event killed more than 200 people (Jenkins et al., 2013). Such shocking events represent just a handful of the fatal disasters connected with explosive volcanic eruptions worldwide, and the continuous expansion of urban settlements around active volcanoes increases the number of people potentially affected by their hazard (Chester et al., 2001). Given the great destructive potential posed by PDCs and their rather high frequency of occurrence in volcanoes around the world, the understanding of the mechanism by which PDCs form and propagate is on a first-order level for scientists who want to develop strategies for volcanic disaster risk reduction.

In the last half-century, huge strides have been made in understanding the complexity of PDCs dynamics, especially through multidisciplinary investigations and direct observations made during and immediately after PDC-forming eruptions (e.g. Hoblitt et al., 1981; Newhall and Panungobayan, 1993; Druitt and Kokelaar, 2002; Komorowski et al., 2013). Thanks to hundreds of studies following

the 1980 eruption of Mount St. Helens, the 1991 outburst of Mount Pinatubo and the 1997-99 explosive activity of Soufrière Hills Volcano on Montserrat, we have developed a sophisticated understanding of the mechanisms that lead to the conditions for steady plume-forming eruptions, collapse and PDC formation. Enough is known to surmise that PDCs encompass a huge spectrum of flow transport regimes and multiphase gas-particle interactions, spanning from fast and highly turbulent dilute current to slow and dense granular flow, which produce a wide variety of deposit characteristics (Branney and Kokelaar, 2002; Dufek, 2016; Sulpizio et al., 2014). Given the high unpredictability and dangerousness of PDCs, and our inability to observe the evolution of the flow properties (i.e. particle concentration, velocity and temperature) inside the current, most of our knowledge derives from integration of field-based observations of their deposits, analogue experiments and numerical modeling. Studies of the geological record throughout the characterization of PDCs' deposits are essential to infer the transport and emplacement processes of these currents, as well as to define the eruptive history of a particular volcano, although this record is usually incomplete. However, such inferences that come from the fieldwork need to be evaluated experimentally by numerical and analog approaches, which, at the same time, must be validated by the deposits' characteristics.

Although great efforts have been made on the study of PDCs (from their generation to their emplacement), their dynamics, and consequently their related hazard, still remain open issues (Sulpizio et al., 2014). Future progress will be enhanced by the continuous collection of important quantitative field-based data, thus providing the fundamental evidences that would be critical for testing and improving the physical models. Needless to say, new data will surely reveal further fascinating questions about the flow characteristics that will stimulate the study of physical problems as yet unexplored. Since we are unable to take real-time measurements of the opaque interior of PDCs, the spatiotemporal evolution of the flow properties can be indirectly obtained by looking at different proxies within the deposits and/or at the magnitude of the damage. In particular, much attention has been given in quantifying the velocity and concentration fields of PDCs, as on these

quantities relies the estimation of their dynamic force (i.e. dynamic pressure), which is an important prerequisite for assessing their destructive power to the buildings (e.g. Jenkins et al., 2013; Pittari et al., 2007). Recently, by using a large-scale experimental set-up, Breard and colleagues (Breard et al., 2016; Lube et al., 2015) were able to study in detail the complex velocity and density stratifications that occur inside high-density cold gravity currents. Their results have crucial implications for PDCs hazard assessment.

However, much less work has focused on understanding the thermal evolution of PDCs, from their generation to their emplacement. Like the dynamic pressure, it is essential to incorporate the thermal factor in our strategies of volcanic hazard mitigation. In general, most of the heat loss of the pyroclastic mixture is believed to be associated with the amount and efficiency of air entrainment during both the collapse of the eruptive column (for those currents that form in this way) and the flow phase, as well as with the ingestion of cold objects such as lithic clasts, water and vegetation (e.g. Bursik and Woods, 1996; Cioni et al., 2004; McClelland et al., 2004). Nonetheless, according to the emplacement temperature data either directly measured or retrieved from various methods, PDC deposits show a huge spectrum of thermal states that seems to be independent of their lithofacies, chemistry and grain size distribution (Walker, 1983). At the low end of the spectrum are PDC deposits that record emplacement temperatures much lower than the magmatic temperature. As an example, Zanella et al., 2015 found that the temperatures of all the small-volume PDC deposits emplaced in the last 22 ka of activity at Somma – Vesuvius mainly are within the 250 – 370°C range (with lower value of about 100°C), almost irrespective of their contrasting sedimentological features, eruptive mechanisms (i.e. magmatic and phreatomagmatic; partial or total collapse of the eruptive column), and distance from the vent. On the other hand, some large-volume PDC deposits are extensively welded through much of their extent (Best et al., 2013), whereas others remain above the Curie temperature (Lesti et al., 2011). Knowing the thermal state of large-volume PDCs can give some important clues about the flow mechanism emplacing such deposits, since direct observations are not available yet. In addition, some proximal PDC deposits exhibit temperatures of emplacement that are

far below those of the eruptive magma, while other deposits were found at high temperature even in distal localities. Assessing where and how the temperature decrease takes place can help the understanding of not only the flow dynamics but also the early contribution of the eruptive processes.

The aim of this thesis is to enhance our current understanding of the thermal evolution that characterize the complex physics of PDCs through their entire process (i.e. from their genesis to their emplacement). The main purpose of this work is to evaluate how the temperature associated with PDCs can be used as a tool that has the potential to highlight both their eruptive and transport history. To this aim, two main research approaches have been applied. The first approach consists in determining the temperature of emplacement of two case studies by using two different methodologies, namely the analyses of the Thermal Remanent Magnetization of lithic clasts and of the Reflectance of charcoal fragments. We compare case studies that encompass the widest possible range of parent PDCs, by studying: (1) large-volume, dense, caldera-forming ignimbrites related to magmatic and phreatomagmatic eruptions of the Colli Albani volcano; and (2) small-volume, dilute, dome-collapse ignimbrites emplaced during the 2010 Merapi eruption. This research strategy aims at answering the following main questions:

Questions: *What are the patterns of thermal decay within PDCs? What is the role, if any, of the topographic interactions on the flow thermal properties? How do different eruptive mechanisms reflect on PDCs temperature?*

Objectives: To study systematically the changes in emplacement temperature as a function of the distance from the source, verifying the feedback between topography and thermal history. To build on the available dataset of PDC deposits temperature. To understand and compare the thermal properties of PDCs related with different eruptive mechanisms.

The second part of this thesis is focused on unravelling the effects of different column collapse regimes (and potentially different thermal regimes) on the thermal evolution of the eruptive mixture and, in particular, on the initial temperature of PDCs at their formation. A series of 3D numerical

simulations are performed to systematically explore the collapse region in order to answer at the questions listed below.

Questions: *How do different collapse regimes affect the initial temperature of PDCs? If so, does this effect provide an explanation for the huge spectrum of the emplacement temperatures observed in PDC deposits?*

Objectives: To analyze the temperature field of the ejected mixture during the jet and collapse phases in order to quantify the temperature of the collapsing mass, which provides the initial thermal condition of the PDC.

Thesis outlines

This thesis consists of four chapters. In Chapter 1, the thermal behavior of four historical large-volume PDC deposits of the Colli Albani volcano, central Italy, is discussed in the form of a short-length research article. Here, the aim is to compare the emplacement temperatures of magmatic and phreatomagmatic ignimbrites, similar in volume (VEI 6-7) and chemistry, focusing on their thermal spatial variations and on the effect of topographic barriers on the temperature of their parental currents. The temperature distributions derived from the paleomagnetic results have been interpreted using the theoretical model of Doronzo (2012) and Doronzo et al. (2016), which classifies PDCs based on their flow energy (i.e. forced vs inertial regimes) rather than the most commonly used flow concentration (i.e. dilute vs concentrated). This chapter highlights the importance of a sustained mass discharge rate as a key controlling mechanism for explaining the overall conservation of thermal energy across the areal extent of the deposits, regardless of the grain size, concentration and initial temperature (i.e. magmatic vs phreatomagmatic) of their parental currents.

Chapter 2 presents new determinations of the emplacement temperatures of the high-energy PDCs produced during the explosive activity at Merapi on 5 November 2010. The optical analysis on

charcoal fragments is used for this case study to retrieve emplacement temperatures information that aim at assessing (1) if changes of the flow dynamics due to topographic conditions can be correlated to changes of the flow temperature, and (2) how the blast produced by dome collapse reflects in the thermal imprint of the resulting PDCs. It is shown that charring temperatures do not seem to be modulated by the marked topography characteristics, notwithstanding the strong interaction between PDCs and the terrain over which they flowed. This result highlights that the blast process played a major role in determining the strong temperature drop of the associated PDCs, which subsequently were able to maintain their inherited thermal state at source over their flow path.

The effects of different collapse regimes on the initial temperature of PDCs is considered in Chapter 3. There, a numerical study of the eruption column is presented in the form of a short-communication research article. It is shown, that the collapse regime strongly influences the thermal history of collapsing columns, where the percentage of collapse is directly and linearly correlated with the initial temperature drop of the pyroclastic mixture during the jet and collapse phases. These results provide an innovative and previously not explored perspective on the large variability of emplacement temperatures seen in PDC deposits.

Finally, in the last section (Chapter 4) this thesis is concluded with summary of the data presented and a discussion that links the results in a comprehensive overview of the advancements that this thesis has achieved in the understanding of PDC thermodynamics. Some suggestions for future research are presented as well.

Chapter 1

Forced transport of thermal energy in magmatic and phreatomagmatic large volume ignimbrites: paleomagnetic evidence from the Colli Albani volcano, Italy

Note - This Chapter has been published as:

Trolese, M., Giordano, G., Cifelli, F., Winkler, A., Mattei, M., 2017. Forced transport of thermal energy in magmatic and phreatomagmatic large volume ignimbrites: paleomagnetic evidence from the Colli Albani volcano, Italy. Earth Planet. Sci. Lett. 478, 179-191. doi:10.1016/j.epsl.2017.09.004.

Abstract: Few studies have detailed the thermal architecture of large-volume pyroclastic density current deposits, although such work has a clear importance for understanding the dynamics of eruptions of this magnitude. Here we examine the temperature of emplacement of large-volume caldera-forming ignimbrites related to magmatic and phreatomagmatic eruptions at the Colli Albani volcano, Italy, by using thermal remanent magnetization analysis on both lithic and juvenile clasts. Results show that all the magmatic ignimbrites were deposited at high temperature, between the maximum blocking temperature of the magnetic carrier (600 – 630°C) and the glass transition temperature (about 710°C). Temperature estimations for the phreatomagmatic ignimbrite range between 200 and 400°C, with most of the clasts emplaced between 200 and 320°C. Because all the investigated ignimbrites, magmatic and phreatomagmatic, share similar magma composition, volume and mobility, we attribute the temperature difference to magma-water interaction, highlighting its pronounced impact on thermal dissipation, even in large-volume eruptions. The homogeneity of the deposit temperature of each ignimbrite across its areal extent, which is maintained across topographic barriers, suggests that these systems are thermodynamically isolated from the external environment for several tens of kilometers. Based on these findings, we propose that these large-volume ignimbrites are dominated by the mass flux, which forces the lateral transport of mass, momentum, and thermal energy for distances up to tens of kilometers away from the vent. We conclude that spatial variation of the emplacement temperature can be used as a proxy for determining the degree of forced-convection flow.

1.1. Introduction

Quantitative estimation of the deposit temperature of pyroclastic density currents (PDCs) is commonly derived by paleomagnetic methods, which are based on the progressive thermal demagnetization of lithic and juvenile clasts embedded within the deposits (e.g. Bardot and McClelland, 2000). The emplacement temperatures of PDCs depend on several factors, such as the starting magmatic temperature (and hence the chemistry of the magma), the eruptive style (for example, eruption column collapse vs boiling-over activity), and the degree of interaction between the flow and external influences such as air and/or water (McClelland and Druitt, 1989). This technique has been most commonly applied to small-to-intermediate volume ignimbrites, thus focusing on eruption events that fall in the VEI 2 – 5 range that are largely dominated by partial column collapse (Vesuvius – Cioni et al., 2004; Kent et al., 1981; Paterson et al., 2010; Zanella et al., 2008, 2015; Fogo – Pensa et al., 2015a; 2015b; Colima – Clement et al., 1993; Paterson et al. 2010; Sulpizio et al., 2015; Santorini – McClelland and Druitt, 1989; Bardot, 2000; El Chichón – Sulpizio et al., 2008, 2015), overpressure jet/blast (Mount Saint Helens – Paterson et al., 2010), pyroclastic fountaining (Tungurahua and Cotopaxi – Rader et al., 2015) and explosion of a lava dome (Mount Unzen – Uehara et al., 2015).

At present, there have been very few applications of the paleomagnetic emplacement temperature technique to studies of the temperature of large-volume pyroclastic flows, the only examples being the VEI 8 Cerro Galán ignimbrite (Lesti et al., 2011) and the VEI 6 Taupo ignimbrite (McClelland et al., 2004). Similarly, little is known about the emplacement temperatures of phreatomagmatic ignimbrites (Cioni et., 2004; Porreca et al., 2006, 2008; Zanella et al., 2008, 2015; van Otterloo and Cas, 2016). Despite the lack of these kinds of study, they have a clear importance for better understanding the dynamics of large-volume magmatic and phreatomagmatic eruptions.

We quantify here the emplacement temperature of large-volume caldera-forming ignimbrites of Colli Albani volcano (VEI 6 – 7) using the thermal analysis of the magnetic remanence carried by both

lithic and juvenile clasts embedded within the deposit. In this work, we choose to analyze the aforementioned case studies because they offer the opportunity to compare large-volume ignimbrites characterized by similar features, such as chemistry (eruptive compositions are consistently mafic, <50% SiO_2, Boari et al. 2009; Conticelli et al., 2010), volume (on the order of 10-100 km^3, Giordano et al., 2010), and mobility (up to 33 km distance from the vent), but related with different magma fragmentation styles (i.e. magmatic and phreatomagmatic). It is therefore possible to discern temperature differences between the succession of ignimbrites and to interpret them in terms of the degree of magma-water interaction. Moreover, the thermal character of these deposits allows us to examine the flow mechanisms emplacing very large-volume ignimbrites.

1.2. Geological setting of Colli Albani ignimbrites

The Quaternary Colli Albani volcano is the southernmost caldera complex of the potassic Roman Magmatic Province (Mattei et al., 2010), and its volcanic activity is currently quiescent (Funiciello et al., 2003). The present topographic caldera has dimensions of 8 × 8 km and is located to the southeast of the city center of Roma (Fig. 1.1). Despite the erupted products being consistently silica undersaturated (<50% SiO_2; Boari et al., 2009; Conticelli et al., 2010), the style of activity of the Colli Albani volcano was mostly characterized by explosive caldera-forming eruptions during which several large-volume, low aspect-ratio ignimbrites were erupted, making this volcano one of the most explosive mafic volcanoes in the world.

During the oldest period of activity (between about 600 and 355 ka; Giordano et al., 2010), at least seven caldera-forming ignimbrites were emplaced over an area of about 1600 km^2 around the present caldera. Based on the currently preserved deposits, the eruptive volume for each ignimbrite has been estimated between 10 and 100 km^3 (Giordano et al., 2010). However, neither the distal co-ignimbrite ash nor the intra-caldera volume have been considered, suggesting that these volumes may represent minimum values. The products erupted during the earliest phase of volcanic activity are preserved to

maximum distances of about 35 km from the caldera center, where they were emplaced beyond topographic obstacles (i.e. Apennine Mountains) as high as 400 m.

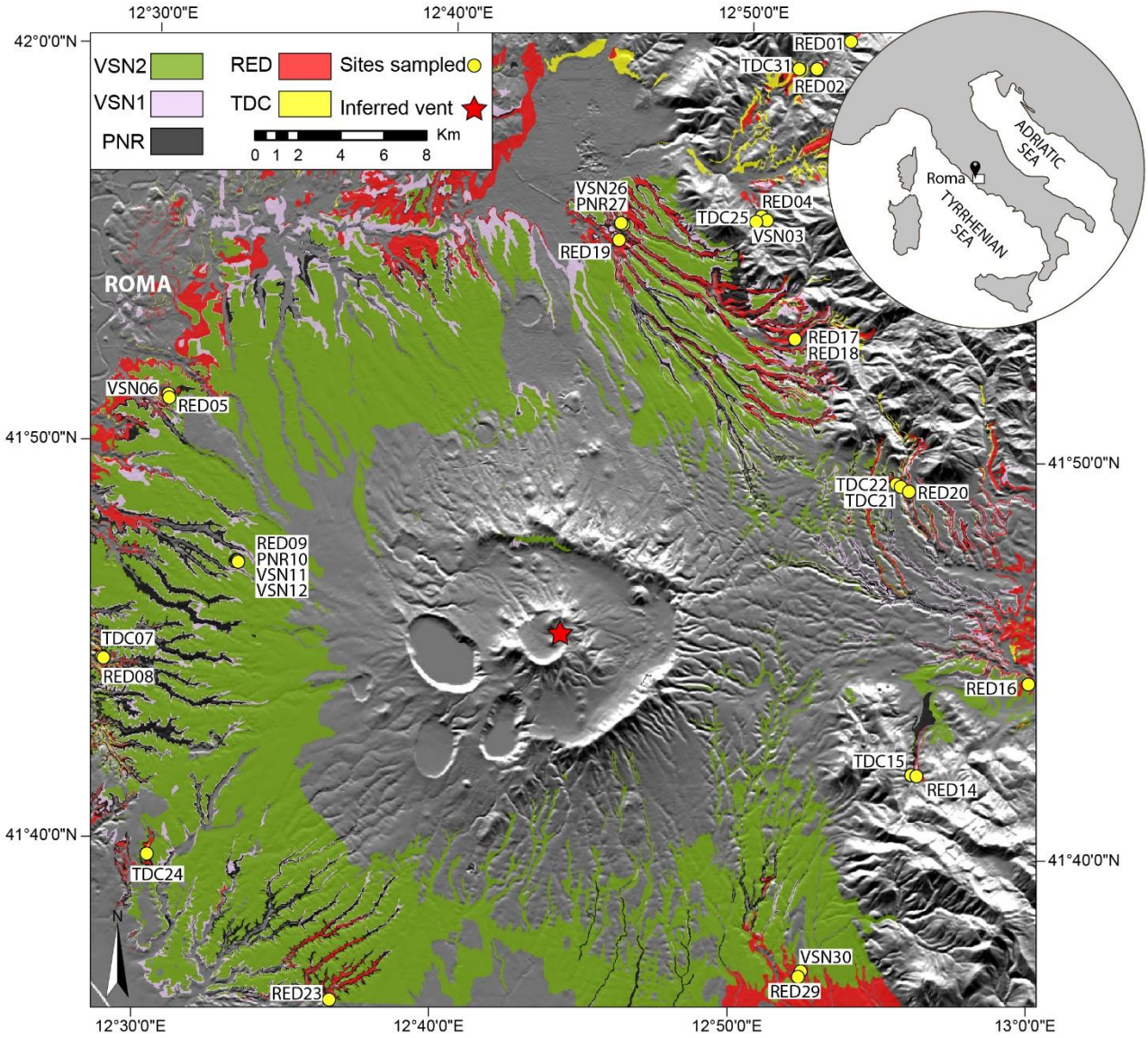

Fig. 1.1. *Simplified geological map of the Colli Albani volcano (location denoted by rectangle on inset map), showing the studied ignimbrites and sampling sites (modified from Giordano et al., 2010). The inferred vent location (red star) is the same for all the investigated ignimbrites.*

The oldest ignimbrites, grouped under the name of the Pisolitic tuffs succession (De Rita et al., 2002), show features commonly attributed to phreatomagmatic activity, such as the abundant presence of

accretionary lapilli and blocky fine ash shards. These lower deposits mark a long period of phreatomagmatism (about 100 ka) that has been interpreted to be due to interaction between the erupted materials and surficial water related to the persistence of a large pre-eruptive lake or lagoon (De Rita et al., 2002). Among these ignimbrites, the Tor de' Cenci unit (TDC) is the largest and best exposed unit, although its outcrops are limited mainly to distal areas.

The fragmentation mechanism subsequently changed from shallow phreatomagmatic to dominantly magmatic, suggesting the progressive exhaustion of the caldera lake. During this period of volcanic activity, three major ignimbrites were emplaced which, from oldest to youngest, are the Pozzolane Rosse (RED), the Pozzolane Nere (PNR) and the Villa Senni (VSN) ignimbrites. The outcrops of these ignimbrites are much better preserved, allowing a more extensive sampling through much of their extent. These ignimbrites are the subject of the present paper. A detailed description of their sedimentological features can be found in De Rita et al. (2002), Watkins et al. (2002), Giordano et al. (2010), and their main characteristics are summarized in supplementary Appendix A.

After the last caldera-forming eruption at about 355 ka (VSN), the eruptive style changed significantly to effusive and mildly explosive, forming an intracaldera stratovolcano as well as peri-caldera fissure systems (between about 355 and 180 ka). Subsequent very small- to small-volume, maar-forming phreatomagmatic eruptions occurred during the last period of activity at Colli Albani.

1.3. Materials and experimental procedure

An elegant description of the method of using progressive thermal demagnetization on both lithic and juvenile clasts embedded within pyroclastic deposits to estimate their emplacement temperature (T_{emp}) can be found in Bardot and McClelland (2000). A brief explanation of the principles of thermal remanent magnetization (TRM) is given in supplementary Appendix B.

The main purpose of our sampling was to evaluate the possible variations in the flow T_{emp} as a function of the distance from the source for both the magmatic and phreatomagmatic ignimbrites. To this end, TDC deposits were sampled in close proximity to the RED deposits, where possible. We specifically sampled in areas where PDCs interacted with the Apennine Mountains to investigate how temperature is affected by the presence of a topographic barrier. This allows us to test if changes of the flow velocity and capacity (e.g. Giordano, 1998) are also reflected by T_{emp} variations. Sample locations can be found in Figure 1.1.

Efforts were made to sample clasts of similar size, from 0.5 to 3 cm in diameter, to avoid possible thermal heterogeneity that can be recorded by large clasts (Marti et al., 1991; Cioni et al., 2004; Porreca et al., 2008). The majority of the collected samples are lithic clasts because the juvenile magnetic mineralogy may provide uncertain information (e.g. McClelland et al., 2004). In addition, we collected some scoria clasts at most sites, as recently Rader et al. (2015) have shown that using data from both types of clasts together provides more detailed information about the thermal history of PDCs. With this approach we aim at both verifying if at Colli Albani the results from lithics and juveniles are comparable and to build on the available dataset for juvenile. The clast population includes aphyric and porphyritic lavas, and poorly vesicular scoria clasts. The principal sampling procedure was identical to that used by Lesti et al. (2011), in which the strike and dip of each clast were taken in the field with a magnetic compass. We collected 364 samples from 29 sites, 7 of which are from the TDC unit, 14 from the RED unit, 2 from the PNR unit and 6 are from the VSN unit (3 from VSN1 and 3 from VSN2, see Appendix A; Table 1.1). Following the technique adopted by Cioni et al. (2004), the oriented clasts were set in 2.5-cm-diameter plastic cylinders filled with non-magnetic white plasticine. Stepwise thermal demagnetization was performed in air using a furnace with residual fields <10 nT, at the Paleomagnetic Laboratory of University of Roma Tre. Thermal stepwise demagnetizations were carried out with an average of 13 steps, from room temperature until the remaining intensity was less than 1% of the natural remanent magnetization (NRM). The remanence was measured after every demagnetization step and for each sample using an Agico JR-

6A Spinner Magnetometer. Demagnetization data were plotted on Zijderveld diagram (Zijderveld, 1967) and the principal components of magnetization were analyzed using Remasoft 3.0 software (Chadima and Hrouda, 2006). Paleomagnetic mean directions for each site are calculated applying Fisher statistics (Fisher, 1953).

The variation of magnetic susceptibility with temperature was measured on powders from representative samples (a subset of lithic specimens from two sites) by means of an Agico KLY-3 Kappabridge equipped with a CS-2 furnace. Samples were heated up to 700°C and cooled back to 40°C to estimate the Curie/Néel range of temperatures, according to the inverse susceptibility method proposed by Petrovský and Kapička (2006), and to examine for any possible mineralogical changes associated with the heating process in air.

The hysteresis properties of powders from representative samples were measured on a Princeton Measurements Corporation 3900 vibrating sample magnetometer (VSM), in fields up to 1 T. The powders were placed in pharmaceutical gel caps suitable for vibrating in the VSM, in order to determine, after subtracting the high field linear trend, the coercive force (B_c), the saturation remanent magnetization (M_{rs}), as well as the saturation magnetization (M_s). The coercivity of remanence (B_{cr}) values have been extrapolated from backfield remagnetization curves up to -1 T, following forward magnetization in a +1 T field. First-order reversal curves (FORCs, see Pike et al., 1999; Roberts et al., 2000) have been measured on selected specimens using the Micromag operating software, and processed and drawn with the FORCINEL Igor Pro routine (Harrison and Feinberg, 2008). FORCs have been measured in steps of 2.0 mT with an averaging time of 100 ms; the maximum applied field was 1.0 T.

All the magnetic mineralogy measurements were made at Istituto Nazionale di Geofisica & Vulcanologia, Rome.

Table 1.1
TRM results for each site

Unit	Site (ID)	Lat (°N)	Long (°E)	D (km)	N	Clast type		Class			T_{emp} (°C)
						L	J	A1	A2	B	
VSN2	VSN12	41° 46.950'	12° 33.048'	16	13	12	1			13	≥630
	VSN26	41° 55.826'	12° 45.628'	18,5	15	11	4			15	≥600
	VSN30	41° 37.014'	12° 52.290'	19,6	10	9	1			10	≥620
VSN1	VSN03	41° 55.969'	12° 50.543'	20,5	12	12				12	≥580
	VSN06	41° 51.136'	12° 30.629'	21,6	10	8	2			10	≥580
	VSN11	41° 47.031'	12° 33.062'	16	15	13	2			15	≥630
PNR	PNR10	41° 47.088'	12° 33.078'	16	14	14				14	≥580
	PNR27	41° 55.830'	12° 45.689'	18,5	12	12				12	≥600
RED	RED01	42° 00.572'	12° 53.399'	30	11	11				11	≥580
	RED02	41° 59.680'	12° 52.223'	27,8	9	8	1			9	≥560
	RED04	41° 56.092'	12° 50.552'	20,7	11	9	2			11	≥580
	RED05	41° 51.180'	12° 30.691'	21,5	14	12	2			14	≥580
	RED08	41° 44.482'	12° 28.737'	22,2	16	13	3			16	≥630
	RED09	41° 46.955'	12° 33.082'	16	25	17	8			25	≥630
	RED14	41° 42.072'	12° 56.175'	17,6	12	10	2			12	≥630
	RED16	41° 44.416'	13° 0.325'	22,1	15	14	1			15	≥630
	RED17	41° 52.917'	12° 51.761'	16,5	15	12	3			15	≥630
	RED18	41° 52.917'	12° 51.761'	16,5	11	9	2			11	≥630
	RED19	41° 55.372'	12° 45.710'	17,7	11	11				11	≥630
	RED20	41° 49.203'	12° 55.580'	16,6	10	10				10	≥630
	RED23	41° 34.960'	12° 36.659'	23	15	15				15	≥630
	RED29	41° 36.984'	12° 52.281'	19,6	16	13	3			16	≥620
TDC	TDC07	41° 44.428'	12° 28.664'	22,2	10	10		8	2		200 – 240
	TDC15	41° 42.079'	12° 56.031'	17,5	11	11		9		2	280 – 320
	TDC21	41° 49.312'	12° 55.269'	16,3	5	5		4	1		360 – 400
	TDC22	41° 49.344'	12° 55.414'	16,5	6	6		6			240 – 280
	TDC24	41° 39.604'	12° 30.379'	22,7	15	15		13		2	240 – 280
	TDC25	41° 56.038'	12° 50.509'	20,6	15	15		12	1	2	320 – 360
	TDC31	41° 59.936'	12° 51.772'	27,6	10	10		7		3	280 – 320

D, distance from the inferred vent; N, number of samples used in mean directions and T_{emp} estimations; L, lithic clasts; J, juvenile clasts; number of samples classified as Class A1, A2 and B; T_{emp}, estimated mean deposit temperature for each site

1.4. Results

1.4.1. Magnetic Mineralogy

The susceptibility *vs* temperature cooling curves are generally similar or below the heating curve in all the samples but TDC3107, meaning that the formation of new ferrimagnetic minerals due to the heating process is limited (Fig. 1.2A–F). Low-Ti titanomagnetite and magnetite are the main magnetic minerals, with exceptions for the sample TDC3107, in which Ti-rich titanomagnetite is probably the main magnetic carrier. In this case, T = 300°C cannot be taken as indicative of T_{emp}, because the overlapping blocking temperature (T_b) of the low-temperature (LT) and high-temperature (HT) components may be controlled by variations in the magnetic mineralogy.

Hysteresis loops, isothermal remanent magnetization (IRM) acquisition curves and backfield applications are well defined (Fig. 1.3A–D), due to the high values of the concentration-dependent magnetic parameters. The results are mainly consistent with a prevailing low-coercivity component, as evidenced by B_{cr} values generally lower than 50 mT (Fig. 1.3B). The exception is sample RED2904, whose B_{cr} value is considerably higher (69 mT); anyway, the significant presence of hematite can be excluded also in this sample, since the hysteresis loop and the IRM acquisition curve are saturated well below 1 T (Fig. 1.3A and C) and the estimated Curie temperature (T_c) is around 580°C (Fig. 1.2A).

FORC diagrams were performed on selected samples and indicate prevailing pseudo-single domain (PSD) features, even if the discrimination between PSD and a mixture of single domain (SD) and multidomain (MD) is not straightforward with these diagrams (Roberts et al., 2000); in general, a broad magnetic grainsize distribution is suggested.

The secondary peak at the origin of the FORC distribution of sample TDC3111 (Fig. 1.3F) can be ascribed to the presence of ultrafine superparamagnetic (SP) particles, as confirmed by the relevant decay of remanent magnetization 100 s after the application of 1 T magnetic field.

The FORC diagram of the sample RED2904 (Fig. 1.3E) is coherent with its high B_{cr} value; the coercivity distribution exceeds 200 mT and peaks at about 55 mT, probably due to oxidized or acicular magnetite in prevailing low interaction SD domain state/grain-size distribution.

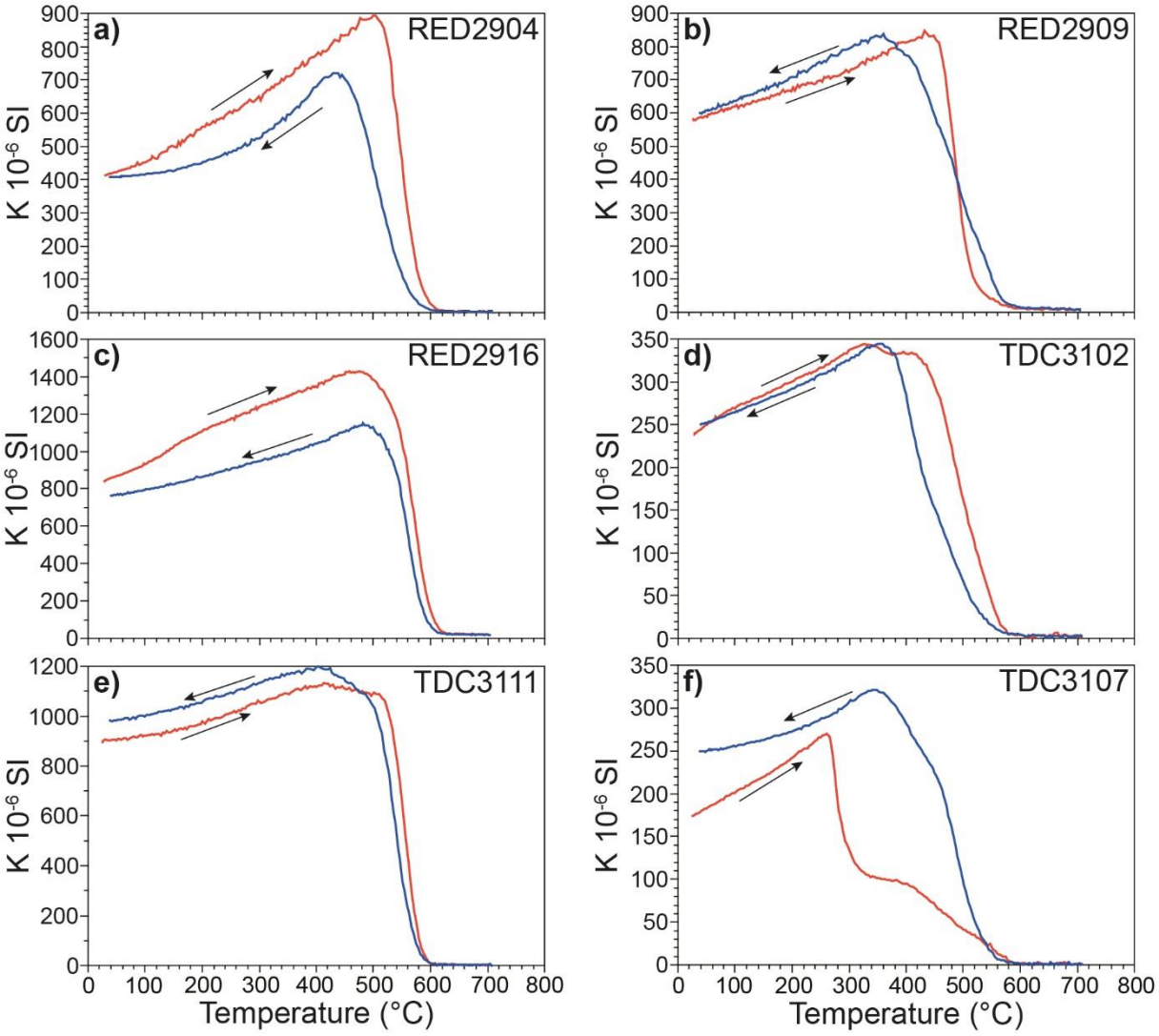

Fig. 1.2. *Thermomagnetic curves for selected lithic clasts. Red and blue lines represent the heating and cooling cycle, respectively.*

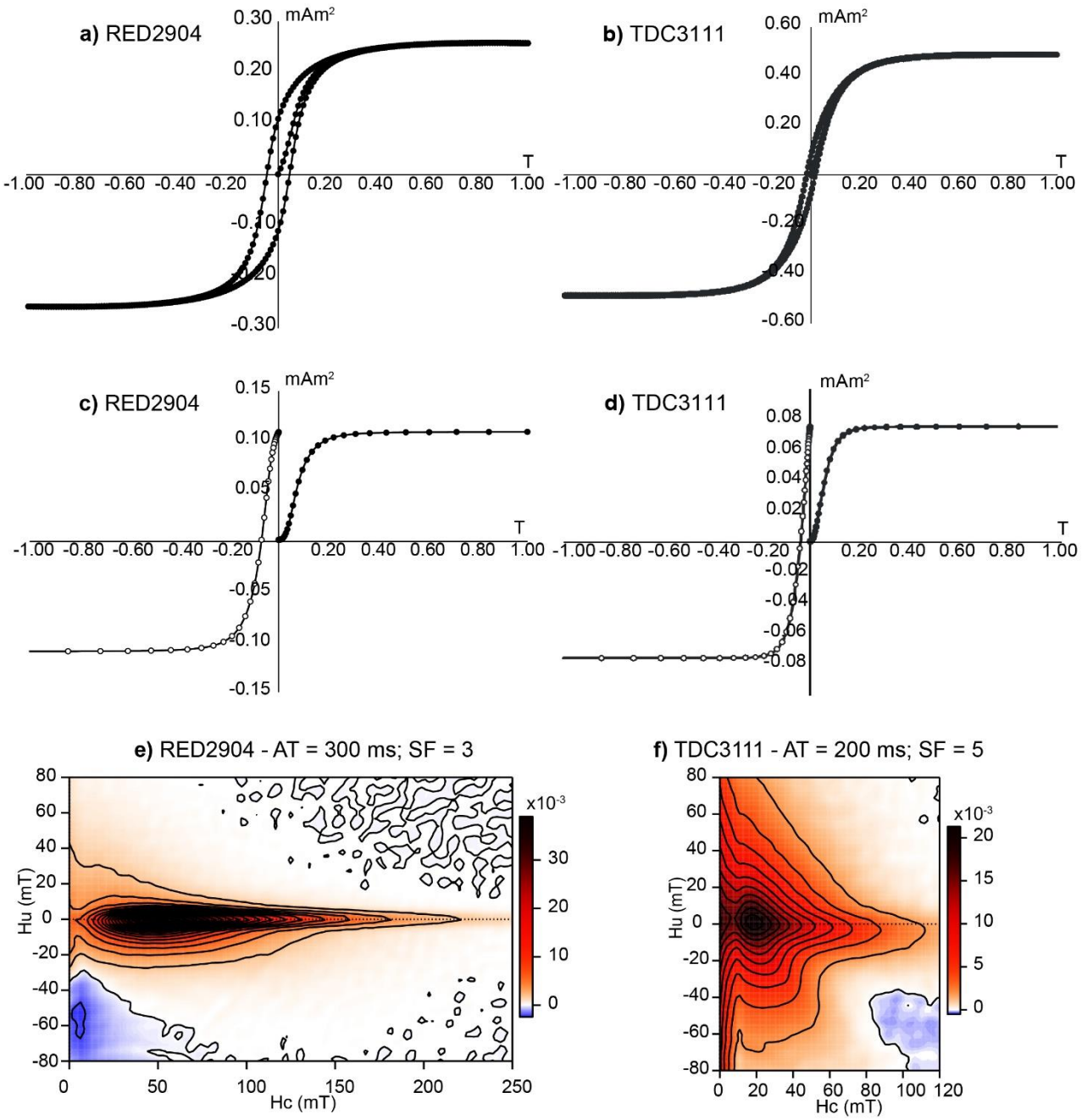

Fig. 1.3. *Hysteresis loops (a, b), IRM acquisition curves (c, d – black circles), backfield applications (c, d – white circles) and FORC diagrams (e, f) for samples RED2904 and TDC3111, respectively. Hysteresis loops are corrected for the high field paramagnetic linear trend. In FORC diagrams, AT is the selected averaging time and SF is the smoothing factor.*

1.4.2. TRM results

NRM intensities of all the analyzed clasts range from 1.1 x 10^{-3} to 17.8 A m^{-1}. Almost all samples show a stable magnetic behavior, and the remanence is typically completely unblocked at 520 – 630°C. Only a few samples did not exhibit stable behavior during progressive demagnetization and, therefore, they were not included in the data analysis.

Following McClelland et al. (2004), the demagnetization pattern has been classified into three groups distinguished by the number of magnetic components and their directions. Class A1 includes clasts that have two distinct magnetic components, with the LT component being parallel to the local geomagnetic field and the HT component being randomly oriented. The LT component represents the new partial thermoremanence acquired as the clast cooled in place, after deposition, whereas the HT component is the original magnetization that was not erased by the reheating event (Appendix B). Thus, the clast was never heated to temperatures related to the HT component. The temperature interval between the highest T_b of the LT component and the lowest T_b of the HT component marks the T_{emp}. In this case, for our example clast in Figure 1.4A, the T_{emp} estimate is 400 – 440°C. In Class A2, the vector plots are similar to those of Class A1, but the two magnetic components are separated by a curved path, which makes the estimation of the emplacement temperature less precise. In this case, we define T_{emp} as the range between the highest T_b and lowest T_b easily identified on the LT and HT components, respectively. Thus, for the clast in Figure 1.4B, T_{emp} is 320 – 440°C. In Class B, the remanence is a single component aligned with the local geomagnetic field (Fig. 1.4C), indicating that any original magnetization was completely reset by a new thermal event (Appendix B). In this case, the T_{emp} was equal to or higher than the maximum T_b of the magnetic carrier. Thus, for clast in Figure 1.4C, T_{emp} is $\geq$ 560°C.

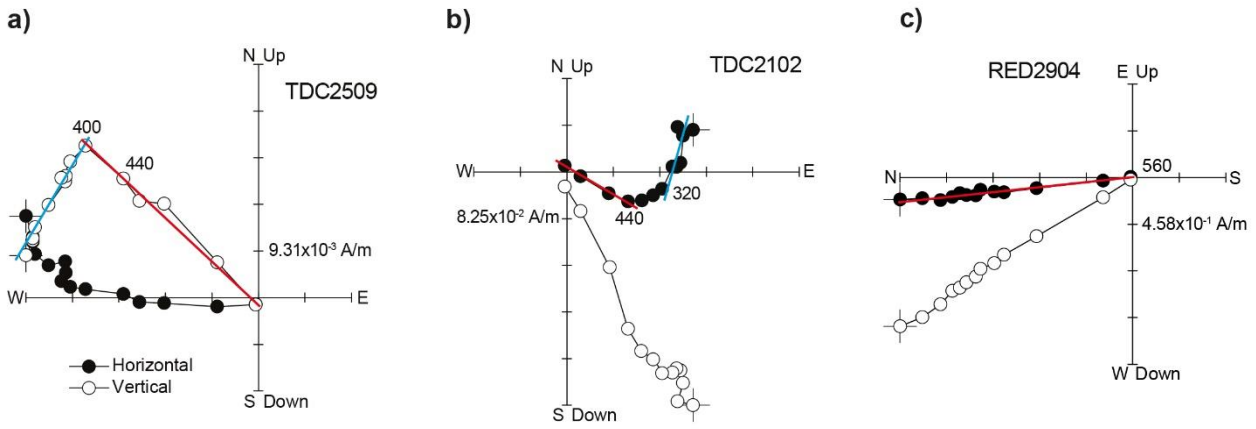

Fig. 1.4. *Stepwise thermal demagnetization data representative of the three classes identified. Black dots and white dots represent the horizontal and vertical projection of the magnetic vector at different laboratory temperature (°C), respectively. Red and blue lines represent the HT and LT components, respectively. (a) Lithic clast showing two distinct magnetic components (Class A1) with* T_{emp} *= 400 – 440°C. (b) Lithic clast showing two components of magnetization separated by a curved path (Class A2);* T_{emp} *= 320 – 440°C. (c) Lithic clast showing a single magnetic component (Class B);* $T_{emp} \geq$ *560°C.*

1.4.2.1. Magmatic units

The VSN unit includes two main ignimbrites named VSN1 and VSN2 (Appendix A). We analyzed 32 lithic and 6 juvenile clasts from 3 sites of the VSN2 unit. The NRM intensities range from 14.7 x 10^{-2} to 4.9, and 34.6 x 10^{-2} to 3.2 A m^{-1}, for the lithic and juvenile clasts, respectively. These samples show well distributed T_b spectra that are fully unblocked between 520 and 630°C. All the demagnetized clasts have single magnetic components (Class B, Fig. 1.5A; Table1.1).

We analyzed 33 lithic and 4 juvenile clasts from 3 sites of the VSN1 unit. The NRM intensity values range from 7.8 x 10^{-2} to 17.8 A m^{-1}, and the remanence was fully removed between 520 and 630°C. All the lithic clasts yield a well-defined single magnetic component (Class B, Fig. 1.5B; Table 1.1). The HT component identified for the lithic clasts is also recorded in all juvenile clasts. In Fig. 1.7A,

we grouped the HT components from VSN1 samples together with those of VSN2 samples. The mean direction of this HT component is D = 357.4° and I = 62.3° (k = 23.6, α_{95} = 3.5°), which is very close to the geocentric axial dipole (GAD) magnetic field for the sampled locality (Fig. 1.7A).

The 26 lithic clasts from 2 sites of the PNR unit have NRM intensities ranging from 55 x 10^{-3} to 3.2 A m^{-1}. The magnetization of each sample is fully unblocked between 520 and 600°C. All samples have single magnetic components (Class B, Fig. 1.5C; Table 1.1) that have a mean direction of D = 358.0°, I = 34.9°, (k = 35.7; α_{95} = 4.8°), which is close to the GAD magnetic field direction (Fig. 1.7B).

We demagnetized 164 lithic and 27 juvenile clasts from 14 sites of the RED unit. The NRM intensity ranges from 2.7 x 10^{-3} to 4.0, and 5.4 x 10^{-2} to 5.6 A m^{-1}, for the lithic and juvenile clasts, respectively. The majority of the samples are completely thermally unblocked between 520 and 630°C. All the lithic and juvenile clasts have a single magnetization component (Class B) with well-distributed T_b spectra (Fig. 1.5D; Table 1.1), which is stable up to 630°C. The orientations of this HT component are well grouped and lie close to the GAD field direction for the Colli Albani volcano, with D = 24.4° and I = 60.1° (k = 25.4; α_{95} = 2.1°; Fig. 1.7C).

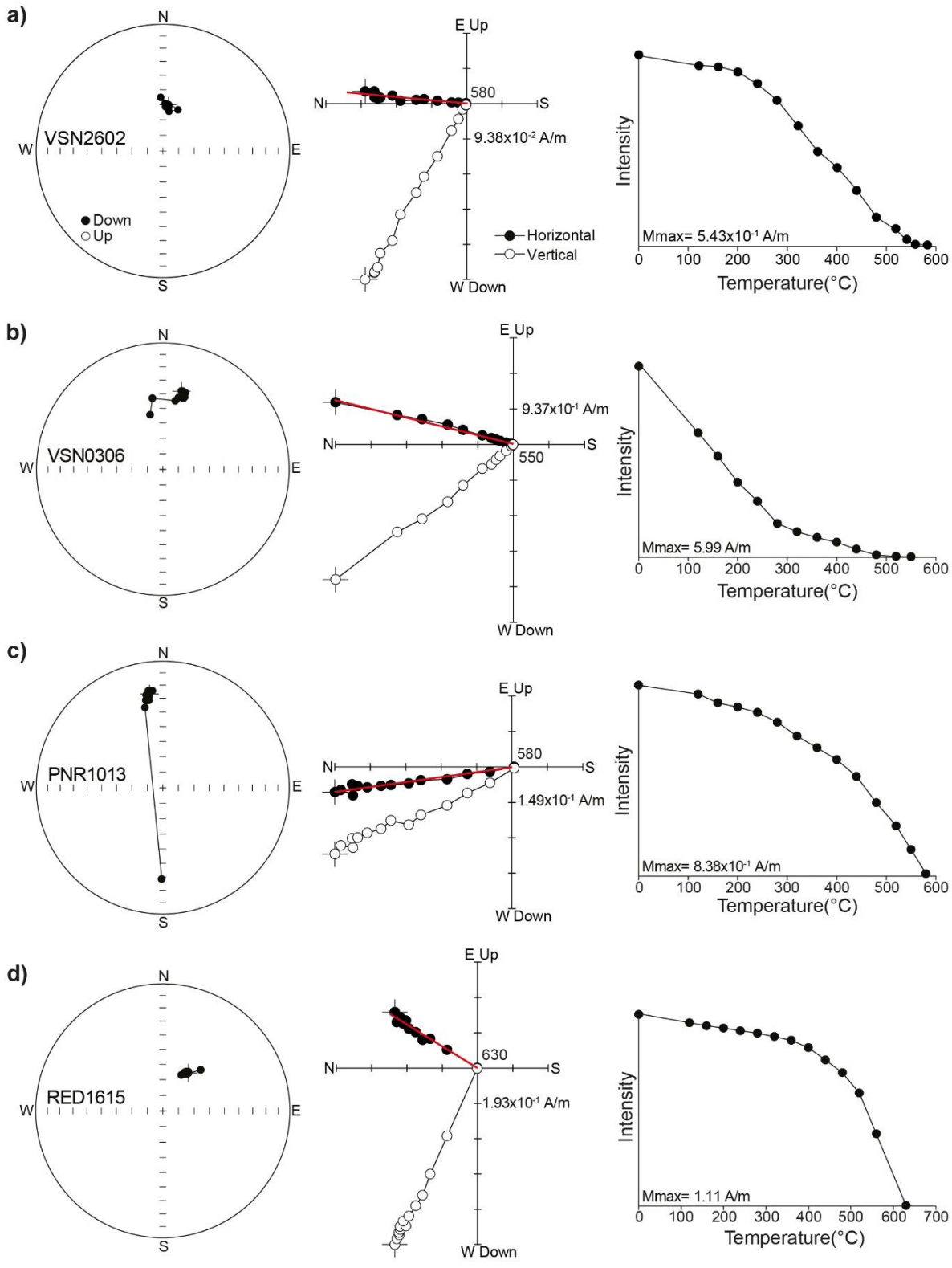

Fig. 1.5. *Representative thermal demagnetization data for selected lithic clasts from VSN2 (a), VSN1 (b), PNR (c) and RED (d) ignimbrites. (left) Equal-area stereonet (open and solid dots represent data on upper and lower hemisphere respectively), (middle) Zijderveld diagrams (symbols as in Fig. 1.4), (right) normalized intensity decay curve.*

1.4.2.2. Phreatomagmatic unit

A total of 72 lithic clasts were demagnetized from 7 sites of the TDC unit, with NRM values that are lower than those from the magmatic units, ranging from 1.1 x 10^{-3} to 2.4 A m^{-1}. Thermal demagnetization shows that most of the samples are completely demagnetized between 480 and 630°C. A few samples show unstable behavior and therefore were not included in the data analysis. Based on the T_b spectra, we identified clasts with one and two components of magnetization. In particular, 12% of the samples belong to Class B (Table 1.1) with an estimated mean direction of the HT component of D = 22.3° and I = 38.5° (k = 7.6, α_{95} = 29.6°). Among the clasts with two magnetic components, 94% and 6% belong to Class A1 and Class A2, respectively (Table 1.1). The temperature interval at which the LT component is fully removed varies between 200 and 480°C (Fig. 1.6A–B). The mean direction of the LT component is D = 6.5° and I = 51.5° (k = 15.6, α_{95} = 4.7°; Fig. 1.7D) while the HT component is randomly oriented (k = 1.1, α_{95} = 47.6°; Fig. 1.7E).

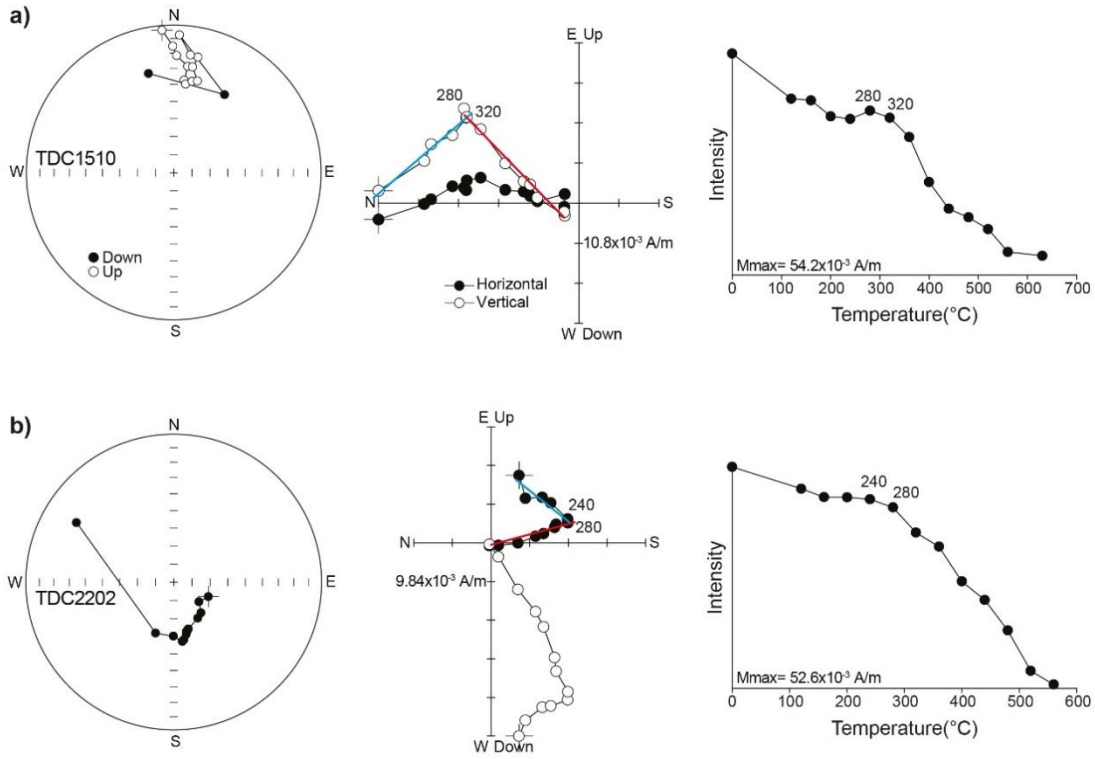

Fig. 1.6. *Representative thermal demagnetization data for selected lithic clasts from TDC ignimbrite (a, b). (left) Equal-area stereonet, (middle) Zijderveld diagrams, (right) normalized intensity decay curve. The symbols are the same as in Fig. 1.4.*

1.5. Discussion

1.5.1. Interpretation of thermal demagnetization data and T_{emp} estimation

As described above, the T_{emp} of each individual sample is determined from clast classification. All the magmatic units are dominated by the presence of Class B clasts, with maximum T_b ranging from 520 to 630°C. Although lithic clasts cannot record T_{emp} that exceed their T_c (maximum T_b), they still provide an important picture of the minimum temperature at which the deposits were emplaced. As discussed by some authors (e.g. Cioni et al., 2004), the different thermal history experienced by both accessory and accidental lithic clasts can make the interpretation of the T_{emp} difficult. This is because lithic clasts can be picked up cold by the flow along the volcanic flanks (accidental), or they may have experienced a pre-heating condition within the conduit (accessory). In some cases, a wide range of T_{emp} in a single PDC deposit has been documented, as a result of the coexistence of lithic clasts with different origins and thermal histories (e.g. Pensa et al., 2015a, 2015b).

Although it is not possible to know the thermal history of each clast, our data show unambiguously that the RED, PNR and VSN units were emplaced at high temperature. The consistency of the HT components, which are well grouped about the GAD magnetic field at Colli Albani, allows us to conclude that all the remanence of the clasts was acquired while cooling in situ within the deposit. This indicates that the PDCs were hot enough to unblock the maximum T_b of the clasts during transport and/or after their emplacement. For each site, the highest T_b value is considered as indicative of the minimum T_{emp} of the deposit in that location (Table 1.1). Then, the T_{emp} of the studied ignimbrites has been estimated as the maximum imposed by the highest T_b observed among each site, i.e. $T \geq 630$°C for RED and VSN units, and $T \geq 600$°C for PNR unit.

Lithic clasts sampled within the TDC unit mostly belong to Class A. In this case, T_{emp} of each clast is estimated between the maximum and minimum value of the LT and HT components, respectively. The estimated T_{emp} show significant differences among TDC sites, with values ranging from 200 to 480°C (Fig. 1.8). To identify the mean deposit temperature for each site, one possible approach is to

select the lowest T_{emp} value of the sampled clasts (McClelland et al., 2004; Paterson et al., 2010). According to this approach, the lowest T_{emp} value represents the equilibrium state at which all the different thermal populations start to cool as a whole and the highest ones are related to a pre-heating history. Cioni et al. (2004) suggested the possibility to have different cooling conditions as a function of the clasts position within the deposit (i.e. at the boundaries of the deposit) and defined the deposit temperature as the main overlap of T_{emp} of each clast at one site. Here we take the approach of Cioni et al. (2004) to explain the large scatter of temperature values and to estimate T_{emp} for each locality. At some sites, very few clasts showed a single component (Class B in Table 1.1). This is interpreted as due to a pre-heating condition. In any case, according to the standard methods for deriving the T_{emp} (e.g. McClelland et al., 2004; Cioni et al., 2004), their occurrence does not affect the estimated temperature of TDC deposits (Fig. 1.8). For each site, the mean T_{emp} is shown in Figure 1.8 and its value is reported in Table 1.1.

It is worth noting that we interpret the magnetization paths to be of thermal origin (i.e. TRM) rather than a chemical remanent magnetization overprint (Appendix B), because the magnetic mineralogy is reasonably uniform over the whole set of samples, and its variations are not connected to different emplacement temperatures.

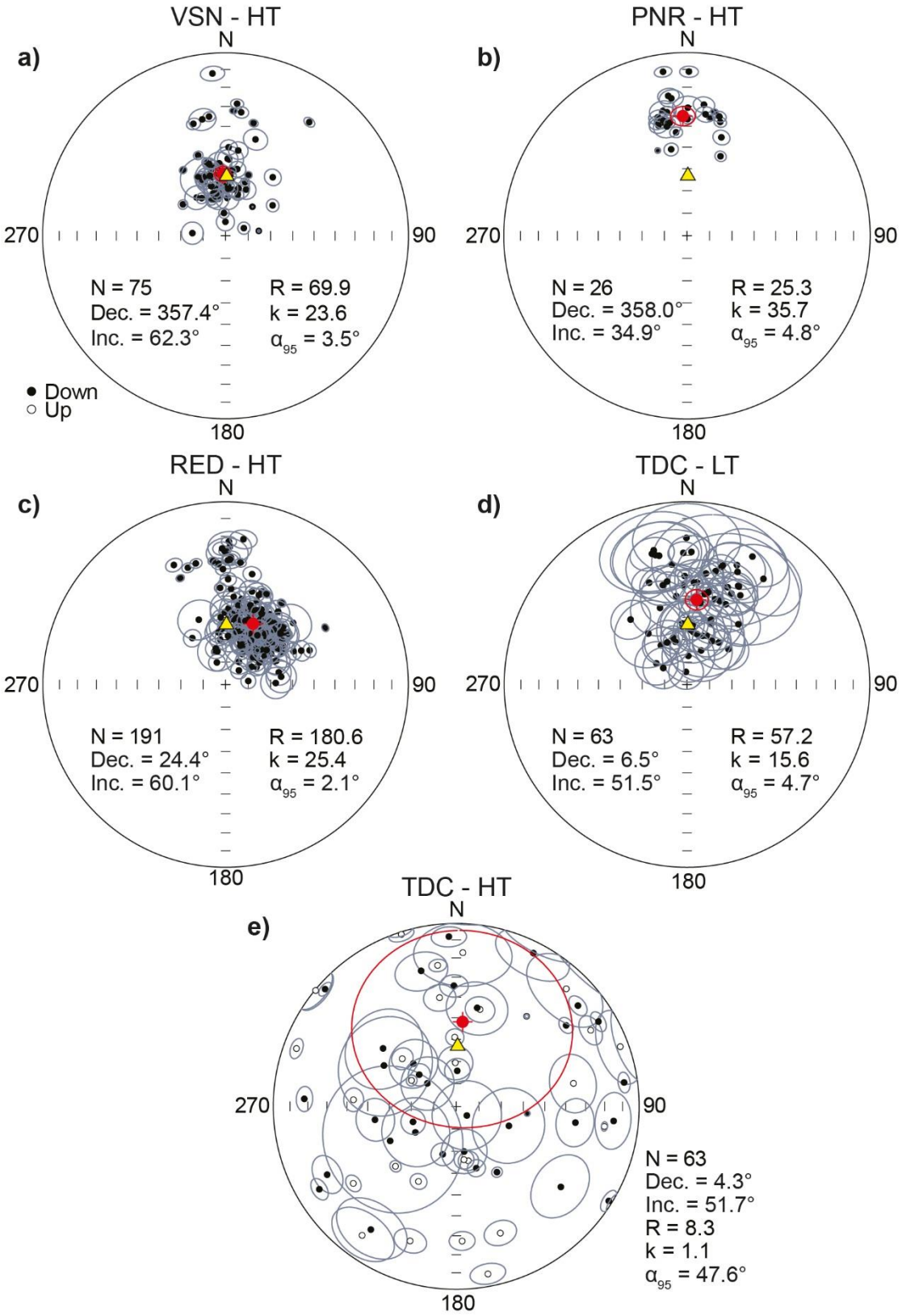

Fig. 1.7. *Equal-area projection of the mean paleomagnetic directions for the high-temperature (HT) and low-temperature (LT) components of each sample from the different unit (**a** – **e**). Open and filled symbols indicate upper and lower hemisphere projections respectively, and red dots denote the mean*

direction values. The α_{95} confidence ellipses are drawn for both samples (grey) and mean value (red). The yellow triangle marks the mean direction of the GAD field direction.

1.5.2. Temperature of magmatic vs phreatomagmatic ignimbrites

The differences between the analyzed ignimbrites are strikingly clear, with the phreatomagmatic unit (TDC) being significantly cooler than the magmatic ones (RED, PNR and VSN). Our T_{emp} estimations provide unequivocal evidence that all the magmatic ignimbrites were deposited hot, at temperatures higher than the maximum T_b of the magnetic carrier (i.e. titanomagnetite and magnetite). The high thermal signal matches with field evidence, such as the absence of charcoal fragments preserved in the deposits, suggesting that the high temperature completely incinerated any vegetation. In contrast, paleomagnetic data from the TDC unit yield T_{emp} between 200 and 400°C, with most of the samples within the 200 – 320°C range. These temperature estimates are consistent with the sedimentological features of the deposits, which show unequivocal evidence for magma-water interaction (i.e. abundant presence of accretionary lapilli and fine ash, and blocky shape of shards), indicating temperatures of 100 – 300°C (De Rita et al., 2002). This is also supported by the occurrence of preserved vegetation as charcoal within the deposit.

The temperatures of PDC deposits can vary widely, depending on their eruptive and transport histories (e.g. McClelland et al., 2004; Pensa et al., 2015a). Both the phreatomagmatic and magmatic PDCs investigated here share many similarities, such as chemistry (hence the initial magmatic temperature is assumed to be roughly the same), volume (on the order of 10 – 100 km^3), areal extent (Fig. 1.1), and their ability to climb topographic barriers as high as 400 m. A strong decrease in the temperature of the erupting material may occur during magma-water interaction (Koyaguchi and Woods, 1996). Thus, we interpret this temperature contrast in terms of the role of phreatomagmatism, as it is the main macroscopic difference between the two.

Low T_{emp} similar to those of the TDC unit have been estimated for small-volume phreatomagmatic ignimbrites, including deposits from Colli Albani (240 – 350°C, Porreca et al., 2008), Stromboli (<140°C, Porreca et al., 2006), Mount Gambier (<270°C, van Otterloo and Cas, 2016) and Vesuvius (180 – 240°C, Cioni et al., 2004; 260 – 360°C, Zanella et al., 2008, 2015; 240 – 370°C, Caricchi et al., 2014). T_{emp} for large-volume PDC deposits like the TDC ignimbrite have been documented for the 1.8 ka Taupo ignimbrite (>150°C, McClelland et al., 2004), the 25.4 ka Oruanui ignimbrites (150 – 250°C, McClelland and Wilson, pers. comm. in Wilson, 2001, and Van Eaton and Wilson, 2013), and at Santorini (400°C, Bardot, 2000). At Taupo, McClelland et al. (2004) found very different temperatures between proximal facies (less than 30 km from the source), where T_{emp} was estimated between 150 and 300°C, and distal facies (up to 50 km from the source), where lithic clasts were emplaced between 400 and 500°C. The authors interpreted the low T_{emp} as primarily due to mixing of the early-erupted proximal flow deposits with pre-eruption caldera lake, which partly surrounded the vent area. The low T_{emp} of the Oruanui eruption was also related to magma-water interaction (Wilson 2001; Van Eaton and Wilson, 2013). Evidences of its dominant phreatomagmatic origin arise from field observations showing an overall fine grain nature of the deposits with abundant presence of accretionary lapilli. Such sedimentological features are also found in the TDC unit, supporting the interpretation that the observed temperature differences among the studied units can be ascribed to phreatomagmatism. While phreatomagmatism in the small-volume case studies indicated above is due to interaction with ground-water, the large-volume ignimbrites most likely relate to interaction with caldera surface water (De Rita et al., 2002; McClelland et al., 2004). In contrast, most large-volume ignimbrites associated with pure magmatic fragmentation are usually characterized by high T_{emp}, as testified by extensive welding (e.g. Best et al., 2013) or temperature above the T_c (e.g. Lesti et al., 2011).

The results presented here indicate that the phreatomagmatic imprint on the T_{emp} can be of hundreds of degrees even in large-volume eruptions, highlighting the high efficiency of this process. However, it must be noticed that Mandeville et al. (1994) proposed that the subaqueous flow at Krakatoa was

not significantly affected by water (T_{emp} between 475 and 550°C), suggesting that other processes may occur in subaqueous environment to preserve temperature.

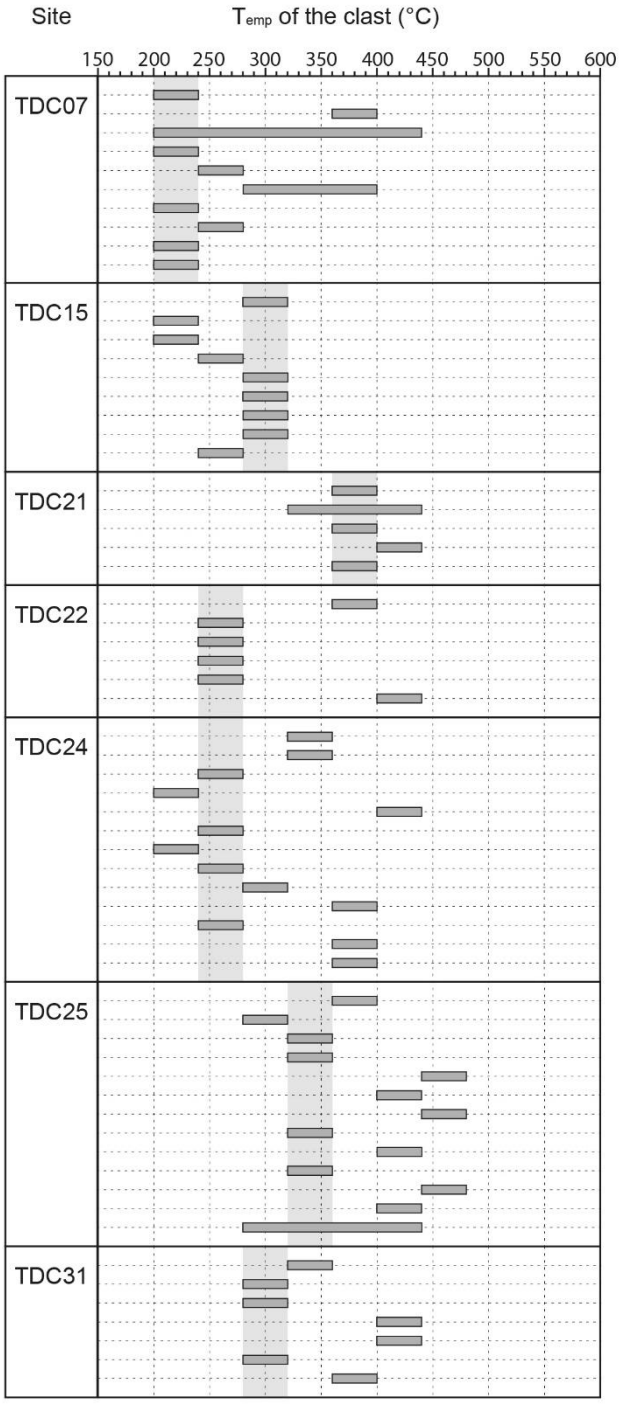

Fig. 1.8. *The deposit temperature of each site is determined by the main overlap of individual clasts T_{emp} range (grey bars) and is shown as grey zone.*

1.5.3. Forced transport of thermal energy

An interesting outcome of our study is that the temperature of all the ignimbrites investigated here appears to have been nearly constant throughout their extent and across topography, independent of the style of explosive activity (i.e. magmatic vs phreatomagmatic). Figure 1.9 shows the distribution of T_{emp} as a function of the distance from source for both the magmatic and phreatomagmatic ignimbrites.

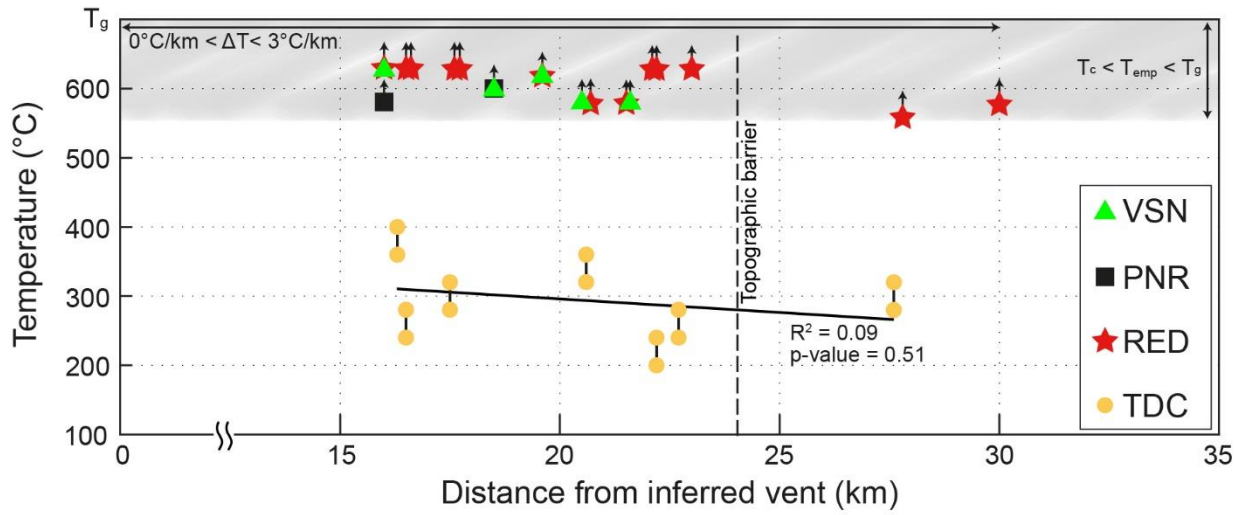

Fig. 1.9. *Temperature variation as a function of distance from the inferred center of the caldera for TDC (yellow dot), RED (red star), PNR (black square) and VSN (green triangle) ignimbrites. The regression line shows a very weak correlation between the temperature values of the TDC unit and the distance from the source. The light-shaded grey area represents the temperature interval between T_g and T_c, which highlights the T_{emp} range of the magmatic units.*

It is important to note that welding textures have not been recognized in most of the magmatic deposits, providing further information about the upper boundary of the T_{emp}. Given that the pyroclasts have been emplaced at temperatures lower than the glass transition temperature (T_g), we can refine the range of T_{emp} between T_c and T_g. Using the model of Giordano et al. (2008), we have

calculated the maximum T_g value of about 710°C for anhydrous compositions that encompass the full spectrum for the analyzed ignimbrites, ranging from tephrites to phono-tephrites (RED and PNR ignimbrites respectively; Boari et al., 2009). This suggests that the maximum temperature drop would have been approximately 100°C, from the onset of magma fragmentation to the emplacement of PDCs. Considering an average runout distance of about 30 km for all the magmatic units, the maximum lateral thermal gradient is about three degrees per kilometer (Fig. 1.9). Only the VSN1 ignimbrite is characterized locally by a lithofacies that contains approximately 10% spatter scoria clasts within an unwelded matrix, indicating that some plastic deformation occurred during/after emplacement for lapilli-sized clasts up to 16 km from vent (Watkins et al., 2002). This suggests that the bulk temperature of the deposit was lower than T_g.

Although in the eastern sector both the magmatic and phreatomagmatic PDCs crossed the morphological barrier of the Apennine Mountains, the temperatures of the deposits are surprisingly similar in comparison to the western area, where the flows expanded in an open plain condition. The role of topographic barriers perpendicular to flow direction is of great importance in accounting for flow dynamics (e.g. Andrews and Manga, 2011; Bursik and Woods, 2000). As discussed by Giordano (1998), the reduction of flow capacity and hindered settling conditions may occur at changes in slope, increasing the sedimentation rate. This process leads at the same time to the generation of the buoyantly rising co-ignimbritic clouds above the base of the barrier, which results in the elutriation of gas and fine ash (Andrews and Manga, 2011). The ash-cloud entrains atmospheric air, with subsequent adiabatic expansion, decreasing its density. All these factors should cause an efficient heat exchange within the ash-cloud. However, how much this process propagates inside the whole PDC and affects the basal part is unknown. The analyzed ignimbrites are thicker upcurrent of the ridge, thinning beyond the obstacle, and this aspect should be mirrored in a decrease of T_{emp} beyond the barrier. However, we do not observe significant temperature variation between sites located before and after the interaction of the flows with the morphological obstacle of the Apennine Mountains (Fig. 1.9). This is true for both the magmatic and phreatomagmatic PDCs, notwithstanding the large

amount of fine ash available in the TDC ignimbrite, which should promote rapid thermal equilibration in the phreatomagmatic flows both along the path and especially after passing over a barrier, as they enhance the level of dilution and the amount of air entrainment in the currents.

We find in the interpretation of Doronzo (2012) a possible explanation for the overall conservation of the thermal energy across the areal extent for the Colli Albani ignimbrites, which, based on our field and laboratory data, shows to be irrespective of their grain size, concentration (dilute and/or concentrated PDCs) and initial temperature (i.e. magmatic vs phreatomagmatic). Doronzo (2012) proposed a new subdivision of PDCs based on the flow energy (rather than the flow concentration), which is defined by two end-members: forced convection-dominated and inertia-dominated currents. Since they are time and space dependent, these two end-members are not strictly correlated to the well-known dilute and concentrated flows end-members or vice versa. Forced convection-dominated currents are sustained throughout by high mass flux, either for high mass discharge rates at source or for constriction along topography; in forced-convection flows, the lateral decay of mass, momentum and thermal energy is limited by the high mass flux that favors the maintenance of the pressure inside the current (Giordano and Doronzo, 2017). The inertial currents (driven by their own inertia) instead are characterized by a rapid decay of the internal pressure, which favors the rapid dissipation of mass, momentum and thermal energy.

We think that the forced-convection model is intrinsically more suitable to describe the thermal homogeneity of the Colli Albani ignimbrites, with respect to the dilute vs concentrated PDCs end-members, because the latter take into account only the sedimentological aspect. In fact, in the classical model, the internal structure of PDCs is commonly described by using vertical profiles of their velocity and concentration fields (neglecting their temperature field). The analytical and numerical treatment of the relationships between sedimentation and temperature can be found in Doronzo et al., 2016.

The ignimbrites investigated here show clear evidence of a forced transport of thermal energy and this well compares with the depositional characteristics of the ignimbrites. The evidence of a conservative transport system of the total energy is supported by: (1) the widespread massive and chaotic lithofacies of the ignimbrites (Giordano et al., 2010), indicating that they were emplaced by PDCs characterized by high sedimentation rates throughout; (2) the low aspect-ratio of the deposits, which indicates that their parental currents were able to transport mass for long distances (Giordano and Doronzo, 2017); (3) the fact that their parental currents climbed up to 400 m above the surrounding plains at about 25 km from the source, suggesting that their momentum was sustained through time. These observations suggest that all the parental currents of the investigated ignimbrites were very poorly dissipative in terms of mass, momentum and thermal energy, in agreement with the forced-convection model. For these reasons, we believe that the action of a sustained mass discharge rate (either at source and/or for constriction along topography) helped to maintain the flows at high internal pressures and consequently at high temperatures, making the cooling effect of air entrainment less efficient. This allows PDCs to be thermally isolated from the surrounding environment, independently of their dilute and/or concentrated nature, grain size distribution, and initial temperature (i.e. magmatic vs phreatomagmatic). As discussed by Roche et al. (2016), a sustained high mass discharge rate must be invoked to explain the extreme mobility of large-volume PDCs that form low aspect-ratio ignimbrites in which the deposits tend to be extensively welded over much of their extents, highlighting the low efficiency of mixing of air during flow.

Similar thermal homogeneity has been described for the >530 km^3, 2.08-Ma Cerro Galán ignimbrite (Lesti et al., 2011) that, even though less mobile, is also a low aspect-ratio ignimbrite interpreted as dominated by very high mass flux (Cas et al. 2011). Some other studies have also found that the T_{emp} of small-volume PDC deposits does not seems to change significantly along the flow direction (e.g. Porreca et al., 2008; Zanella et al., 2015). These cases may also be associated mainly to forced-convection flows, in which the degree of forcing is maintained in space and time (i.e. the timescale of the current) as a result of flow channelization in paleovalleys. Based on these considerations, we

suggest that a specific accounting of the temperature variations throughout the extension of a PDCs deposit can be used as a proxy to evaluate the degree of forced-convection vs inertial flows.

1.6. Conclusions

Understanding the fundamental properties of PDCs, and particularly their temperature, is essential to assess the hazard related to these complex physical phenomena. Nonetheless, the thermal evolution of PDCs, especially those associated to large-volume eruptions, is still poorly understood. We have investigated the temperature of emplacement of large-volume caldera-forming ignimbrites erupted at Colli Albani volcano by using thermal remanence analysis on both lithic and juvenile clasts. What the present study reveals is that:

- The magnetic mineralogy in lithic clasts belonging to the TDC and RED units is mostly characterized by Ti-poor titanomagnetite and magnetite grains. No significant indications of magnetic alteration due to heating are present, supporting the validity of our T_{emp} estimates.
- T_{emp} of all the magmatic ignimbrites ranges from the maximum T_b of the magnetic carrier (i.e. RED and VSN $\geq$ 630°C, and PNR $\geq$ 600°C) to T_g (i.e. about 710°C), whereas the phreatomagmatic TDC ignimbrite was emplaced between 200 and 400°C, with the majority of the samples within the 200 – 320°C range. We attribute this T_{emp} difference to efficient and sustained magma-water interaction throughout the eruption, which lowered the initial temperature of the PDC by several hundred degrees.
- Independently of the eruptive mechanism (i.e. magmatic vs phreatomagmatic), the emplacement temperatures of the investigated ignimbrites exhibit little change with distance from the source, despite the interaction between the flows and the morphological barrier of the Apennine Mountains.

According to the model of Doronzo (2012), the Colli Albani ignimbrites were emplaced by forced-convection PDCs (Giordano and Doronzo, 2017). We suggest that forced-convection well explains the characteristics of large-volume ignimbrites dominated by high mass fluxes that force the lateral transport of mass, momentum and thermal energy, justifying their usual low aspect-ratios, consistent lithofacies associations, and overall conservation of the thermal energy across the areal extent and in different paleo-topographic settings. Based on our findings, we conclude that spatial variations of T_{emp} can be used to discriminate between forced and inertial PDCs, providing an insight into the flow dynamics. We hope that our results and observations may serve to stimulate future numerical and analog modeling studies to investigate the effect of sustained mass flow rates on the multiphase physics of PDCs and related hazard.

1.7. Supplementary Appendix A: Description of the analyzed units

A brief summary of the main sedimentological features of the studied ignimbrites are described here to provide an understanding of their nature. Figure 1.1A shows a composite stratigraphic column of the Colli Albani volcano, emphasizing the studied units.

Tor de' Cenci ignimbrite (TDC):

The TDC unit represents the best exposed and largest volume ignimbrite erupted during the early caldera-forming period at Colli Albani, dominated by large volume phreatomagmatic eruptions, and represented by the Pisolitic Tuff succession (Giordano et al., 2010). This unit has been dated at 561 ± 2 ka using sanidine and leucite $^{40}Ar/^{39}Ar$ method (Karner et al., 2001) and its chemistry is K-foiditic (42.69 – 44.67 wt.% SiO_2; Palladino et al., 2001). The deposit volume has been estimated at ca. 20 km^3 (Giordano et al., 2010), which identify an eruption of VEI 6. The TDC unit contains an underlying moderately sorted, ungraded to reverse-graded fall deposit, which is made of coarse ash- to small lapilli-sized poorly vesicular scoria (80 – 90%), altered crystal fragments (leucite, clinopyroxene, mica; 10 – 20%) and minor amount of lithic clasts. Although the scarcity of outcrops, the evidence that the deposit thickness at a distance of 25 km from the caldera is 10 cm to the west and 25 cm to the NE suggests that the main dispersal axis is towards east (De Rita et al., 2002). The fallout deposit is overlain by the associated ignimbrite, which consists mostly of fine and coarse ash (85 – 95%) of poorly vesicular juvenile shards (with angular blocky shapes) and crystals (leucite, clinopyroxene, mica), and subordinate amount of grey and yellow scoria lapilli, and lithic clasts (up to 10% of the deposit) with average diameters less than 1 cm. The presence of spherical accretionary lapilli (0.5 – 3 cm in diameter), which occur both sparsely within the matrix and in discrete layers, is the most striking feature of this unit. The deposit is rich of charcoalified woods (up to 40 cm in diameter) at the base. The ignimbrite is non-welded, but ubiquitously lithified through vapour phase alteration. The TDC ignimbrite varies from a massive and thick (up to 20 m) facies in the eastern

sector (i.e. along the Aniene River paleovalley, and across the Apennine Mountains), to multiple planar- to low-angle cross-bedded and massive depositional units in the western sector (i.e. open plains). Preserved outcrops in the eastern sector can be found at topographic height up to 250 m, where the flow overpass the Apennine Mountains.

Pozzolane Rosse ignimbrite (RED):

The RED unit represents the most widespread and largest volume ignimbrite erupted at Colli Albani volcano, with an outcrop area extending over ca. 1600 km^2 and a dense rock equivalent volume of ca. 60 km^3 (Giordano et al., 2010; Giordano and Doronzo, 2017), which can be associated with an eruption of VEI 7. Deposits are distributed axisymmetrically around the central caldera up to distances of 33 km to the NE. The ignimbrite is tephritic in composition (Conticelli et al., 2010) and it has been dated at 456 ± 3 ka ($^{40}Ar/^{39}Ar$, Marra et al., 2009). The base of the unit is defined by the presence of a reverse-graded scoria lapilli fallout deposit, with a maximum thickness of 70 cm and dispersal axis toward ENE (Giordano et al., 2010). The main lithofacies of the ignimbrite is mostly massive and chaotic, poorly sorted and matrix supported. This facies consists of reddish-purple to dark grey, aphyric- to leucite- and clinopyroxene-phyric, vesicular to poorly vesicular scoria (up to 30 cm in diameter) and lithic clasts (up to 8 cm in diameter) in a crystal and coarse-ash shard matrix (60 – 90%). It is distinguished from the other products of Colli Albani by its content of thermally metamorphosed sedimentary lithic clasts. The ignimbrite is generally unconsolidated and in some places moderately lithified by zeolites. The ignimbrite is a tabular sheet that can be up to 80 m thick (at a break in slope of the volcano, in paleovalleys and in front of the Apennine Mountains), with an average thickness ranging from 10 to 20 m. Outcropping deposits in the eastern sector are found beyond topographic barrier ca. 400 m high.

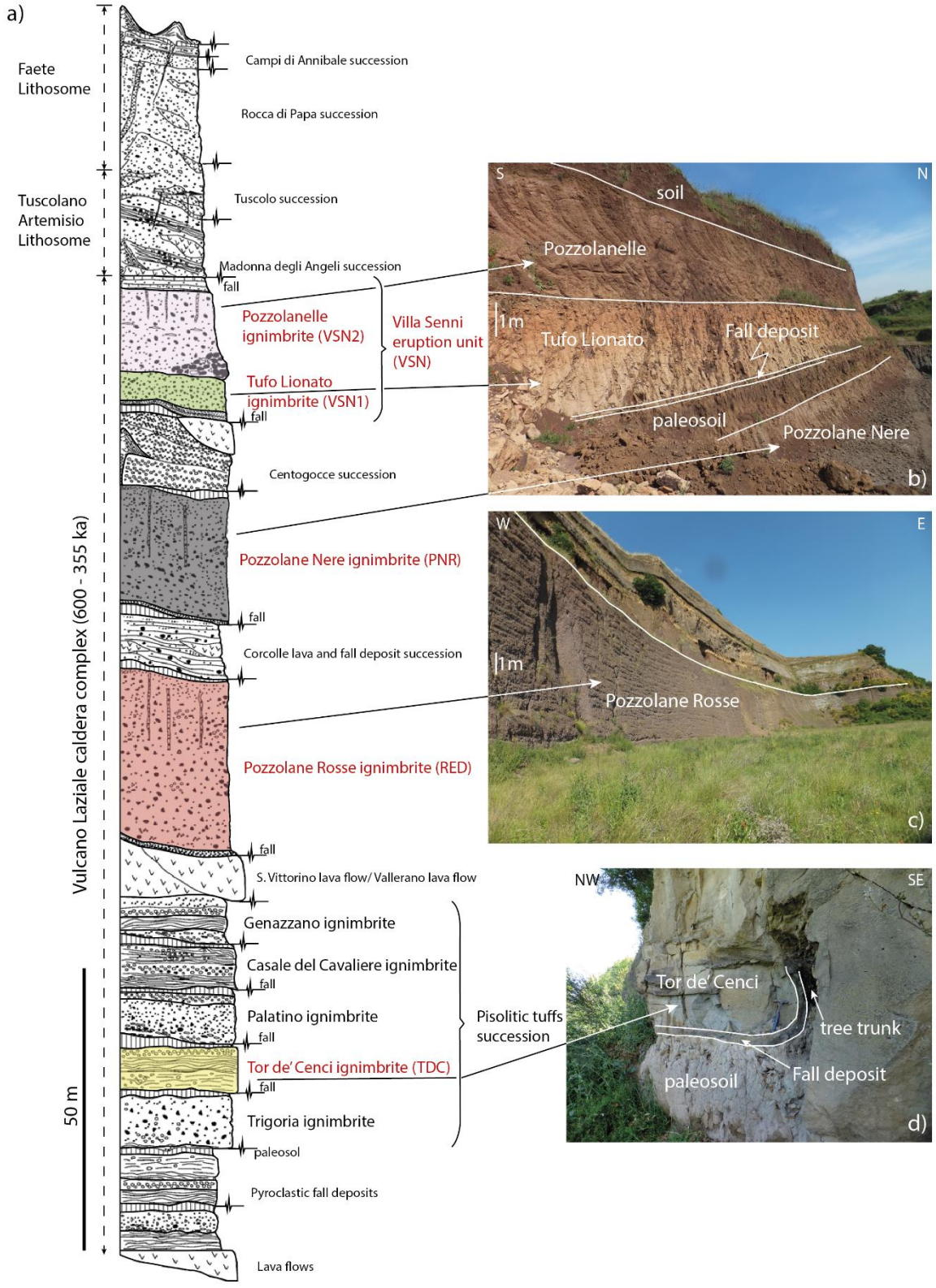

Fig. 1.1A. *(**a**) Composite stratigraphic log of the Colli Albani volcano (simplified after Giordano et al., 2006, 2010) emphasizing the studied ignimbrites with colors. (**b**) Outcrop photograph showing the VSN2 (site VSN12), VSN1 (site VSN11) and PNR (site PNR10) ignimbrites within the Imater quarry. (**c**) Outcrop photograph showing the RED ignimbrite (site RED19) within Corcolle quarry.*

(d) *Outcrop photograph showing the TDC ignimbrite (site TDC07), which at the base is characterized by planar stratification whereas the upper part is massive. Note the occurrence of a flattened and charred tree trunk at the base of the ignimbrite, which deformed the basal fall deposit after the impact.*

Pozzolane Nere ignimbrite (PNR):

The PNR ignimbrite is tephritic-phonolitic in composition (Conticelli et al., 2010) and has been dated at 407 ± 4 ka ($^{40}Ar/^{39}Ar$, Karner et al., 2001). The eruptive volume of the PNR has been estimated at ca. 15 km^2 (Giordano et al., 2010). The base of the unit is characterized by the presence of a stratified sub-aphyric and vesicular scoria lapilli fall bed, with multiple dispersal axes toward ENE and ESE and with a maximum outcrop thickness of 160 cm at 18 km from caldera center (Giordano et al., 2010). The overlying ignimbrite is a poorly sorted, dark-grey to black, massive and chaotic, non-welded unit, which is up to 20 m thick. The basal 25 – 50 cm show reverse coarse tail grading that progressively grade upward in the main matrix supported facies. Fine-ash matrix, including crystal fragments of leucite, clinopyroxene and biotite, constitutes ca. 80 – 90% of the ignimbrite. Lapilli to bomb-sized porphyritic and vesicular scoria clasts constitute up to 30 vol.% of the ignimbrite. Lithic clasts (up to 12 cm in diameter) represent at most 5 vol.% of the ignimbrite.

Villa Senni formation (VSN):

The VSN formation represents the last large volume caldera-forming eruption of the Colli Albani volcano. The deposits currently outcrop to maximum distances of ca. 35 km from caldera center and are distributed symmetrically around it, covering more than 1600 km^2. The eruptive volume has been estimated at ca. 30 km^3 (Giordano et al., 2010). Several age determinations have been proposed for the VSN formation, which are clustered at ca. 355 ka (cf. Soligo and Tuccimei, 2010). The VSN sequence is composed, from the base to the top, of a basal fall and surge deposit and two main ignimbrite, which have been erupted during the same explosive event. The basal deposit is a faintly

cross-stratified, coarse-ash surge deposit up to few centimeters thick, overlain by a scoria lapilli fall deposit up to 140 cm thick, with a dispersal axis to the ENE of the vent area (Giordano et al., 2010). The fallout bed is overlain by the Tufo Lionato ignimbrite (VSN1) that is a lithoidal, yellow to reddish, massive and chaotic, up to 25 m thick in paleovalleys. The ignimbrite is tephritic-phonolitic in composition (Conticelli et al., 2010). Ash matrix represents ca. 70 – 90% of the ignimbrite. The framework is mostly made of low to moderately vesicular scoria (80 – 90%), crystal fragments (leucite, clinopyroxene, phlogopite; <5%) and accessory lithics (ca. 20%). The average grainsize is 2 – 3 cm, with maximum diameter up to 20 cm. The upper part of the unit is characterized by the presence of spatter scoria clasts (up to 30 vol.% of the total juvenile clasts, and a grainsize up to 20 cm), which have an elongated shape often not horizontally aligned (Watkins et al., 2002). There is also no evidence of welding of the unit or coalescence of the spatter clasts. This facies outcrops only in proximal to medial settings to the N and NW of the caldera. The overlying unit is the Pozzolanelle ignimbrite (VSN2), which is a dark grey to dark red, massive and chaotic, ash-matrix supported ignimbrite that can be up to 80 m thick in proximal areas. The composition varies from tephritic to tephritic-phonolitic (Conticelli et al., 2010). In contrast with the VSN1, the VSN2 ignimbrite is largely unconsolidated, maintaining its coarse ash-matrix supported character. The lithofacies consists mostly of dark reddish to black, aphyric to highly porphyritic, vesicular to poorly vesicular scoria and subordinately by lithic clasts, in a crystal (leucite, clinopyroxene, biotite) and coarse-ash shard matrix (60 – 90%). The average clast size is 5 – 6 cm, with maximum diameter of the scoria clasts that can be up to 90 cm in the most proximal settings. Lithic clasts consist mostly of lava, skarn and intrusives. In proximal locations along the north and north western sector of the caldera, the VSN2 ignimbrite presents a basal co-ignimbrite lithic breccia (up to 5 m thick), which is coarser-grained and very fines-depleted in comparison with the overlying main lithofacies.

1.8. Supplementary Appendix B: Extended method section

Many studies have applied the principle of thermal remanent magnetization (TRM) to extract information about the temperature of emplacement of pyroclastic deposits (e.g. McClelland and Druitt, 1989). Analysis of progressive thermal demagnetization data provides valuable information on the emplacement temperature (T_{emp}) of ignimbrites, thereby enabling a detailed reconstruction of the thermal history of pyroclastic density currents (PDCs).

During pyroclastic eruption, various amount of lithic clasts can be ripped from the walls of the magma chamber-conduit system (accessory lithic clasts) and/or eroded from the ground surface (accidental lithic clasts) being successively incorporated into a PDC. The heating process of lithic clasts containing ferromagnetic grains resets a portion of their original magnetization corresponding to blocking temperature (T_b) less than or equal to the maximum temperature experienced by the clasts while tumbling into the flow or in place after deposition. T_b represents the temperature at which the magnetic grains, in the clasts, record part of the TRM at the time of their cooling, as a function of their grain size, composition and shape.

If the temperature of pyroclastic flow is greater than the Curie temperature (T_c; maximum T_b) of the magnetic grains within each lithic clast, then the original magnetic remanence will be completely unblocked. During the subsequent cooling to ambient temperature, or below the T_b, all clasts will acquire a new magnetic remanence parallel to the local geomagnetic field at the time of emplacement. Thus, a single magnetic component is indicative of relatively (depending on the magnetic mineralogy) high temperature PDC. On the other hand, if the T_{emp} does not exceed the maximum T_c, only a portion of the original magnetization will be unblocked and lithic clasts will acquire a new partial thermomagnetic remanence (pTRM) during cooling, which partially overprints the original magnetization. In this case, two magnetic components can be observed: a low temperature (LT) component aligned with the local geomagnetic field at the time of emplacement and a randomly oriented high temperature (HT) component.

Progressive thermal demagnetization experiments allow isolating the two magnetic components and estimating the highest temperature needed to reset the LT component. At each thermal step, a portion of the total remanence is unblocked and then the magnetic remanence can be measured. The T_{emp} of the lithic clast with two magnetization components is then estimated to be the temperature interval between the highest demagnetization temperature at which the low T_b component is fully unblock and the next temperature step. In the case of a single component aligned with the expected geomagnetic field at the time of cooling, a lower limit on the emplacement temperature can be obtained by the higher T_b of the clast.

The above discussion assumes that the natural remanent magnetization (NRM) acquired at the time of emplacement is a TRM. As emphasized by Bardot and McClelland (2000), thermal results may be erroneous if the magnetic mineralogy of specimens of lithic clasts has been altered during the eruption and progressive thermal demagnetization. As a consequence of this alteration, the magnetic carriers will acquire a chemical remanent magnetization (CRM) that may partially or completely replace the original T_b spectra. The acquisition of a chemical overprinting is typically due to the formation of a new magnetic grain, the alteration of a pre-existing magnetic phase and shape variations of existing magnetic minerals (McClelland and Druitt, 1989). Given that the T_b of a magnetic grain is controlled by its composition, size and shape, a new or modified mineral phase may yield a T_b that is not connected to the temperature at which it is formed/altered. This leads to the coexistence of two groups of magnetic grains with $T_b > T_{emp}$: those that carry the previous randomly oriented thermoremanence (the HT component), and those that carry a remanence that is parallel to the magnetic field at the time of their formation/alteration. As a result of this overlapping, the vector plots show a curvature of their trajectories above T_{emp} (McClelland – Brown, 1982; Bardot and McClelland, 2000). In these cases, T_{emp} can be estimated as the temperature interval between the highest T_b of the LT component and lowest T_b that is easily identified on the HT component. If the CRM overprints also the LT component then the whole T_b spectra will be related to the magnetic properties of the new (or altered) magnetic grains, providing no information about T_{emp}.

In this study, specific magnetic mineralogy analyses, such as the variation of the magnetic susceptibility with temperature in air, hysteresis loops and isothermal remanent magnetization acquisition, have been performed to detect the main magnetic minerals and their possible alteration during heating and simultaneous oxidation.

An additional caveat to the acquisition of CRM is that the paleomagnetic components can be altered if the clasts are exposed to a magnetic field for a prolonged period, producing a viscous remanent magnetization (VRM) overprint. As a result, a low T_b component that is parallel to the present day geomagnetic field can be a VRM. Both VRM and CRM can affect the identification of the T_b spectrum of a clast, being magnetic components that can be interpreted as pTRM. Since the time dependence of magnetization also depends on the temperature at which the exposure occurs (Néel, 1949), a VRM can be removed by thermal demagnetization in the laboratory. Following the approach of Bardot and McClelland (2000), we have calculated 160°C as the temperature needed to unblock the maximum T_b for any VRM. Thus, LT components of magnetization with T_b equal or lower that 160°C have been excluded from further analysis.

Chapter 2

Thermal behavior of the high-energy PDCs associated with the 2010 Merapi eruption

Note – In preparation for submission:

Trolese, M., Giordano, G., Komorowski, J.K., Jenkins, S., Baxter, P.J., Cholik, N., Raditya, P., Corrado, S. Thermal behavior of the high-energy PDCs associated with the 2010 Merapi eruption.

Abstract: Temperature is one of the main parameters of pyroclastic density currents (PDCs) having important implications for hazard assessment. Understanding the thermal behavior of these complex physical phenomena is crucial for forecasting scenarios for exposed populations. In this work, we investigate the temperature of the high-energy PDCs produced during the explosive outburst at Merapi (Central Java) on 5 November 2010 (Stage 4), the most powerful and devastating event observed at this volcano since 1872, being responsible for more than 200 fatalities and a massive destruction of trees and buildings. This event is anomalous with respect to standard block and ash flows generated by the collapse of the summit dome that was growing fast and partially collapsing since October 26. We perform optical analyses on charcoal fragments embedded into the turbulent PDCs deposits to determine the emplacement temperature. Samples were collected from 29 localities at varying distances from the vent in both unconfined and valley-confined lithofacies to analyze the potential temperature drop that might be related to the interaction of PDCs with irregular topography. Results show mean reflectance (Ro%) values mainly between 0.17 and 0.41, with few charcoal fragments recording higher values possibly connected with the thermal disequilibrium condition of the deposits due to the influence of largely bimodal grainsize distribution of the deposit. These new Ro% data provide minimum temperature of the flow of 240 – 320°C, consistent with previous estimations determined from independent field, engineering, and medical observations published in the literature for this eruption. Charring temperatures show no major differences between proximal and distal deposits, suggesting that PDCs interaction with topography and the effects of air entrainment may have not played the main role in the thermal dissipation of particles along the flow path. We therefore infer that the temperature drop from fragmentation temperature occurred in the very initial part of the current. The proposed blast-like mechanism associated with the 5 November

paroxysmal event was likely responsible for the sudden temperature drop. Further numerical work is needed to verify this.

2.1. Introduction

The last major eruptive sequence of the Merapi volcano, in Indonesia, began on 26 October and ended on 23 November 2010 (Surono et al., 2012). During this period, the activity was mostly characterized by recurrent rapid lava-dome growth and collapses, accompanied by numerous block and ash flows that threatened the local settlements up to 15 km from the crater (Cronin et al., 2013; Genareau et al., 2014; Jenkins et al., 2013; Komorowski et al., 2013; Surono et al., 2012). On 5 November, a series of paroxysmal dome explosions and collapses generated several high-energy pyroclastic density currents (PDCs) that inundated an area of 22 km^2, depositing ~ $5x10^6$ m^3 of material (Komorowski et al., 2013). Although the small volume of the eruptive products in comparison to other climactic phases, this event represents the most disastrous volcanic eruption observed at Merapi since 1872, being responsible for more than 200 deaths and a massive destruction of trees and buildings (Jenkins et al., 2013). The unconfined high-energy PDCs associated with this paroxysmal phase flowed down the southern flank of the volcano for 8.4 km crossing over transverse topographic ridges up to 245 m high, whereas co-genetic valley-confined PDCs continued propagating in the Gendol drainage reaching 15.5 km (Komorowski et al., 2013).

These currents impacted an area of dense vegetation causing the felling of many trees, which orientation is a relevant parameter for determining the dynamics and mobility of the offenders PDCs. Through an extensive study of satellite imagery and fieldwork, Komorowski et al. (2013) reconstructed the complex flow direction pattern of the high-energy PDCs as a result of their interaction with a marked topography. They argue that the strongly directional tree blowdown and the distinctive bipartite nature of the high-energy PDC deposits, which are characterized by a lower coarse-grained, fines-poor massive and chaotic unit overlain by a finer-grained, fines-rich laminar to low angle cross-stratified unit, are marked features shared with other historical blasts, suggesting that the paroxysmal event was also a directional laterally-directed blast-like explosion. Moreover, Jenkins et al. (2013) used the evidence of damages to trees and buildings to derive the dynamic pressure

evolution across the impact area of the high-energy PDCs, which were able to exert significant dynamic pressure (≥ 10 kPa) over distances of 5 – 6 km from the crater, despite their unconfined setting. Other studies have also used the damage to trees to infer velocities (and hence dynamic pressures) of other historical Merapi eruptions (Clarke and Voight, 2000; Kelfoun et al., 2000). Cronin et al. (2013) interpreted the energetic event of 5 November as an extremely hot and mobile block and ash flow (able to develop several decoupled surges) generated by the collapse of a very hot and highly gas charged dome.

The high-energy PDCs associated with the Merapi 2010 paroxysm were also sufficiently hot to char most of the vegetation encountered along their path, entombing and preserving charred fragments within their deposits. Experimental studies have shown that during the charcoalification process, the reflectance of charcoal increases with temperature (Correia et al., 1974; Scott and Jones, 1991; Scott and Glasspool, 2007). Even though reflectance may also increase at a given temperature with time, it has been demonstrated that it stabilized after exposure greater that 4 – 5 h (Scott and Glasspool, 2005), so that it can be used as an indicator of the charring temperature of specimens embedded within PDC deposits. Despite its potential, the study of charcoal fragments has been adopted to determine the emplacement temperature of few historical PDC deposits, including pyroclastic deposits at Soufrière Hills (325 – 525°C, Scott and Glasspool, 2005; 300 – 425°C, Scott et al., 2008), Taupo (269 – 398°C, Hudspith et al., 2010), Vesuvius (240 – 370°C, Caricchi et al., 2014) and Fogo (330 – 460°C, Pensa et al., 2015).

A systematic exploration of the thermal state of PDCs (and its spatial variation) provides important insights into the flow dynamics, and enhances our ability to mitigate potential future hazards. However, our knowledge about how quickly the heat is exchanged between the pyroclastic mixture and the external environment is still limited. Estimated emplacement temperatures of PDCs of the recent activity at Merapi have been obtained using different types of proxies. In particular, the use of melting plastics has been adopted to infer the temperature of the associated ash cloud surge of the

block and ash flows emplaced during the 1994 eruption (<200°C, Voight and Davis, 2000), and the 2006 eruption (<165°C, Charbonnier and Gertisser, 2008). Jenkins et al. (2013) estimated low temperatures (200 – 300°C) for the high-energy PDCs emplaced on 5 November both in proximal and distal localities. They used a series of scattered evidences, such as photographs of injuries, building damages and field observations (i.e. heat effects on manmade objects and vegetation) to show that communities situated along the Gendol river at about 12 km from the crater were invaded by dilute PDCs with low dynamic pressure but sufficiently high temperatures to cause injuries and dead. However, the high extrusion rate (~ 25 m^3 s^{-1}; Pallister et al., 2013) of the new dome that collapsed on 5 November, which was built between 2 and 4 November, suggests a large supply of thermal energy available for the associated high-energy PDCs, likely due to the fact that it was very hot at that time (Cronin et al., 2013). This leads to the question: which is the main process, between the flow source system and that of transport, responsible for the sudden temperature drop?

Here we address this question by investigating the spatial variation of charring temperature of plant materials, which were preserved within the high-energy PDC deposits of 5 November.

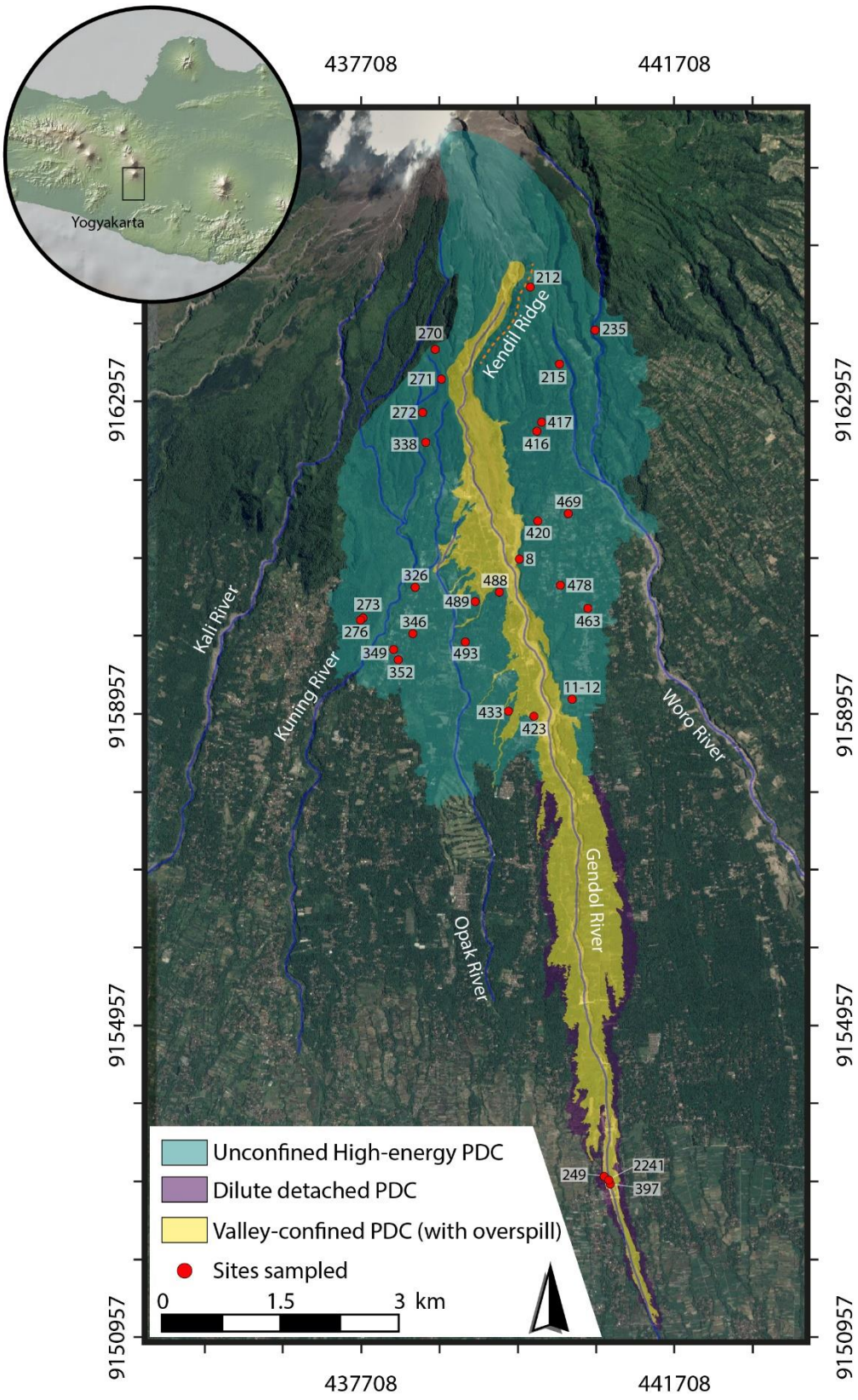

Fig. 2.1. *Map showing the distribution of PDC deposits from the 5 November 2010 eruption at Merapi (simplified from Komorowski et al., 2013), and the sites sampled in this study. The inset box indicates the location of Merapi volcano in Central Java.*

2.2. Materials and Method

Several charcoal fragments were collected from 29 sites by JCK (Fig. 2.1), of which all belong to a single depositional unit that Komorowski et al. (2013) interpreted to be related to the third explosion of Stage 4 (U1), which emplaced both unconfined and co-genetic valley-confined lithofacies. To examine the potential thermal evolution of the high-energy PDCs in relation to topographic changes, sampling sites were placed in different topographic settings (i.e. ridge tops, interfluves and deep channels) across the impacted area, and at varying distances from the source (from ~ 2.1 to ~ 13.5 km). In particular, ten sites (212, 215, 417, 416, 420, 469, 8, 478, 463, 11-12) were sampled from deposits related to the unconfined PDCs that partially spilled over both the Kendil Ridge and the Gendol valley, and continued propagating southward along the Gendol-Woro interfluve. These samples were collected along a N – S transect at distances of ~ 2.1 to 7.3 km from the summit. One sample (235) was taken from deposits formed by unconfined PDC lobes in the east side of the Woro drainage (~ 2.8 km from the vent). Eight sites (270, 271, 272, 338, 326, 346, 349, 352) were sampled in the right side of the Opak river through a NE – SW transect ~ 4 km long. Here the deposits represent unconfined PDCs that detached from the main axial flow direction of the Gendol channel and overpassed a series of subparallel ridges (i.e. the western walls of the Gendol and Opak valleys), spreading onto the Kinarhejo area. Two sites (273, 276) were sampled from deposits situated at the southwest distal edge of the high-energy PDC impact area (~ 6.2 km from the volcano), where the flows stopped in the Kuning – Opak interfluve before entering the Boyong drainage. Five sites (488, 489, 493, 433, 423) represent the overbanking deposits that cover the Gendol-Opak interfluve. They are distributed along a N – S transect at increasing distances from the source (from about 5.7 to 7.4 km). Three samples (249, 2241, 397) were collected from valley-confined block-poor concentrated PDC deposits along the Gendol drainage, at ~ 13.5 km from the crater.

Deposits of the high-energy PDCs are generally rich of charred vegetation, which was originally composed mainly by evergreen angiosperm trees, herbs and shrubs (Sutomo and Dini Fardila, 2013).

Pieces of charred branches and trunks (on the order of centimeters) were collected in most of the analyzed deposits. In the absence of macroscopic charcoal pieces, bulk samples were collected directly from the matrix. In these few cases, small fragments of charcoal were found dispersed within the matrix during laboratory analysis.

Charcoal fragments were incorporated in epoxy resin and wet-polished. The polishing procedure was performed adopting grinding papers (grain size of 250, 500 and 1000) and isopropanol lubricant; after then, the samples were polished with alumina powder of grain sizes from 1 to 0.01 μm. Samples were examined through a Zeiss Axioskop 40 microscope under oil of ne = 1.518 at about 23°C, using an Epiplan–Neofluar 50x optics. The incident light source was a tungsten–halogen lamp (12 V, 100 W) filtered at 546 nm. Reflectance measurements (Ro%) were performed using the MPS 200 detection system by J&M Analytik AG in a dark-room. The instrument was calibrated with mono–crystalline standards of spinel (Ro% = 0.426), sapphire (Ro% = 0.595), yttrium-aluminum-garnet (Ro% = 0.905) and gadolinium-gallium-garnet (Ro% = 1.726), prior to the measurements. Calibration was repeated approximately every 2 h of work using a group of three standards that were selected according to the Ro% range measured in the sample. Specimens were also photographed with a microscope–mounted Canon Power Shot G6.

Up to 114 Ro% measurements were randomly selected within each sample in order to calculate the mean Ro% value and its standard deviation.

Table 2.1
Charcoal reflectance data and related temperature estimates for each site.

Site	Lithofacies	Lat (°S)	Long (°E)	D (km)	G	MLRo% ± 1σ	MHRo% ± 1σ	L-T_{emp} (°C)	H-T_{emp} (°C)
212	Unconfined	7° 33.544'	110° 27.292'	2.1	A	0.17 ± 0.04		240 - 284	
215	Unconfined	7° 34.077'	110° 27.494'	3.1	B	0.74 ± 0.15		329 - 358	
417	Unconfined	7° 34.480'	110° 27.370'	3.7	A	0.31 ± 0.03		274 - 306	
416	Unconfined	7° 34.542'	110° 27.337'	3.8	A	0.33 ± 0.03		278 - 315	
420	Unconfined	7° 35.163'	110° 27.344'	4.9	C	0.28 ± 0.04	1.36 ± 0.19	266 - 309	386 - 444
469	Unconfined	7° 35.111'	110° 27.554'	4.9	A	0.36 ± 0.03		285 - 318	
8	Unconfined	7° 35.425'	110° 27.217'	5.4	A	0.36 ± 0.03		285 - 318	
478	Unconfined	7° 35.607'	110° 27.500'	5.8	C	0.25 ± 0.04	1.52 ± 0.22	259 - 306	401 - 458
463	Unconfined	7° 35.766'	110° 27.689'	6.2	A	0.35 ± 0.02		283 - 316	
11-12	Unconfined	7° 36.394'	110° 27.582'	7.3	C	0.36 ± 0.09	1.49 ± 0.26	285 - 318	398 - 456
270	Unconfined	7° 33.976'	110° 26.634'	2.7	A	0.41 ± 0.08		297 - 323	
271	Unconfined	7° 34.181'	110° 26.679'	3.1	A	0.33 ± 0.09		278 - 315	
272	Unconfined	7° 34.412'	110° 26.549'	3.5	A	0.25 ± 0.06		259 - 306	
338	Unconfined	7° 34.619'	110° 26.570'	3.9	C	0.41 ± 0.12	1.12 ± 0.06	297 - 323	364 - 399
326	Unconfined	7° 35.621'	110° 26.496'	5.7	A	0.31 ± 0.03		273 - 312	
346	Unconfined	7° 35.941'	110° 26.480'	6.3	A	0.33 ± 0.05		278 - 315	
349	Unconfined	7° 36.051'	110° 26.348'	6.5	A	0.25 ± 0.08		259 - 306	
352	Unconfined	7° 36.122'	110° 26.380'	6.7	A	0.30 ± 0.04		271 - 311	
273	Unconfined	7° 35.832'	110° 26.137'	6.2	B	0.59 ± 0.17		316 - 342	
276	Unconfined	7° 35.846'	110° 26.119'	6.2	A	0.33 ± 0.04		278 - 315	
488	Unconfined	7° 35.654'	110° 27.078'	5.8	A	0.32 ± 0.02		276 - 313	
489	Unconfined	7° 35.719'	110° 26.911'	5.9	A	0.37 ± 0.10		288 - 319	
493	Unconfined	7° 35.998'	110° 26.843'	6.4	A	0.36 ± 0.03		285 - 318	
433	Unconfined	7° 36.477'	110° 27.141'	7.3	A	0.32 ± 0.04		276 - 313	
423	Unconfined	7° 36.512'	110° 27.317'	7.4	A	0.35 ± 0.02		283 - 317	
235	Unconfined	7° 33.731'	110° 27.752'	2.8	A	0.38 ± 0.05		290 - 320	
249	Valley-confined	7° 39.694'	110° 27.802'	13	A	0.31 ± 0.06		274 - 312	
2241	Valley-confined	7° 39.718'	110° 27.834'	13	A	0.33 ± 0.03		278 - 315	
397	Valley-confined	7° 39.746'	110° 27.844'	13	A	0.34 ± 0.04		281 - 316	

D, runout distance from crater; *G*, samples group; *MLRo%* and *MHRo%* represent the mean low and high reflectance value, respectively; *L-T_{emp}* and *H-T_{emp}* represent the temperature of emplacement related to the *MLRo%* and *MHRo%*, respectively. Temperatures are inferred from experimental curves by Scott and Glasspool (2005, 2007) and Ascough et al. (2010).

2.3. Results

A complete summary of the reflectance microscopy data for each site is provided in Table 2.1. In general, the majority of the collected plant material has a black color, leaves a black streak on hands and paper, and it breaks easily under pressure. Under light microscopy, it also shows varying degree of cell walls homogenization, and therefore can be categorized as charcoal. At one site (212), located in a very proximal region (~ 2.1 km) on top of the Kendil ridge, the sampled vegetation shows a variety of colors ranging from brown to dark-brown to black-brown, indicating that such woody material varies from uncharred to poorly charred, respectively. The uncharred branches and rootlets may have also been heated to temperature up to 200°C, because below this value the reflectance cannot be measured (Scott and Jones, 1991).

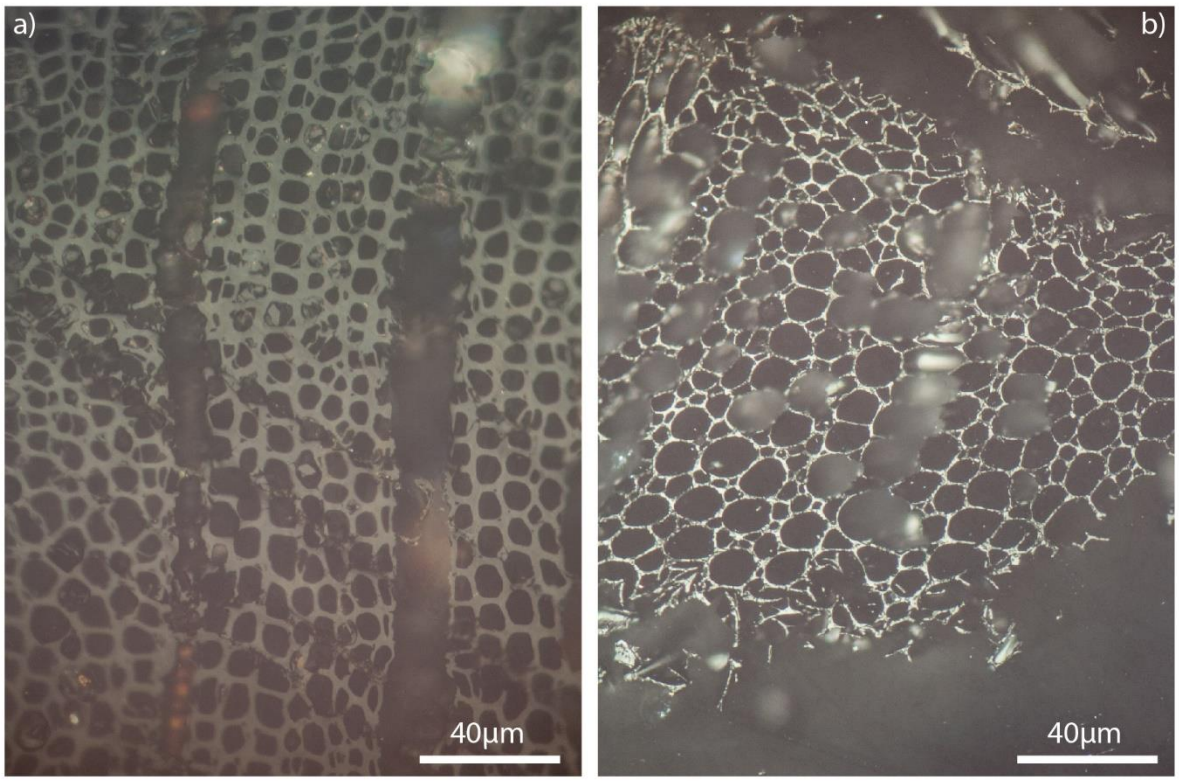

Fig. 2.2. *Reflected light microphotographs of polished blocks under oil showing variable degree of charring.* ***a****) Incompletely charred specimen (from site 270), as evidenced by the cell walls that are not completely homogenized (mean Ro% = 0.36).* ***b****) Fully charred fragment (from site 338) with high homogenized cell walls yielding mean Ro% = 1.42.*

Overall, partially and fully charred fragments are well-preserved within the high-energy PDC deposits at all localities, and their mean Ro% range from 0.17 ± 0.04% to 1.52 ± 0.22% (Fig. 2.2). The samples can be divided into three groups (A to C) based on their Ro% distribution. Group A samples are those showing a narrow and well-defined Gaussian distribution in reflectance values, with very small standard deviation (Fig. 2.3A-H). Here, the specimens are characterized by a poor homogenization of the cells, and yield mean Ro% values that vary between 0.17 ± 0.04% and 0.41 ± 0.08%. Most of the localities studied (about 79%; Table 2.1) present specimens belonging to this group. In particular, group A samples occur widely throughout the spatial extent of the unconfined PDC deposits, regardless of their topographic location and their distance from the crater. At distal localities, the valley-confined PDC deposits record the same degree of charring observed in proximal unconfined lithofacies.

Group B samples are those that contain charred woody fragments displaying a larger range in Ro% than that observed in group A (Fig. 2.3I, L), with mean Ro% values ranging from 0.59 ± 0.17% to 0.74 ± 0.15%. The frequency histograms show a high standard deviation, which may be due to the overlap of two Gaussian distributions that are difficult to separate. The two sites (about 7%; Table 2.1) that contain charcoal fragments associated with Group B are found sporadically in unconfined PDC deposits located in the Kuning (273) and Woro (215) rivers.

Samples of group C (about 14%, Table 2.1) show two main clusters of Ro% values identifiable by two distinct Gaussian distributions (Fig. 2.3M, N). Here, there is the coexistence of specimens with both low and high homogenization of the cell structure, with mean Ro% ranging from 0.25 ± 0.04% to 0.41 ± 0.12%, and from 1.12 ± 0.06% to 1.52 ± 0.22%, respectively. This bimodal distribution is not observed within the individual specimens, since Ro% value of the central area is similar to that of the edge, but related to the presence of specimens with different degrees of charring in the same sampled site. This feature in the data are observed in unconfined PDC deposits at few sites in the Gendol-Woro interfluve (420, 478, 11-12), and at one site in the Opak drainage (338).

The examples in Fig. 2.3 highlight that the predominant symmetrical peak observed in group A samples is also present in samples of group B and C.

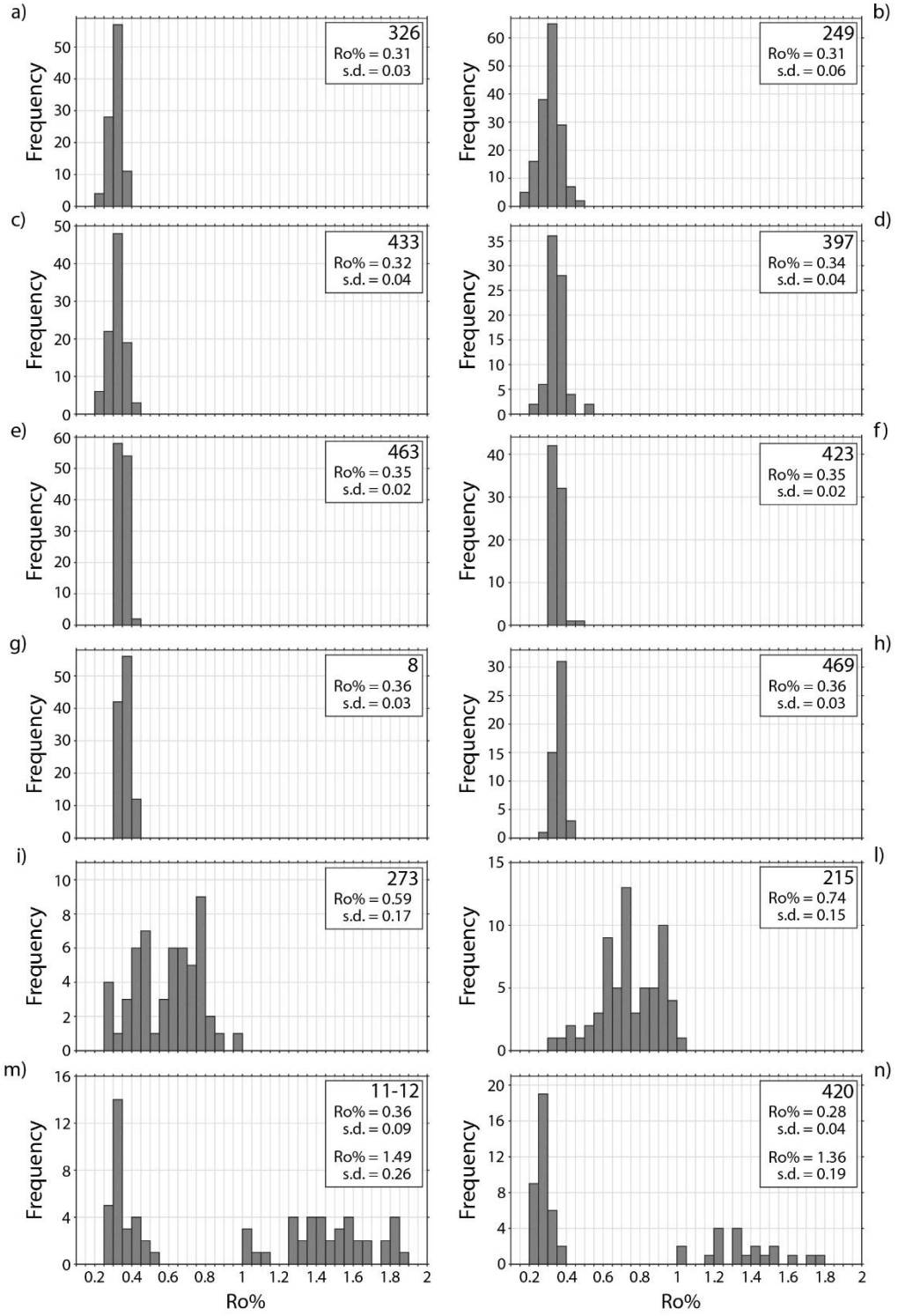

Fig. 2.3. *Results of optical analyses are shown in terms of frequency histograms of Ro% values. Three groups have been identified.* ***(a-h)*** *Group A samples are those that show a well-defined Gaussian distribution in Ro% data, with very small standard deviation.* ***(i-l)*** *In Group B specimen, the Gaussian*

*distribution is less defined because of the large variation in Ro% possibly due to the overlap of different Ro% families. (**m-n**) Group C samples are those yielding a distinct bimodal pattern of Ro%. The mean Ro% value as well its standard deviation is reported in the inset of each sample.*

2.4. Discussion

2.4.1. Determining the temperature of the high-energy PDC deposits

Here we use the experimental curves proposed by Scott and Glasspool (2005, 2007) and Ascough et al. (2010) to convert Ro% into temperature values. Scott and Glasspool (2005, 2007) performed a series of charring experiments using branches of *Sequoia sempervirens* to build an empirical Ro% vs temperature curve. Experimental data from woods of *Pinus sylvestris* and *Rhizophora apiculate* were used by Ascough et al. (2010) to extrapolate similar relationship. As discussed by Ascough et al. (2010) and Hudspith et al. (2010), no meaningful difference can be observed in reflectance values between angiosperms and gymnosperms for the same temperature conditions. Moreover, Scott and Glasspool (2007) showed that the experimental Ro% - T curve determined for the bracket fungus *Ganoderma* sp lies close to that of the *Sequoia sempervirens*, although the former is not likely to contain lignin in its structural cells (Paterson, 2006). We therefore assume that these curves can be applied to our samples, which are most likely an ensemble of different angiosperms species, although their taxonomical identification is outside the purpose of this paper. Because of different experimental procedure, the above authors obtained slightly different temperature value for a given Ro%. We therefore prefer to use the range of temperature defined by the combination of these curves as our best estimate of the PDC emplacement temperature (Fig. 2.4).

Our Ro% results show evidence that the samples experienced different degrees of charring, suggesting either that PDCs were thermally heterogeneous, or that some specimens did not equilibrate with the hot flow due to the short time-scale of the charring process. In particular, group A samples are well-clustered in a narrow peak at about Ro% of 0.32 yielding temperatures between 240 – 320°C.

Charcoal fragments of group B, instead, present higher Ro% values that translate into temperature of emplacement of 316 – 358°C. Ro% data of group C reveal the presence of two marked populations of charcoal materials, where the lowest and highest mean Ro% values indicate temperatures of 259 – 323°C and 364 – 456°C, respectively.

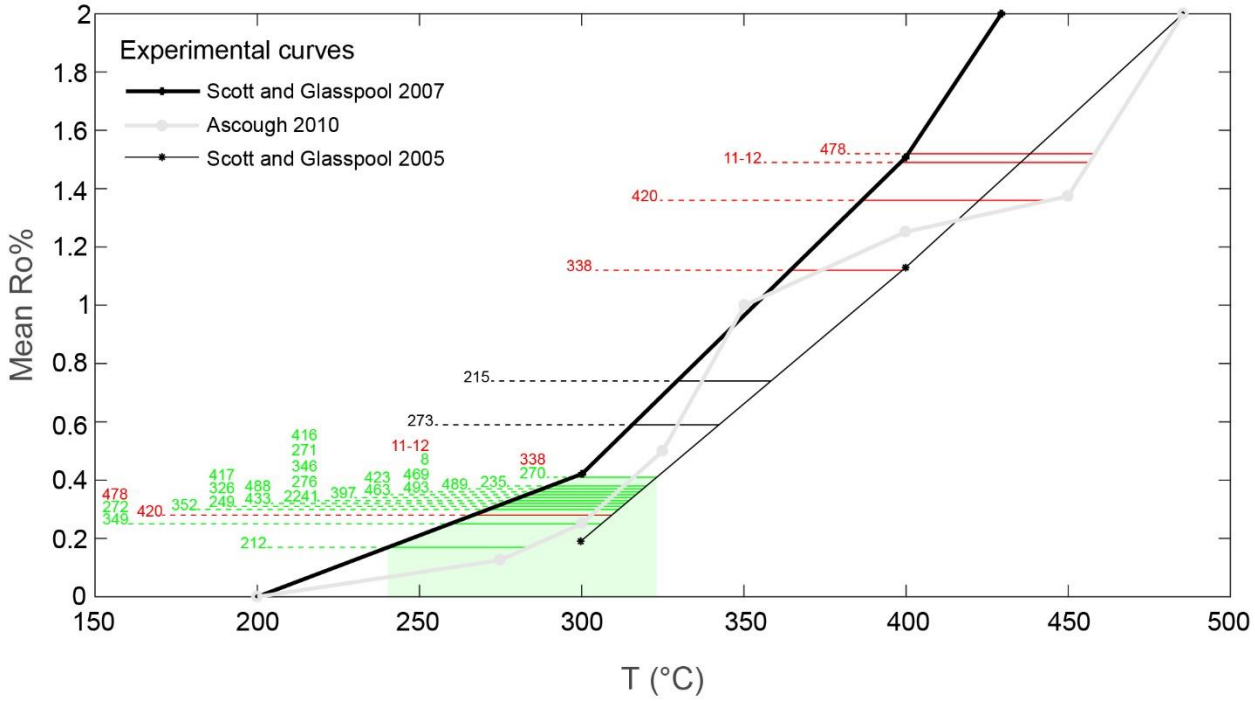

Fig. 2.4. *Conversion of Ro% data into paleo-temperatures. Ro% values are converted into temperature values adopting the experimental curves for Sequoia sempervirens and Pinus sylvestris, after Scott and Glasspool (2005, 2007) and Ascough et al. (2010), respectively. For a given Ro% value, the temperature interval defined by the combination of these curves (colored solid line) is assumed here as an estimate of the mean PDC emplacement temperature at that location. Green, black and red lines represent samples of group A, B and C, respectively. The green shaded area indicates the minimum emplacement temperature for the 5 November PDC.*

A possible explanation of this thermal heterogeneity may reside in the different contact time interval between the vegetation and the hot flow. Some plants may have been subjected to a brief high temperature heating to prevent the acquisition of the equilibrium condition, whereas others remained

long enough to acquire it. However, all but one (212) of the collected samples were totally enclosed within the deposits, so that they were held in hot ash for a considerable time. Direct measurements of the temperature of some PDC deposits showed that they retained their hot thermal character for several days to months after deposition (Banks and Hoblitt, 1996), which is a considerable amount of time for the charcoal to keep a stable thermal signal (Scott and Glasspool, 2005). Furthermore, the thermal state of the high-energy PDC deposits are derived from Ro% measurements related to small-sized charcoal fragments, which are most likely inclined to achieve rapidly the equilibrium temperature. This is testified by the fact that the majority of the samples yield well-clustered Ro% data (group A). Site 212 is distinct because it contains some uncharred plants that were taken at the interface between the high-energy PDC deposit and the underlying soil, where the flow was probably being cooled by the erosive interaction with wet soil.

The internal temperature pattern of a single PDC may be complex, and is likely to be a function of the thermal behavior of all its constituents (juvenile and lithic clasts, magmatic gases and external fluids, such as air and water). The ash-sized juvenile particles should be able to exchange heat efficiently with the surrounding components, so that they can be considered thermally (and mechanically) coupled with the carrying gas phase. Bomb-sized clasts, instead, are likely to be able to retain their initial temperature for several hours (cf. Cioni et al., 2004). The analyzed charcoal specimens are mostly contained in the lowermost unit of the high-energy PDC deposits, which represents the coarsest layer being dominantly made of lapilli (2-64 mm) but also ranging from block and bomb (> 64 mm) to coarse ash (0.062-2 mm). We therefore infer that the contrasting thermal signal recorded by few samples of group C, as well as the high Ro% variability observed in group B, are likely connected with the thermal disequilibrium attained during the emplacement process between clasts of different grain size. We suggest that the Ro% values of the main peak characterizing group A, which are also present in group B and C, are associated to specimens that have reached equilibrium with surrounding ash matrix. In contrast, the higher Ro% values correspond to regions of the deposit where the thermal influence of large clasts is more pronounced. This means, therefore,

that the minimum emplacement temperature of the high-energy PDCs was between 240 and 320°C (Fig. 2.4). These values are in excellent agreement with the temperature proposed by Jenkins et al. (2013).

2.4.2. Thermal evolution of the high-energy PDCs

According to the charcoal data presented here, the high-energy PDC was emplaced over a wide area of contrasting topography conditions maintaining a fairly homogeneous temperature, although its dynamics constantly evolved along the flow path as a results of its interaction with an irregular terrain morphology. Figure 2.5 shows the inferred temperature values for each locality. From this figure, it is clear that there are no appreciable differences in the degree of charring between the distal valley-confined PDC deposits and those of the unconfined lithofacies.

Given that several block and ash flows had occurred since October 26 and that they had already knocked down and charred part of the living vegetation, it may be argued that the previously formed charcoal could have been transported within the subsequent high-energy PDCs of 5 November, affecting its temperature estimation. However, it is important to note that the Ro% value of charred specimens is not reversible, but relates to the highest temperature experienced since it can be overprinted only by subsequent charring at higher temperatures (McParland et al., 2009). Assuming that some woody plants were reworked, this leads to the following hypotheses. The first is that if the temperature of the high-energy PDCs of 5 November was higher than those of PDCs generated during previous eruptions, our samples would have recorded the thermal overridden of the last event. On the other hand, if the high-energy PDCs of 5 November were cooler, our proposed temperature may overestimate their actual thermal state. Regardless of which hypothesis is correct, it is important to emphasize that our data highlight a thermal signal that is homogeneously distributed across topography and it is far below magmatic temperatures.

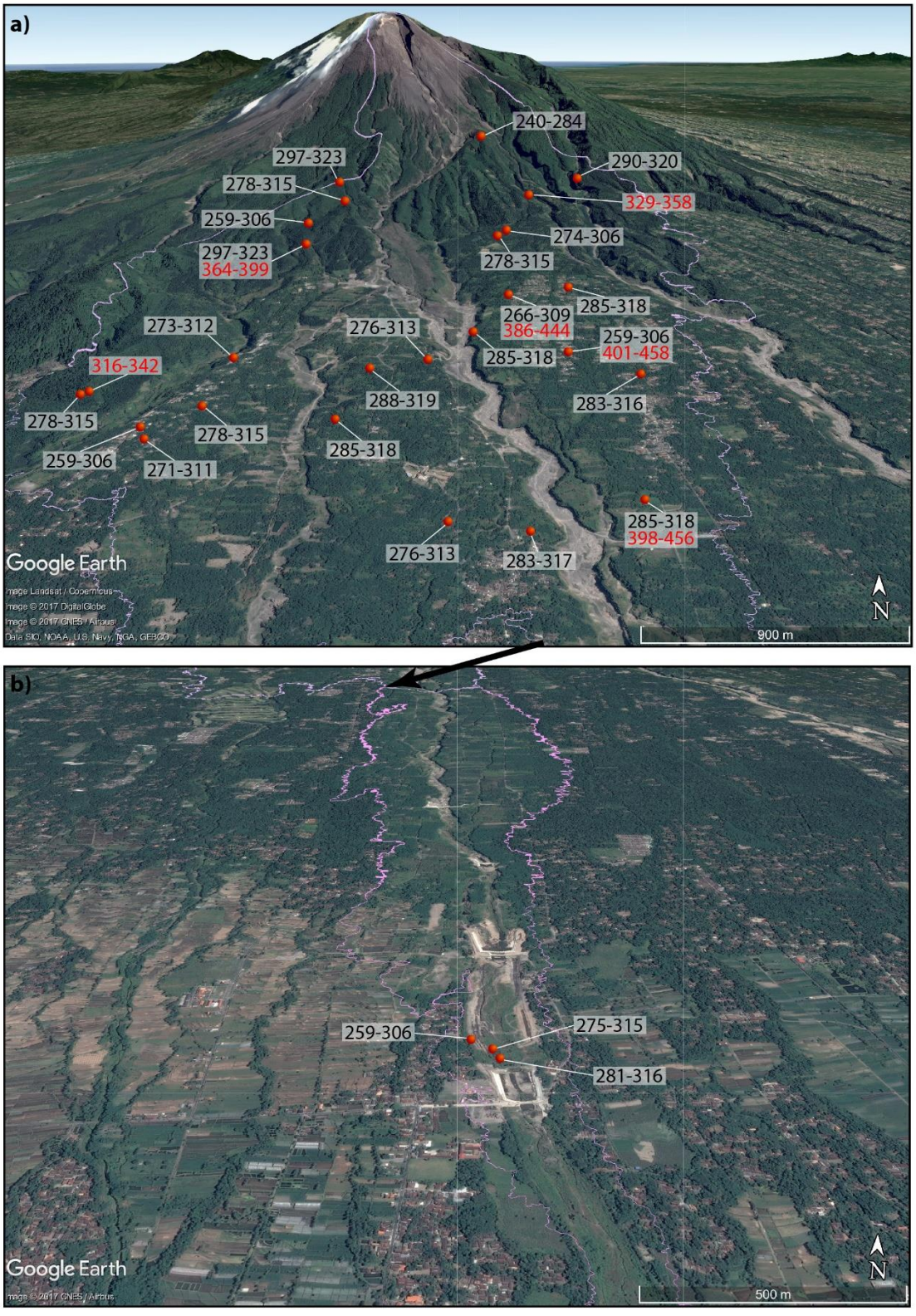

Fig. 2.5. *Areal distribution of the emplacement temperature for PDC deposits in (**a**) proximal (inundation area of the unconfined high-energy PDC) and (**b**) distal (valley-confined) region. Temperatures in red are related to samples of Group B and C.*

Assessing the temperature of PDCs formed by dome collapse is complicated by the fact that it is unknown the extent of cooling of the lava crust before detaching from the lava dome. At the time of gravitational collapse, the outer margin of the dome could be hot, warm or even cold. As far as we know, temperatures of block and ash flow deposits may vary substantially, largely because they reflect the broad thermal range that is associated to the dome source materials (Uehara et al., 2015). Although this possible thermal heterogeneity, block and ash flow deposits are generally found at high temperatures because of their typical valley-confined behavior (Cole et al., 2002; Uehara et al., 2015; Voight and Davis, 2000). Voight and Davis (2000) inferred that the 1994 channeled block and ash flows at Merapi were emplaced at temperature of about 550°C, whereas detached surge deposits were below 200°C, highlighting the efficiency of the heat exchange between the ash cloud and the external atmosphere. A similar result was obtained by Charbonnier and Gertisser (2008), which estimated 400°C for the block and ash flow deposit and about 165°C for the associated ash cloud surge. In case of the 2010 paroxysmal activity at Merapi, the temperature of PDC deposits seems to have not been modulated by changes of the flow concentration arising from the interaction with a complex topography. Nevertheless, our temperature estimations are significantly lower than those that might be associated with hot dome-generated PDCs. The high magma extrusion rates estimated during 1 – 4 November (~ 25 m^3 s^{-1}; Pallister et al., 2013) suggest that the largest part of the dome that collapsed on 5 November was made of fresh magma, and therefore, its initial temperature was likely close to magmatic temperature (around 900°C; Costa et al., 2013). As a consequence, the thermal state of the associated PDCs should be much higher than that indicated by our data. A possible explanation of a fast cooling of the pyroclastic mixture may be related to the rapid expansion that characterizes the blast phenomena. However, the expansion process in the blast can be approximated fairly accurately to be isothermal, since the effective value of the ratio of specific heat for the gas-pyroclast mixture ($1 + y_w R_w T/C_v$, where y_w is the water content, T the magma temperature, R_w is the vapor gas constant (~462 J/kg/K), and C_v is the specific heat of the gas-pyroclast mixture (~1×10^3 JK^{-1} kg^{-1})) is nearly 1. Given that the velocity associated with free decompression is at most twice of sound

velocity ($2\sqrt{y_w R_w T}$, Woods and Bower, 1995), the kinetic energy gain per unit mass due to expansion is expected to be $\sim y_w R_w T$. Considering that this kinetic energy is supplied from the thermal energy $C_v \Delta T$, the magnitude of temperature drop ΔT is estimated as follows:

$$\frac{\Delta T}{T} \sim \frac{y_w R_w}{C_v} \sim 10^{-2}$$

This implies that such a mechanism cannot decrease the temperature of the pyroclasts itself. We therefore propose that the gravitational collapse of the expanded material is the most likely process that accounts for this sudden temperature drop (Fig. 2.6). We hypothesize that during this collapsing phase, an efficient turbulent mixing with cold atmospheric air may have occurred, thus playing an important role in decreasing the temperature of the hot pyroclastic mixture. It is clear that such possible explanation need a deeper analysis potentially using numerical models that provide more rigorous and quantitative information.

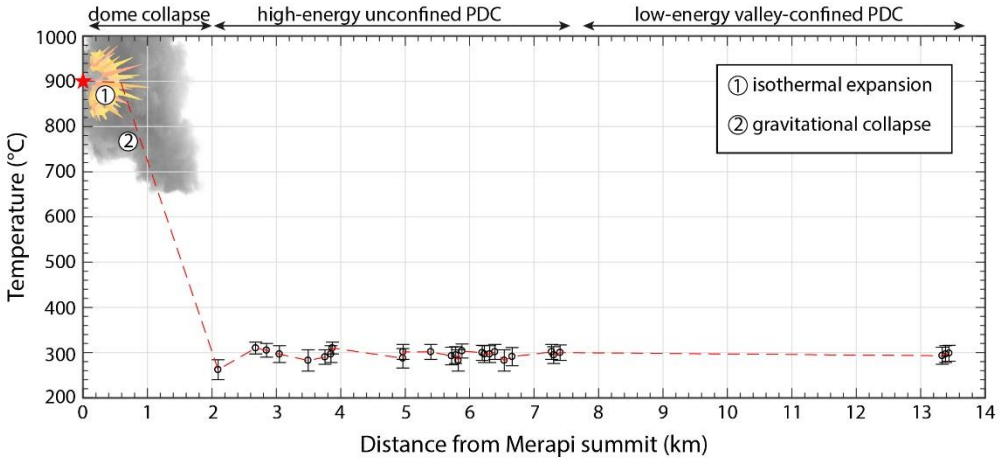

Fig. 2.6. *Emplacement temperature variation as a function of the distance from source for the unconfined high-energy and co-genetic valley-confined PDC deposits of 5 November eruption. The red star marks the inferred initial temperature of the dome before the paroxysmal event.*

However, our data have revealed a fairly homogeneous thermal signal across the entire impacted area of the high-energy PDCs, indicating that the flow transport system was not sufficiently efficient in mixing and cooling, although the strong interaction of such currents with a marked topography. Hence, as observed in other type of PDCs (Banks and Hoblitt, 1996; Porreca et al., 2008; Trolese et al., 2017; Zanella et al., 2015), once the PDC has formed, it is able to maintain its inherited thermal state away from the source both in channelized and unconfined regime.

2.5. Conclusion

We have presented reflectance data of charcoal fragments preserved within the high-energy PDC deposits emplaced during the 5 November 2010 event, the most disastrous volcanic eruption observed at Merapi since 1872. Reflectance data are mostly clustered in low values ranging from 0.17 ± 0.04% to 0.41 ± 0.08%, whereas few specimens yielded higher values suggesting disequilibrium state of the deposits induced by hot bomb-size juvenile clasts. The lower values translate to minimum charring temperature in the range of 240 – 320°C, which is in good agreement with those previously estimated by Jenkins et al. (2013). These temperature data are ubiquitously distributed throughout most of the impact area of the paroxysmal PDC, indicating that the flow transport system was unable to lower the transported thermal energy notwithstanding the flow evolved in its dynamics as it propagated over a complex terrain along the path. The high extrusion rates at which the dome that collapsed of 5 November was built during 1 – 4 November suggest high temperatures available for the associated PDCs, likely much higher of those we have estimated. We therefore identify the inferred blast-like process associated with this paroxysmal event as the likely mechanism leading to the sudden temperature drop. Although data unequivocally need a mechanism for justify a very early and string temperature drop, the hypothesis of the blast as a temperature-dissipation process remains untested and requires further quantitative numerical investigations to be validated.

Chapter 3

Thermal regime of column collapses and controls on initial temperature of pyroclastic density currents

Note – In preparation for submission as a short-communication research article:

Trolese, M., Cerminara, M., Esposti Ongaro, T., Giordano, G. Thermal regime of column collapses and controls on initial temperature of pyroclastic density currents

Abstract: The temperature of pyroclastic density currents (PDCs) is one of the main hazards for communities and infrastructures surrounding volcanoes. Our current understanding of thermal transport in PDCs is, though, still very limited. PDC deposits are known to vary from extensively welded to totally unwelded with emplacement temperatures close to ambient. The reasons for such great diversity are debated in terms of eruptive vs transport and emplacement processes. Here we present three-dimensional numerical simulations to understand the controls of different column collapse regimes on PDCs. We find that the initial temperature of PDCs is linearly correlated with the amount of mass involved into the collapsing phase, and it can be decreased by up to 45% of the starting magmatic temperature in the case of incipient column collapse. This trend is observed independently of the simulated mass discharge rates. Our results suggest that an important imprint to the thermal character of PDCs is provided by the percentage of column collapse.

3.1. Introduction

Pyroclastic density currents (PDCs) range from small-volume short-lived phenomena, commonly generated by the partial collapse of a sustained column, to voluminous long-lived currents resulting from the greatest caldera-forming eruptions known on Earth. Their hot thermal character represents a serious hazard to human settlements, thus posing the attention of the scientific community into the mitigation of their impacts. Available data show that PDC deposits exhibit a wide gamut of emplacement temperatures, ranging from extensively welded to totally unwelded deposits (Fig. 3.1). Small-volume PDC deposits (≤ 1 km^3) show a much larger thermal variability, compared with large-volume ignimbrites that appear to cluster around high temperatures (Fig. 3.1). Few data document the lateral variation of PDC deposits' temperature and indicate substantial conservation of thermal energy along flow path (Banks and Hoblitt, 1996; Lesti et al., 2011; Porreca et al., 2008; Trolese et al., 2017; Zanella et al., 2015). As a consequence, the origin of the temperature drop from initial magmatic temperature has been qualitatively correlated with possible effects of air entrainment during column collapse processes (Benage et al., 2016; Cioni et al., 2004). Such a qualitative relationship is intuitive, but the possible quantitative correlation between eruption dynamics, collapse regimes and the consequent thermal imprint on PDCs have never been addressed.

In the last years, increasing modelling and computational capabilities have progressively enabled the study of the dynamics of turbulent volcanic plumes (Cerminara et al., 2016a; 2016b; Suzuki and Iguchi, 2017; Suzuki and Koyaguchi, 2010). A recent, broad initiative by the International Association of Volcanology and Chemistry of the Earth Interior (IAVCEI) aimed at quantifying the reliability of volcanic plume models (Costa et al., 2016; Suzuki et al., 2016) has demonstrated that numerical models can reproduce, with quantifiable uncertainty, the dynamics of turbulent mixing leading to transition to convective plumes. Unstable regimes eventually leading to partial collapses were also recognized (Cerminara et al., 2016b; Esposti Ongaro et al., 2008; Suzuki and Koyaguchi, 2012), which can explain several depositional features observed in the field (Di Muro et al., 2004)

and characterized in the laboratory (Carazzo and Jellinek, 2012; Carazzo et al., 2015). In this study, we use a 3D flow model to specifically characterize them quantitatively in terms of the percentage of collapse with respect to the mass eruption rate. We then establish a relationship with vent conditions and show that there is a strong correlation between the percentage of collapse and the temperature of incipient PDCs. To this purpose, Large Eddy numerical simulation (LES) are performed by using the ASHEE 3D model (Cerminara et al., 2016a; 2016b). The model is suited to simulate the large-scale features of polydisperse gas-particle mixtures of gas and pyroclasts, including preferential concentration (i.e., non-homogeneous clustering in turbulence) and gravitational settling of particles. Boundary conditions represent the (stationary) injection of an initially homogeneous gas-pyroclasts mixture from a circular vent into a stratified atmosphere. Inlet conditions are univocally determined by imposing 1) (over)pressure and a choked flow constrain at the conduit exit; 2) the mixture gas content; 3) temperature and 4) the mass eruption rate (Supplementary Method A). For overpressured flows, inlet conditions after isentropic decompression are computed following Woods and Bower (1995), thus disregarding the effects of non-homogeneous decompression patterns occurring in supersonic jets (Ogden, 2011; Carcano et al., 2014). All simulations are run with particles of two sizes, which represent coarse (500 μm) and fine ash (50 μm), in equal proportions, to quantify the effects of kinematic decoupling on the dynamics of turbulent plumes.

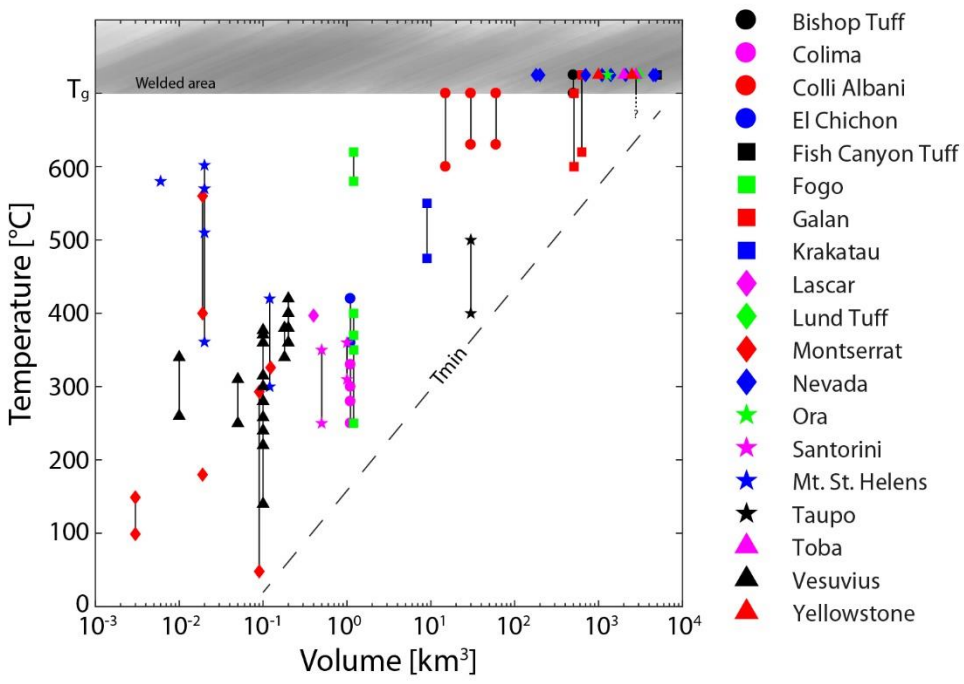

Fig. 3.1. *Collection of PDC deposits temperatures data. PDC emplacement temperatures data are plotted as a function of their respective estimated volume. Full references to the data sets used in the graph are reported in the Supplementary Table 3.2. Dome-generated and phreatomagmatic PDC deposits were discarded from the analysis.*

3.2. Results and discussion

Numerical simulations reproduce the full spectrum of volcanic column regimes, from fully convective plumes to total collapsing fountains generating PDCs. Incipient partial and total collapse regimes are shown in Fig. 3.2. Between them, a range of different collapse regimes occur. For these end-members, we determine the role of turbulence and mixing in decreasing the temperature of the collapsing mass. In Fig. 3.2A, C we present the partial column collapse end-member (U_0 = 202 m s^{-1}, ρ_0 = 9.6 kg m^{-3}, T_0 = 1123 K and r_0 = 127 m). In particular, Fig. 3.2A shows an instantaneous and incipient column collapse that releases a batch of mass, observed intermittently throughout the simulation time. At about 1 km above the vent, the inner and hotter parts of the column start to be affected by turbulent large eddies that progressively erode the central unmixed laminar jet. This turbulence of the column favors the entrainment of cold atmospheric air, which expands by heating causing the dilution of the

mixture (Supplementary Fig. S3.1A, C). The degree and extent of this erosion process determine the quantity of mass involved into the collapse phase (i.e. the stronger the erosion, the minor the collapsing mass). Given that the erosion process does not involve the entire central structure before the upward momentum of the mixture is fully exhausted (defined here as uneroded height H_{un}; see below and Fig. 3.2C), the unmixed part of the column collapses toward the ground from a height of about 2.8 km (defined here as collapse height H_c; see Fig. 3.2C; Supplementary Method B). At the same time, the outer mixed portion of the column becomes buoyant and forms a convective plume that reaches about 38 km (not shown in Fig 3.2). During the collapse, the mixture continues entraining ambient air and diluting. Depending on the amount of mixing, it may either be re-entrained into the eruptive column or remain denser than the ambient air forming a PDC.

To better distinguish the effects of turbulence from those of fluctuations, we averaged the mixture properties through both time and space. From Fig. 3.2C (left panel), which shows the time-averaged temperature field of the mixture normalized to its initial value, it is evident that the jet is characterized by a hot inner core surrounded by a region of gradually decreasing temperature. It is determined, from the ratio between the minimum inflection point of the positive mass flow rate and the mass flow rate at the conduit exit (Supplementary Method B), that the percentage of mass tending to collapse from the column and feeding PDCs is 15% of the mass leaving the source. In the collapsing region, the integrated mean temperature value is estimated at 790 K (Supplementary Method B). Figure 3.2C (right panel) illustrates the time-averaged velocity and temperature profiles both along the vertical z-axis (black and red dashed line, respectively) and averaged across horizontal cross sections (black and red solid line, respectively). These profiles allow us to differentiate the height at which the vertical momentum of the central uneroded z-axis is exhausted (H_{un}) from the one at which the vertical momentum of the whole eruptive column is exhausted (jet height H_{jet}). The time-averaged and horizontally integrated upward velocity decreases until it reaches its minimum value at about 2.2 km (H_{jet}), while along the central z-axis the velocity fall to zero at about 3.1 km (H_{un}). The notable

difference of these heights highlights the effect of dilution of the eruptive column due to the gradual outer mixing with external air, which is responsible for the observed temperature drop.

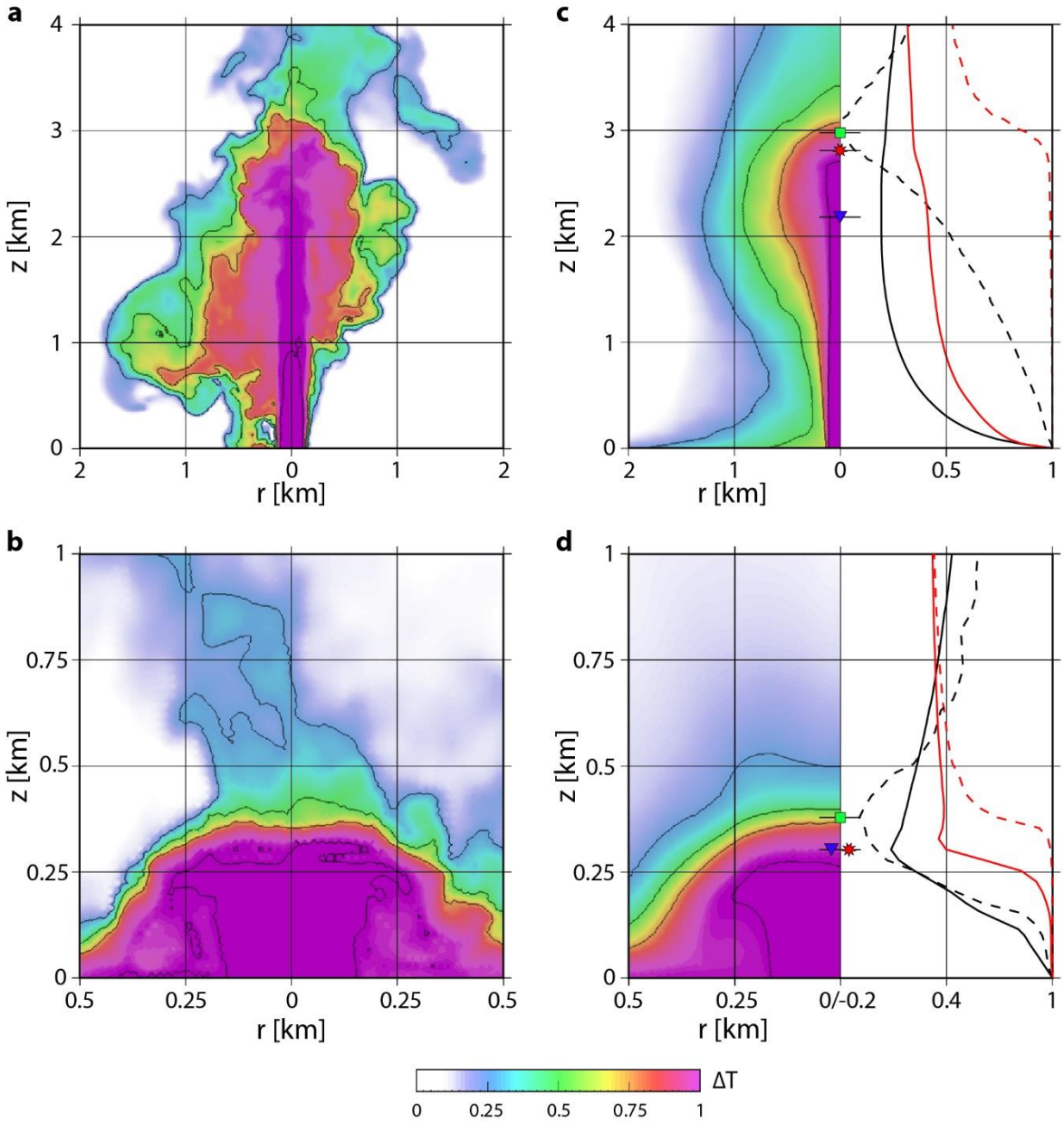

Fig. 3.2. *Comparison between the internal structures of the two column collapse end-members.* ***a-b****, Cross-sectional images showing the instantaneous distribution of the temperature difference relative to the stratified atmospheric temperature at the same vertical position normalized to the initial temperature, at 100 s and 315 s respectively. Isosurfaces correspond to* $\Delta T = 0.25, 0.5, 0.75, 0.999$. ***c-d****, Same as* ***a-b****, but in a time-averaged domain. Black and red lines represent time-averaged velocity (vertical component) and temperature profiles, respectively. Profiles along the vertical axis are dashed, whereas horizontally integrated quantities are solid. All the values are normalized by*

using the initial conditions. The averaging window is from 500 to 1000 s. The symbols represent the uneroded (H_{un}; green square), collapse (H_c; red star) and jet (H_{jet}; blue triangle) heights.

Numerical results for the near total collapse end-member (U_0 = 72 m s^{-1}, ρ_0 = 19 kg m^{-3}, T_0 = 1123 K, r_0 = 151 m) reveal an internal structure of the jet characterized by a symmetrically collapsing fountain (Fig. 3.2B). Here, the velocity integrated throughout time and space is almost similar to that along the central z-axis (Fig. 3.2D, right panel), indicating that the mixing effect is not vigorous enough to erode the eruptive column. Consequently, the H_{jet} and H_{un} are very close to each other, ranging from about 300 to 380 m respectively. The mixture remains at high temperature and high density until it reaches about 300 m where it starts to spread radially, forming a large-scale eddy (Fig. 3.2B, Supplementary Fig. S3.1B, D). Notwithstanding the ingestion of atmospheric air promoted by the large-scale eddy, the continuous feeding of mass from the collapsing jet does not allow the mixture to dilute, leaving it denser than the atmosphere, with solid mass fraction and temperature comparable to the vent conditions. This end-member scenario results in a total collapse (H_c ~ 300 m; Supplementary Method) with generation of PDCs of long run out, whereas a small amount of material becomes buoyant and reaches about 19 km (not shown in Fig. 3.2). The snapshot of the time-averaged temperature field is similar to that of the instantaneous temperature, highlighting that fluctuations are weaker in presence of total collapse (indeed turbulent fluctuations are closely related to dilution intensity or, equivalently to entrainment rate). In this region, the percentage of collapsing mass (net of the mass going into co-ignimbrites) is estimated at 79% of the mass leaving the vent, and its mean temperature is 1050 K (Supplementary Method B).

Figure 3.3A shows the variations of all the heights described above as a function of the percentage of collapse, providing an insight into the jet dynamics. These variations confirm that the dynamics and efficiency of air entrainment play an important role in controlling the collapse regime (Esposti Ongaro et al., 2008; Suzuki and Koyaguchi, 2012; Woods, 1995). For percentage of collapse >50% the

erosion of the jet structure related to air entrainment does not affect significantly the properties of the ascending eruptive column, in which the upward momentum of the mixture becomes exhausted at almost the same low height for both the central uneroded and the outer jet region (H_{un} ~ H_{jet}), leading to a low collapsing height. Lower percentages of collapse, on the contrary, are related to efficient mixing between the ejected mixture and ambient air that rapidly decelerates the upward velocity of the material within the annular mixing region of the eruptive column, whereas the central unmixed axis continues to rise upward until its velocity falls to zero, forming a fountain-like structure (Suzuki and Koyaguchi, 2012) that leads to higher collapse height.

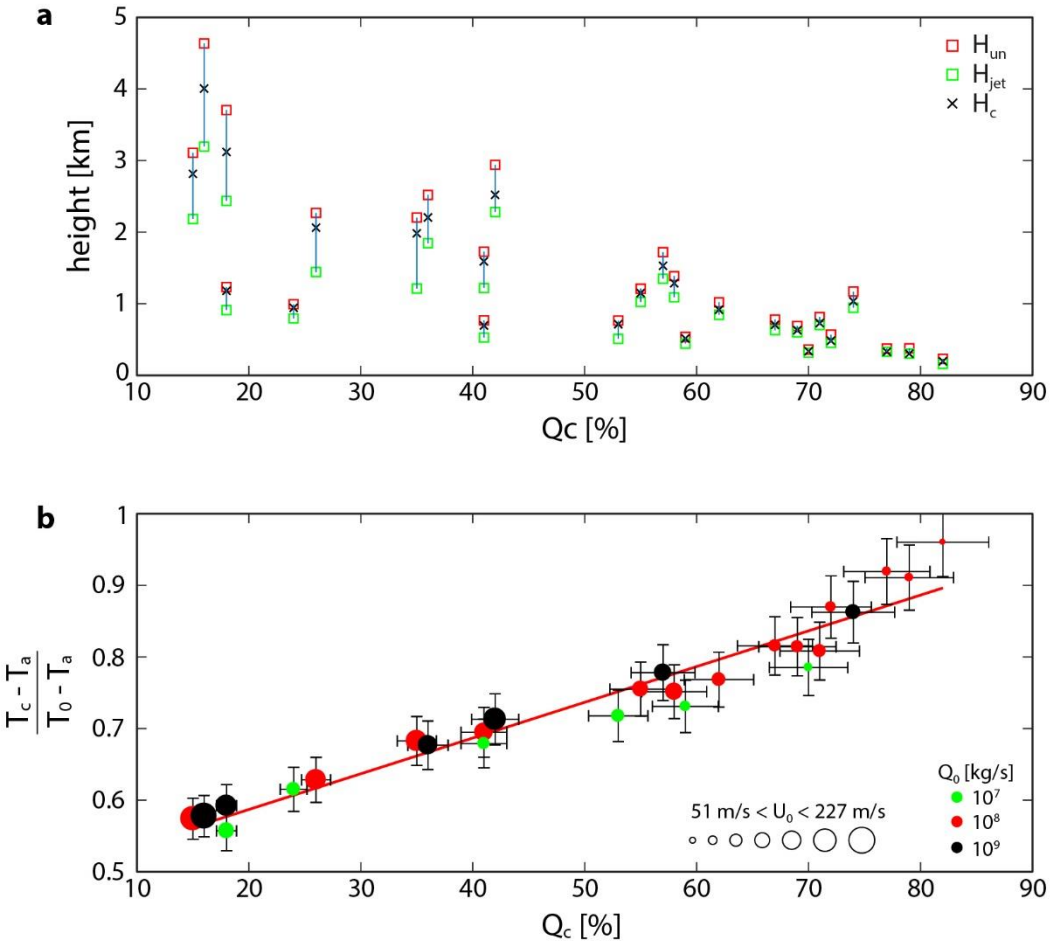

Fig. 3.3. *Summary of the numerical results.* ***a****, Characteristic heights of eruption column as a function of the percentage of collapse for all the simulated dynamics. Red squares show the height at which the mean upward momentum of the central uneroded axis is exhausted (H_{un}). Green squares show the height at which the mean upward momentum of the whole eruptive column is exhausted (H_{jet}). Black*

crosses represent the critical height at which the eruptive column starts to collapse (H_c; see Supplementary Methods). ***b****, Relationship between the percentage of collapsing mass and its corresponding temperature value normalized to the initial magmatic temperature with respect to the atmospheric air. Green, red and black dots represent the adopted mass flow rate Q_0 at the source, and their size represents the relative exit velocity U_0. The red solid line show the linear least square regression ($r_2 = 0.94$; p-value = $4.42x10^{-16}$). A 10% of error is applied due to the mesh geometry, as suggested by Cerminara et al., 2016.*

We observed a linear correlation between the percentage of collapsing mass and its corresponding temperature drop normalized to the initial magmatic temperature (Fig. 3.3B). Thus, as the collapse regime changes from a near total collapse to an incipient collapse of the eruptive column, the temperature of the mass that feeds a PDC is decreased by up to 45% of its initial magmatic value. For a given mass flow rate, an increase in the mixture upward velocity (and hence a decrease in the jet radius) produces a decrease in the percentage of collapsing mass. The correlation shown in Fig. 3.3B is observed to be relatively insensitive to the mass flow rate adopted, implying that the thermal state of PDCs at their generation is dictated by the percentage of collapse. Provided that we are herein not addressing the heat loss during PDC paths, our findings indicate that the collapsing regime has a strong influence on the initial temperature of PDCs, giving important insights for the understanding of the large variations of emplacement temperatures of PDC deposits that show little thermal loss downcurrent. Although Fig. 3.1 compares the emplacement temperature of some ignimbrites with respect to their volumes (i.e. magnitude), it can also be read in terms of eruption intensities (Pyle, 2015), i.e. mass flux. For large magnitude ignimbrite-forming eruptions it is implicit that their mass flux must invariably be high ($10^9 – 10^{10}$ kg s^{-1} for up to 28 hours in the cases of Bishop and Bandelier tuffs; Bursik and Woods, 1996), since otherwise they should be sustained for a considerable period of time, which is unlikely given the dominant to ubiquitous massive and chaotic facies that constrains their sedimentation rates to high values, in the order of several mm to cm s^{-1} (e.g. Bursik and Woods 1996, Roche et al., 2016). In contrast, ignimbrites with magnitude < 5 (bulk deposit volume < 1 km^3)

could be associated to a wide range of eruption intensities. This makes it possible to link our numerically-determined percentage of collapse, which is a dimensionless number that characterizes the total mass flow rate feeding PDCs, with the erupted volume represented by flow deposits. Extensively welded ignimbrites, as well as those above the Curie temperature, may be indicative of sustained total collapses (i.e. high percentage of collapse) from very low fountains, such for large-volume ignimbrites. Furthermore, the great thermal variability observed in PDC deposits of small-volume (≤ 1 km^3), such as those formed during sub-Plinian and Plinian eruptions, can be, at least partly, explained by a broad spectrum of collapsing regimes, from partial to total collapse, indicating the different percentage of mass introduced into a PDC. The relatively high-temperatures of PDCs formed by eruptions of magnitude < 5 may be indicative of rapid and elevated percentage of collapse of the eruptive column, with similar high, though short-lived, intensities to that of larger events. On the other hand, those currents showing lower temperature are likely to represent eruptions characterized by a low percentage of collapse that results in a low intensity (mass flux) PDC. In summary, our analysis of thermal collapsing regimes gives an interesting perspective on the potential of PDC deposits' temperatures to serve as markers for determining the percentage of collapse of past explosive eruptions and, in turn, a minimum value of their intensity.

Supplementary Fig. S3.1

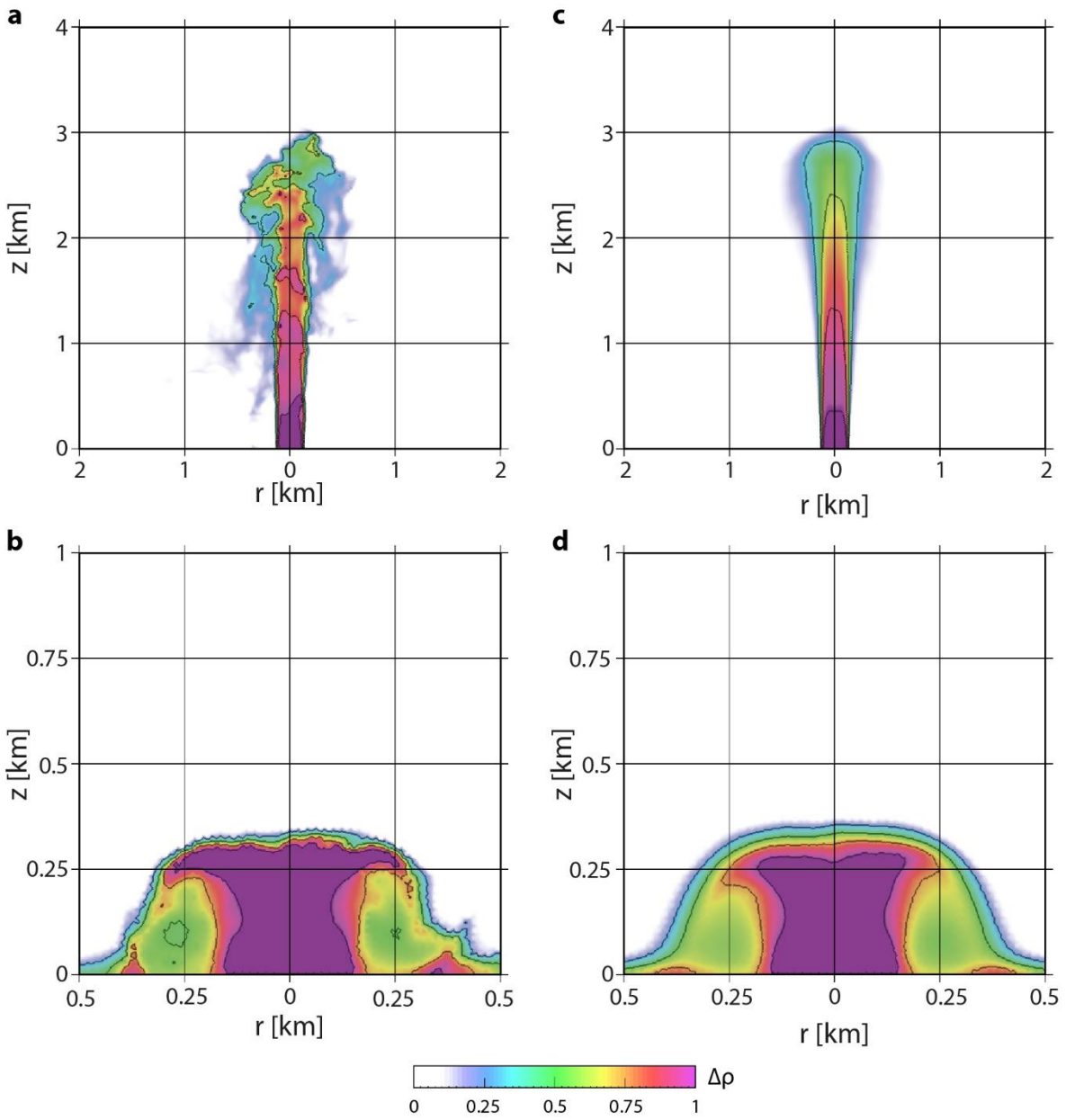

Fig. S3.1. *Comparison between the internal structures of the two column collapse end-members.* ***a-b****, Cross-sectional images showing the instantaneous distribution of the density difference relative to the stratified atmospheric density at the same vertical position normalized to the initial density, at 100 s and 315 s respectively. Isosurfaces correspond to* $\Delta\rho$ *= 0.25, 0.5, 0.75, 0.999.* ***c-d****, Same as a-b, but in a time-averaged domain. The averaging window is from 500 to 1000 s.*

3.3. Supplementary Appendix A

Eruptive scenarios investigated

For our simulation, we set the initial source conditions considering three scenarios, based on different mass eruption rate (10^7, 10^8 and 10^9 kg s^{-1}). These adopted mass flow rate of the mixture at the vent make it possible to study the continuum of regimes possibly occurring during the explosive eruption as well as different degree of mass involved into the collapse mechanisms. All simulations are carried out with a constant mass flux throughout the whole simulation time, within the same atmospheric environment assumed to be quiet and temperate standard atmosphere.

Flow conditions at the conduit exit

For every given mass flux a set of independent mixture variables have been chosen to characterize the eruptive scenario by imposing the main flow parameters at the conduit exit (*vent*), namely the magmatic temperature (T), the total water content (y_w) and the gas pressure (P) ("Independent variables" in Supplementary Table 3.1). In addition, as commonly done in volcanic flow models, we assume sonic flow (choked-flow) conditions at the conduit exit. To simplify the computation, at a first instance, we have assumed that the mass fraction of solids is much larger than that of gases (which are correct in the investigated regime, see e.g. Carcano et al., 2014), so that we can write:

$$U_v = c_{sound} \approx \sqrt{R_m T}$$

where U_v is the mixture velocity at the conduit exit, and the mixture gas constant is

$$R_m = y_w R_w$$

where R_w is the vapor gas constant (~462 J/kg/K).

Flow conditions after decompression

Above the vent, decompression of the mixture involves the formation of complex jet structures, which are largely influenced by the thermodynamic properties and by the geometry of the crater (Koyaguchi et al., 2010; Ogden, 2011; Ogden et al., 2008), and require a fine numerical grid to be resolved (Carcano et al., 2014). To overcome this difficulty, in this work we assume that the multiphase mixture has already decompressed and we compute analytically the flow conditions after decompression above the vent by assuming an adiabatic and nearly isothermal transformation (Fig. A3.1).

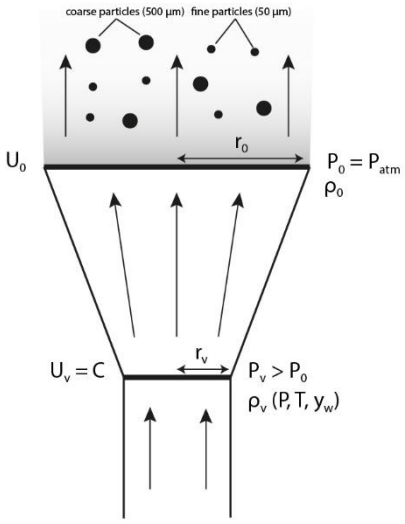

Fig. A3.1. *Schematic drawing of a volcanic jet, illustrating the definitions of the parameters before (vent region) and after decompression (inlet region) of the mixture, where U_0, ρ_0 and r_0 are the dependent source conditions of the numerical domain. The free adiabatic expansion ($P_v > P_0$) of the isothermal mixture is computed analytically, so that the jet of density ρ_0, temperature T and pressure equal to atmospheric pressure ($P_0 = P_{atm}$) rises with velocity U_0 through an inlet of radius r_0.*

In such an under-expanded jet, the flow accelerates due to the rapid adiabatic expansion. In this way, an average flow velocity U_o is calculated with the model of Woods and Bower (1995):

$$U_o = U_v + \frac{P_v - P_0}{\rho_v U_v}$$

where P_0 and P_v are the atmospheric pressure and mixture pressure at the vent, respectively, and ρ_v is the mixture density before the decompression defined by the approximate equation of state (which is reasonable for y_w>>*0.1*%) as:

$$\rho_v = \left(\frac{(1-y_w)}{\rho_s} + y_w \frac{R_w T}{P_v}\right)^{-1} \approx \frac{P_v}{y_w R_w T}$$

where ρ_s is the density of the liquid magma.

The decompression, also, leads to the decrease of the mixture density, which is calculated assuming again an isothermal mixture:

$$\rho_0 = \frac{\rho_v P_0}{P_v}$$

and an increase of the jet radius, which can be calculated as a function of the given mass eruption rate Q, velocity U_0 and density ρ_0 of the decompressed mixture:

$$r_0 = \sqrt{\frac{Q}{\pi \rho_0 U_0}}$$

Since velocity variations for pressure higher than 10 Mpa (i.e. a typical yield strength value of rocks at shallow depth) are almost steady-state (Fig. A3.2), we adopt three different mixture pressure at vent (0,1 – 0,2 and 10 MPa) to obtain the maximum and minimum interval of mixture velocity. We also assume the case of a pressure-balanced sonic flow at the conduit exit. This might represent flow conditions occurring after some time from the beginning of the eruption, in a situation of open conduit system.

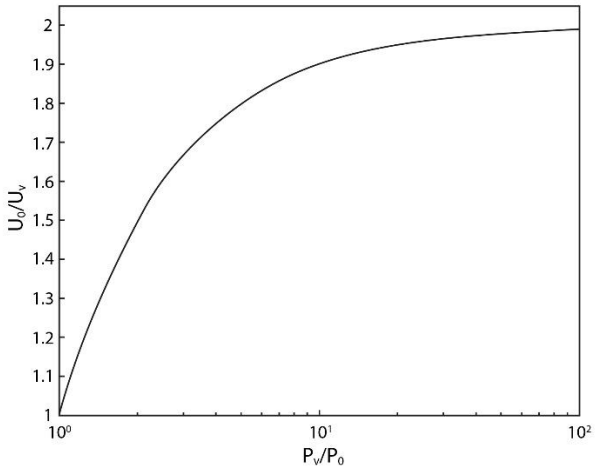

Fig. A3.2. *Variation of eruption velocity as a function of mixture pressure.*

The source parameters assumed for the simulated scenarios are listed in detail in Supplementary Table 3.1. For each simulation, the adopted flow conditions at the vent, i.e. magma temperature T, mass eruption rate Q, water content y_w, exit flow velocity U_v, mixture density ρ_v, vent radius r_v, are fixed (steady conditions). As shown in the Table, an increasing in Q leads to an enlargement of r_v, whereas U_v and ρ_v remain the same. It is also evident from Supplementary Table 3.1. that a higher y_w corresponds to higher U_v, and to a smaller ρ_v. In overpressure jet cases, the decompression above the vent increases both the inlet flow velocity U_o and the inlet radius r_0, and decreases the simulated mixture density ρ_0.

Supplementary Table 3.1
Input parameters and collapse properties

Independent variables				Dependent variables						Q_c	T_c
Q (kg/s)	T (K)	y_w (wt.%)	P (MPa)	ρ_v (kg/m^3)	U_v (m/s)	r_v (m)	ρ_0 (kg/m^3)	U_0 (m/s)	r_0 (m)	(%)	(K)
10^7	1123	0.010	0.1	19.27	72.0	47.9	19.3	72.0	47.9	70	945
10^7	1123	0.015	0.1	12.84	88.2	53.0	12.8	88.2	53.0	59	900
10^7	1123	0.020	0.1	9.637	102	56.9	9.64	102	56.9	41	877
10^7	1123	0.025	0.1	7.709	114	60.2	7.71	114	60.2	24	824
10^7	1123	0.010	0.2	38.54	72.0	33.8	19.3	108	39.1	53	889
10^7	1123	0.015	0.2	25.69	88.2	37.5	12.8	132	43.3	18	776
10^7	1123	0.020	0.2	19.27	102	40.3	9.64	153	46.5	-	-
10^7	1123	0.025	0.2	15.42	114	42.6	7.71	171	49.2	-	-
10^7	1123	0.015	10	1284	88.2	5.29	12.8	175	37.6	-	-
10^7	1123	0.025	10	770.9	114	6.02	7.71	226	42.7	-	-
10^8	1123	0.005	0.1	38.54	50.9	127	38.5	50.9	127	82	1090
10^8	1123	0.010	0.1	19.27	72.0	151	19.3	72.0	151	79	1049
10^8	1123	0.015	0.1	12.84	88.2	167	12.8	88.2	167	72	1015
10^8	1123	0.020	0.1	9.637	102	180	9.64	102	180	67	970
10^8	1123	0.025	0.1	7.709	114	190	7.71	114	190	62	931
10^8	1123	0.005	0.2	77.09	50.9	90.0	38.5	76.4	104	77	1056
10^8	1123	0.010	0.2	38.54	72.0	107	19.3	108	123	71	964
10^8	1123	0.015	0.2	25.69	88.2	118	12.8	132	137	55	920
10^8	1123	0.020	0.2	19.27	102	127	9.64	153	147	41	890
10^8	1123	0.025	0.2	15.42	114	134	7.71	171	155	26	865
10^8	1123	0.005	10	3854	50.9	12.7	38.5	101	90.3	69	969
10^8	1123	0.010	10	1927	72.0	15.1	19.3	143	107	58	917
10^8	1123	0.015	10	1284	88.2	16.7	12.8	175	118	35	880
10^8	1123	0.020	10	963	102	18.0	9.64	203	127	15	790
10^8	1123	0.025	10	771	114	19.0	7.71	226	135	-	-
10^9	1123	0.030	0.1	6.425	124	630	6.42	124	630	74	1009
10^9	1123	0.040	0.1	4.818	144	677	4.82	144	677	57	939
10^9	1123	0.050	0.1	3.855	161	716	3.85	161	716	36	925
10^9	1123	0.060	0.1	3.212	176	749	3.21	176	749	18	805
10^9	1123	0.030	0.2	12.85	124	445	6.42	187	514	42	905
10^9	1123	0.040	0.2	9.637	144	478	4.82	216	552	16	821

Q_c: percentage of collapse, T_c: mean temperature of the collapsing mass

3.4. Supplementary Appendix B

In this section, we provide a description of the methodology used to quantify the properties of the collapsing column, which represent the percentage and the temperature of the mass that collapse.

To smooth out fluctuations, all the quantities are evaluated using time-averaged fields, in the time window 500-1000 s.

Percentage of collapse

The procedure adopted to quantify the amount of mass collapsed is based on the computation of the mass flow rate across horizontal cross-sections of the *ascending column*, at different heights. The ascending column is defined as the part of the domain occupied by erupted material with vertical upward velocity ($U_z > 0$). The edge between the inside and the outside column region is detected using the mass fraction of a tracer: the threshold is set to 1% of the tracer mass fraction at the vent.

Fig. B3.1 shows the ash mass flow rate in the ascending column. When it grows, this means that some ash is entering in the ascending column. When it decreases, this means that some ash is exiting the ascending column, going to the collapse region. The first peak observed in Fig. B3.1 graphs is caused by the lower eddy forming in the collapse region (see Fig. 3.2). This eddy removes mass where the mass flow rate decreases and allows part of the collapsing mass to return into the ascending column where the mass flow rate increases. The fraction of mass lost during this process is the collapsing fraction. It can be quantified by measuring the mass flow rate emerging above the collapsing eddy.

Summarizing, the percentage of collapse is estimated as the ratio between the minimum inflection point of the integrated positive mass flow rate (given by the sum of coarse and fine particles) above the collapsing eddy and the mass flow rate adopted at the vent. The height at which this value is peaked represents the height of collapse (H_c; see black points in Fig. B3.1).

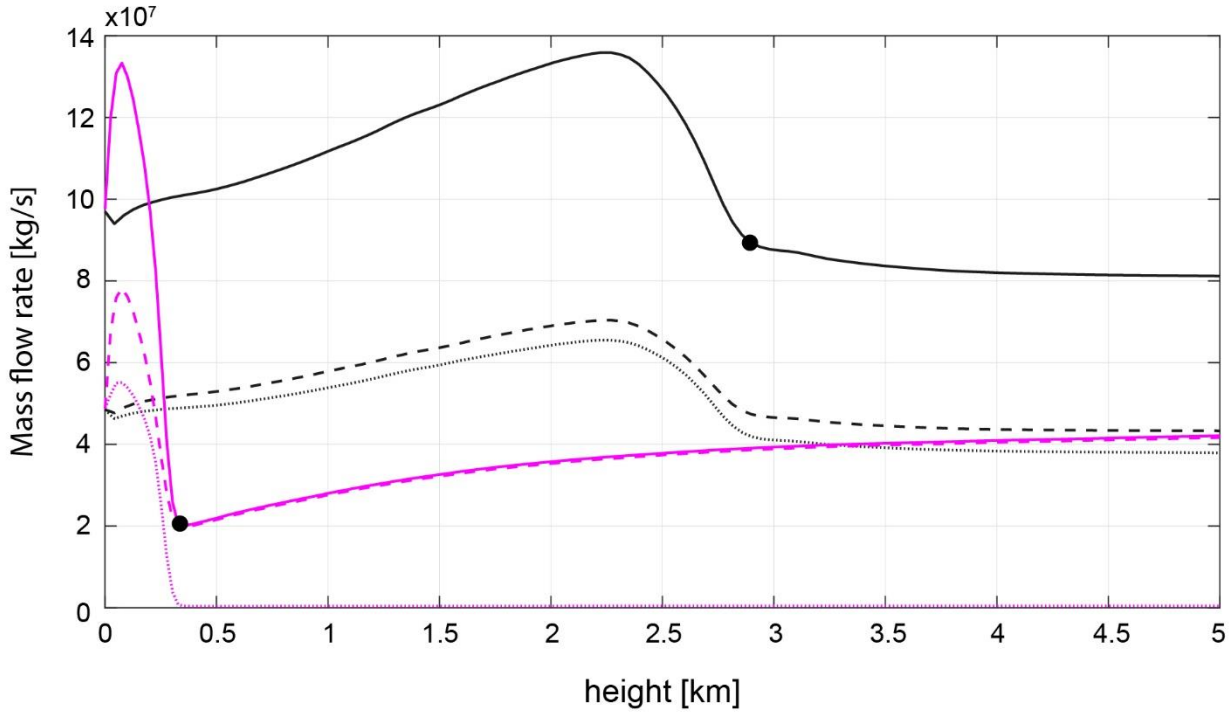

Fig. B3.1. *Mass flow rates in the ascending column integrated in time and horizontally in space. Black and pink lines are the near total collapse and incipient column collapse end-members, respectively. Solid lines represent the sum of the mass flow rate of the coarse and fine particles. Dashed and dotted lines represent the mass flow rate of the fine and coarse particles, respectively. Black point represents the height of collapse (H_c) and the mass flow rate used to estimate the percentage of collapse.*

Temperature of the collapsing mass

As we are interested in determining the mean temperature of the averaged mass that collapse from the eruptive column, we imposed different threshold to properly depict the *collapse region*. Similarly to the definition given for the ascending column, the collapse region is that part of the domain where the vertical component of the velocity is negative ($U_z < 0$), the tracer mass fraction ranges from 0.01 to 1 with respect to the vent value, and the radius is 10 times that of the inlet ($r = 10r_0$).

In this region (Fig. B3.2), we calculate the mean temperature of the collapsing mass (T_c), as the weight average of the temperature with respect to the mixture density:

$$T_c = \int_V \rho T \, dV \Big/ \int_V \rho \, dV$$

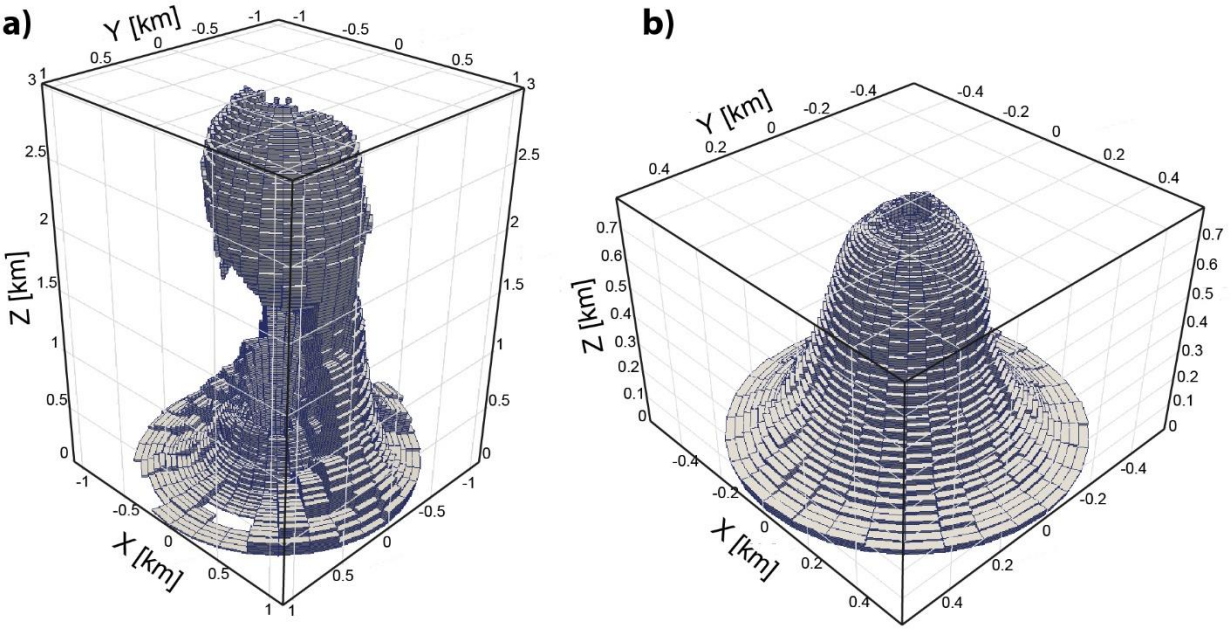

Fig. B3.2. *3D snapshot of the collapse region for the incipient collapse and the near total collapse of the eruption column (**a** and **b**, respectively).*

Supplementary Table 3.2

Emplacement temperature data

Eruption/ Location	V (km^3)	Temperatures range	Authors
29.97 Ma Tuff of Palisade Mesa	200	Welded	Best et al., 2013
24.95 Ma Clipper Gap Tuff	180	Densely welded	Best et al., 2013
35.3 Ma Pancake Summit Tuff	700	Densely welded	Best et al., 2013
26.82 Ma Hancock Tuff Member	1100	Densely welded	Best et al., 2013
26.98 Ma Coyote Summit Tuff Member	1400	Welded	Best et al., 2013
22.93 Ma Pahranagat Formation	2100	Welded	Best et al., 1995; 2013
27.57 Ma Monotony Tuff	4500	Welded	Best et al., 2013
31.69 Ma Windous Butte ignimbrite	4800	Densely welded	Best et al., 2013
0.6 Ma Lava Creek Tuff	1000	Densely welded	Christiansen, 1984; 2001
2 Ma Huckleberry Ridge Tuff	2500	Densely welded	Christiansen, 1984; 2001
0.84 Ma older Toba Tuff	~ 2500	Welded	Rose and Chesner, 1987
75 ka Toba	2800	Unwelded to welded	Rose and Chesner, 1987
29 Ma Lund Tuff	~ 3000	Welded	Maughan et al., 2002
27.8 Ma Fish Canyon Tuff	5000	Welded	Steven and Lipman, 1976
0.76 Ma Bishop Tuff	500	Welded	Sheridan, 1971; Wilson and Hildreth, 2003
274 Ma Ora	~ 1290	Welded	Willcock and Cas, 2014
2.08 Ma Cerro Galan	~ 630	≥620°C/welded	Lesti et al., 2011; Folkes et al., 2011
4.2 Ma Real Grande	510	≥600°C	Lesti et al., 2011; Folkes et al., 2011
0.45 Ma Pozzolane Rosse	60	≥630°C	Trolese et al., 2017; Giordano et al., 2010
0.40 Ma Pozzolane Nere	15	≥600°C	Trolese et al., 2017; Giordano et al., 2010
0.35 Ma Villa Senni	30	≥630°C	Trolese et al., 2017; Giordano et al., 2010
1.8 ka Taupo	30	400 – 500°C	McClelland et al., 2004
1883 Krakatau	9	475 – 550°C	Mandeville et al., 1994
1993 Lascar	0.4	≥397°C	Paterson et al., 2010; Déruelle et al., 1996
1913 Colima – F4	~ 1.1	250 – 300°C	Sulpizio et al., 2015
1913 Colima – F5	~ 1.1	280 – 330°C	Sulpizio et al., 2015
1982 El Chicón	~ 1.1	360 – 420°C	Sulpizio et al., 2015
12 June Mt. St. Helens	0.02	510 – 570°C	Paterson et al., 2010
22 July Mt. St. Helens	0.006	≥580°C	Paterson et al., 2010
18 May Mt. St. Helens - PDCs	0.12	300 – 420°C	Banks and Hoblitt, 1996
12 June Mt. St. Helens	0.02	361 – 602°C	Banks and Hoblitt, 1996
Fogo A – Pink intra-plinian ignimbrite	~ 1.2	350 – 400°C	Pensa et al., 2015
Fogo A – Black intra-plinian ignimbrite	~ 1.2	580 – 620°C	Pensa et al., 2015
Fogo A – Dark-brown ignimbrite	~ 1.2	250 – 370°C	Pensa et al., 2015
79 AD – EU2/3pf; EU3pfi	<0.1	220 – 280°C	Cioni et al., 2004
79 AD – EU3pf	<0.1	240 – 360°C	Cioni et al., 2004
79 AD – EU3pfl	<0.05	250 – 310°C	Cioni et al., 2004
79 AD – EU2/3pf	<0.1	258 – 371°C	Caricchi et al., 2014
79 AD – EU3pf	<0.1	315 – 377°C	Caricchi et al., 2014
79 AD – EU3pf	<0.1	140 – 300°C	Zanella et al., 2007
9.5 ka Mercato	~ 0.2	360 – 420°C	Zanella et al., 2015; Gurioli et al., 2010
22 ka Pomici di Base	~ 0.18	340 – 380°C	Zanella et al., 2015; Gurioli et al., 2010
1631 Vesuvius	<0.2	380 – 400°C	Zanella et al., 2015; Gurioli et al., 2010
472 AD – Pollena	<0.01	260 – 340°C	Zanella et al., 2008
18.5 ka Cape Riva breccias	~ 1	310 – 360°C	McClelland and Druitt, 1989; Druitt, 1985
79 ka Middle Pumice	~ 0.5	250 – 350°C	McClelland and Druitt, 1989; Druitt et al., 1985
21 October 1997 Monserrat – PDCs	~ 0.019	400 – 560°C	Scott and Glasspool, 2005; Cole et al., 2002
26 December 1997 Monserrat – PDCs	~ 0.09	48 – 293°C	Sparks et al., 2002
31 May 1997 Monserrat – PDCs	0.003	99 – 149°C	Cole et al., 2002
17 September 1997 Monserrat – PDCs	0.123	326°C	Cole et al., 2002
17 October 1997 Monserrat – PDCs	~ 0.019	180°C	Cole et al., 2002

Chapter 4

Overall discussion and future perspectives

PDCs undoubtedly represent one of the most destructive and dangerous phase of volcanic eruptions, due to their high temperatures (up to magmatic temperatures), rapid travel velocities (up to 300 km/h) and ability to traverse topographic barriers hundreds of meters high (Branney and Kokelaar, 2002; Druitt, 1998; Sulpizio et al., 2014). Given the widespread and devastating impacts of such currents, understanding their complex behavior is fundamental to tackle the difficult challenges of risk reduction posed by potential future eruptions. However, there are still many unknowns about the physical processes occurring within PDCs, mainly because of our inability to measure and observe their internal structure directly. Nevertheless, a deeper understanding of PDCs dynamics can still be possible through the combination of field-based analysis with numerical and analogue models. Of particular importance to volcanic hazard mitigation is the thermal evolution of PDCs, although our knowledge about the mechanism of heat transport in their interior is still limited. The thermal dynamics of these currents is thought to be influenced by many factors, including the particle concentration gradient, entrainment of ambient air, interaction with topography and generation mechanism, i.e. column collapse, dome collapse and boiling over (Bursik and Woods, 1996; Benage et al., 2016; Cioni et al., 2004; Lesti et al., 2011; Pensa et al., 2015; Sulpizio et al., 2008). Therefore, the reconstruction of the thermal architecture of PDC deposits and the study of the thermal dynamics of eruption collapsing plumes can ideally furnish essential information concerning the complex multiphase physics of PDCs, as well as an overview of their entire eruptive history, from their genesis to their emplacement.

In order to improve our current understanding of the thermal evolution of PDCs, the present thesis provides a series of detailed temperature reconstructions from PDC deposits of several case studies that encompass a broad range as: volume (from very small to several tens of cubic km), PDC

generation mechanism (column collapse and lateral dome collapse), fragmentation mechanism and related grain size distributions (magmatic vs phreatomagmatic vs dome explosion), magma chemistry (mafic to intermediate), topographic interactions (unconfined to confined). This thesis also explores numerically different column collapse regimes to quantitatively assess, for the first time, their thermal footprint on the associated PDCs. Hence, by using a multidisciplinary approach, the findings presented in this work shed light on the crucial and debated process of the heat exchange experienced by PDCs.

The present work shows that the thermal decay of a pyroclastic mixture attained during its eruptive and transport history is a non-linear process, and identifies at least two distinct thermal domains (Fig. 4.1): one in which the heat transfer between the gas-particle mixture and the external environment is substantially very limited (flow transport regime), and one in which it is potentially very efficient (eruptive mechanism).

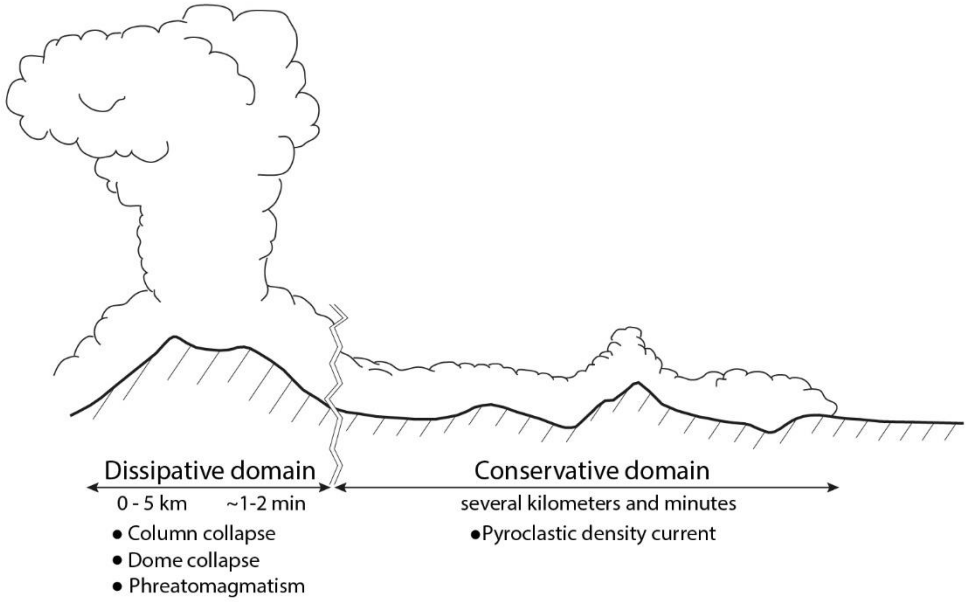

Fig. 4.1. *Schematic drawing of the macro thermal domain identified.*

Here, it has been shown that the lateral thermal gradient of all the studied PDC deposits is surprisingly homogeneous and low across their areal extents, despite their entirely different nature in terms of eruptive conditions, magma composition, lithofacies, grain size and the degree of interaction with topography. This indicates that their parental currents, or better their basal part, were able to transport and preserve the inherited thermal character from the source over their inundation area, whatever the initial temperature conditions, i.e. attained at source for different processes. Previous works have shown that the dynamics of dilute PDCs, such as the runout distance, as well as their thermal history are dependent on the entrainment efficiency (Andrews, 2014; Bursik and Woods, 1996). However, the amount and efficiency of air ingestion in the basal part of PDCs is difficult to quantify, largely because of our incomplete understanding of the complex multiphase flow rheology. The data presented here, along with other emplacement temperatures estimate reported elsewhere, reinforce the idea that within the basal bed-load region the mixing ability and cooling are broadly limited, thus resulting in an almost closed thermodynamic system. This is particularly true in case of sustained mass flux, which forces the transport of the physical properties of PDCs for several tens to hundreds of kilometers, regardless of their complex gas-particle transport regimes.

The interaction with topography has been shown to influence the dynamics of PDCs in several ways (Andrews and Manga, 2011; Bursik and Woods, 2000; Doronzo et al., 2010; Doronzo and Dellino, 2014; Giordano, 1998; Giordano and Doronzo, 2017; Komorowski et al., 2013; Sulpizio et al., 2007, 2010; Woods et al., 1998). This influence may be exerted by promoting sedimentation and increasing the efficiency of air ingestion, likely causing the reduction of the flow density and runout distance. At the same time, it may also act as a bottleneck constriction, inducing the flow to accelerate, concentrate and to propagate further. However, the data presented here suggest that the effect of flow-topography interaction on the thermal dissipation patterns is likely to be at least an order of magnitude less than the one associated with the eruptive mechanisms. It is likely, instead, that very local effects induced by urban edifices, such as the ingestion of cold walls material and the increase of the flow

turbulence, can rapidly decrease the temperature of the current by hundreds of degrees (Gurioli et al., 2005; Caricchi et al., 2014; Giordano et al., *in review*).

The evidence of a conservative PDC transport system, which has been shown here to be independent of initial temperatures (which may either be low or high), density stratifications and extent of topographic interaction, requires that the substantial thermal drop must be due to the eruptive mechanisms, and not to entrainment and mixing of ambient air as the current propagates. Indeed, the Colli Albani case study has confirmed that phreatomagmatism can significantly decrease the thermodynamic state of the erupting materials with respect to its magmatic counterpart, without, though, affecting significantly the mobility of PDCs, nor their tendency to retain the initial heat along flow. Similarly, the low temperature recorded by PDC deposits associated with the 2010 paroxysmal hot-dome explosion at Merapi suggests that the inferred blast-like event is likely responsible for the rapid thermal drop of the mixture, although such speculation need to be tested with numerical calculations.

The temperature of PDCs is thus a function of the temperature at their genesis. In this framework, an important outcome of this thesis is that different column collapse regimes (and hence different percentage of collapsing mass feeding PDCs) have a clear thermal imprint on the subsequent PDCs. Even though this dependency has been qualitatively hypothesized in previous works (Benage et al., 2016; Cioni et al., 2004; Sulpizio et al., 2014), the 3D numerical simulations presented here are used, for the first time, to quantitatively infer the temperature of the gas-particle mixture representing the PDC at its initial stage. The simulations illustrate that a temperature decrease of up to 45% occurs in case of incipient column collapse, whereas higher percentage of collapse result in temperature values close to source conditions. This finding has potential implications for explaining the huge spectrum of emplacement temperature recorded by PDC deposits. In particular, sustained high percentage of collapse (and hence high eruptive intensity) may justify the large magnitude ignimbrites (>1km^3) showing temperatures greater than the Curie temperature or features peculiar of welding. For PDC

deposits of magnitude <5 (<1km^3), the relatively high temperatures of emplacement may indicate high percentage of collapse similar to the one of larger events, but limited to a short time period. On the other hand, the low temperature of emplacement of small-volume PDC deposits could be partially attributed to a regime of incipient collapse, where the net mass flux feeding the PDCs tend to be short-lived, episodic and of low intensity. Hence, for those collapse-generated magmatic currents that show to be a thermally closed system along their path, the emplacement temperature may be an indirect estimate of the column collapse regime, and in turn, of the intensity of the eruption. However, other external processes should be invoked to justify the very low temperature showed by PDC deposits at the low end of the magnitude spectrum, such as the possible influence of magma-water interaction, which may be not enough pronounced to be clearly detected by the deposit characteristics, but sufficient to further decrease the initial temperature of the mixture.

In conclusion, this thesis shows that the primary driver of the thermal consumption occurring from the genesis to the emplacement of PDCs is represented by the mechanism of the eruptive event (i.e. column collapse, magma-water interaction and blast process), whereas the flow transport regime is less efficient (Fig. 4.1). Interestingly, such a bipartite thermal domain span over different time and length scales, where the greatest amount of mixing occurs fast (likely on the order of seconds to a few minutes) and in a restricted area.

Further questions arise from the present thesis:

How is the stratified flow transport system able to thermally insulate the basal part of the current for several tens of kilometers from the source? How does sustained vs episodic (short-lived) mass flux affect the thermal evolution?

The numerical analysis presented in this thesis was restricted to the column collapse region, aiming at verifying the initial thermal condition of the future lateral PDCs. The next direction for this work is to expand the numerical analysis to the flow transport phase. The idea is to use the output of this study as initial condition for new 3D numerical investigations, in order to elucidate the entrainment

efficiency and the thermal evolution of the multiphase gas-particle mixture (and in particular of the basal layer) along its path in case of both sustained and transient mass flux. Specifically, it would be interesting to test and compare the thermal patterns resulting from either a prolonged or episodic lateral supply of hot or relatively cold material. Such approach would help further the understanding of the transport of PDCs' properties and related hazard.

Does the gravitational collapse of the expanded mixture associated with the blast process entrain enough air to cause a substantial thermal decrease of the pyroclastic materials to produce low temperature PDCs?

The possible extremely fast cooling associated with a turbulent mixing with atmospheric air during the gravitational collapse of the blast-expanded materials need to be further examined. Recent simulations have shown that the initial rapidly expanding burst phase provides the energy for efficient magma fragmentation and acceleration of the subsequent gas-particle mixture (Esposti Ongaro et al., 2012). The generation of PDCs from the blast indicates that the decompression failed to entrain sufficient ambient air to decrease the mixture density below than atmospheric.

REFERENCES

Andrews, B.J., 2014. Dispersal and air entrainment in unconfined dilute pyroclastic density currents. Bull. Volcanol. 76, 1–14. doi:10.1007/s00445-014-0852-4

Andrews, B.J., Manga, M., 2011. Effects of topography on pyroclastic density current runout and formation of coignimbrites. Geology 39, 1099–1102. doi:10.1130/G32226.1

Ascough, P.L., Bird, M.I., Scott, A.C., Collinson, M.E., Cohen-Ofri, I., Snape, C.E., Le Manquais, K., 2010. Charcoal reflectance measurements: Implications for structural characterization and assessment of diagenetic alteration. J. Archaeol. Sci. 37, 1590–1599. doi:10.1016/j.jas.2010.01.020

Auker, M.R., Stephen, R., Sparks, J., Siebert, L., Crosweller, H.S., Ewert, J., 2013. A statistical analysis of the global historical volcanic fatalities record 1–24.

Banks, N.G., Hoblitt, R.P., 1996. Direct Temperature Measurements of Deposits, Mount St. Helens, Washington, 1980-1981.

Bardot, L., 2000. Emplacement temperature determinations of proximal pyroclastic deposits on Santorini, Greece, and their implications. Bull. Volcanol. 61, 450–467. doi:10.1007/PL00008911

Bardot, L., McClelland, E., 2000. The reliability of emplacement temperature estimates using palaeomagnetic methods: A case study from Santorini, Greece. Geophys. J. Int. 143, 39–51. doi:10.1046/j.1365-246X.2000.00186.x

Benage, M.C., Dufek, J., Mothes, P.A., 2016. Quantifying entrainment in pyroclastic density currents from the Tungurahua eruption, Ecuador: Integrating field proxies with numerical simulations 6932–6941. doi:10.1002/2016GL069527.Received

Bernard, D., Oscar Figueroa, A., Eduardo Medina, T., Jose Viramonte, G., Mario Maragaño, C., 1996. Petrology of pumices of April 1993 eruption of Lascar (Atacama, Chile). Terra Nov. 8, 191–199.

Best, M.G., Christiansen, E.H., Deino, A.L., Grommé, C.S., Tingey, D.G., 1995. Correlation and emplacement of a large, zoned, discontinuously exposed ash flow sheet: The 40Ar/39Ar chronology, paleomagnetism, and petrology of the Pahranagat Formation, Nevada. J. Geophys. Res. Solid Earth 100, 24593–24609.

Best, M.G., Gromme, S., Deino, A.L., Christiansen, E.H., Hart, G.L., Tingey, D.G., Street, C., Alto, P., 2013. The 36 – 18 Ma Central Nevada ignimbrite fi eld and calderas , Great Basin , USA : Multicyclic super-eruptions i, 1562–1636. doi:10.1130/GES00945.1

Boari, E., Avanzinelli, R., Melluso, L., Giordano, G., Mattei, M., De Benedetti, A.A., Morra, V., Conticelli, S., 2009. Isotope geochemistry (Sr-Nd-Pb) and petrogenesis of leucite-bearing volcanic rocks from “Colli albani” volcano, roman magmatic province, central Italy: Inferences on volcano evolution and magma genesis. Bull. Volcanol. 71, 977–1005. doi:10.1007/s00445-009-0278-6

Branney, M.J., Kokelaar, B.P., 2002. Pyroclastic density currents and the sedimentation of ignimbrites. Geological Society of London.

Breard, E.C.P., Lube, G., Jones, J.R., Dufek, J., Cronin, S.J., Valentine, G.A., 2016. Coupling of turbulent and non-turbulent flow regimes within pyroclastic density currents 1. doi:10.1038/NGEO2794

Bursik, M.I., Woods, A.W., 2000. The effects of topography on sedimentation from particle-laden turbulent density currents. J. Sediment. Res. 70.

Bursik, M.I., Woods, A.W., 1996. The dynamics and thermodynamics of large ash flows. Bull. Volcanol. 58, 175–193.

Carazzo, G., Jellinek, A.M., 2012. A new view of the dynamics , stability and longevity of volcanic clouds. Earth Planet. Sci. Lett. 325–326, 39–51. doi:10.1016/j.epsl.2012.01.025

Carazzo, G., Kaminski, E., Tait, S., 2015. The timing and intensity of column collapse during explosive volcanic eruptions. Earth Planet. Sci. Lett. 411, 208–217. doi:10.1016/j.epsl.2014.12.006

Carcano, S., Esposti Ongaro, T., Bonaventura, L., Neri, A., 2014. Influence of grain-size distribution on the dynamics of underexpanded volcanic jets. J. Volcanol. Geotherm. Res. 285, 60–80. doi:10.1016/j.jvolgeores.2014.08.003

Caricchi, C., Vona, A., Corrado, S., Giordano, G., Romano, C., 2014. 79AD Vesuvius PDC deposits' temperatures inferred from optical analysis on woods charred in-situ in the Villa dei Papiri at Herculaneum (Italy). J. Volcanol. Geotherm. Res. 289, 14–25. doi:10.1016/j.jvolgeores.2014.10.016

Cas, R.A.F., Wright, H.M.N., Folkes, C.B., Lesti, C., Porreca, M., Giordano, G., Viramonte, J.G., 2011. The flow dynamics of an extremely large volume pyroclastic flow, the 2.08-Ma Cerro Galán Ignimbrite, NW Argentina, and comparison with other flow types. Bull. Volcanol. 73, 1583–1609.

Cerminara, M., Esposti, T., Neri, A., 2016. Large Eddy Simulation of gas – particle kinematic decoupling and turbulent entrainment in volcanic plumes. J. Volcanol. Geotherm. Res. 326, 143–171. doi:10.1016/j.jvolgeores.2016.06.018

Cerminara, M., Esposti Ongaro, T., Berselli, L.C., 2016. ASHEE-1.0: a compressible, equilibrium-Eulerian model for volcanic ash plumes. Geosci. Model Dev. 9, 697–730.

Chadima, M., Hrouda, F., 2006. Remasoft 3.0 a user-friendly paleomagnetic data browser and analyzer. Trav. Géophysiques 27, 20–21.

Charbonnier, S.J., Gertisser, R., 2008. Field observations and surface characteristics of pristine block-and-ash fl ow deposits from the 2006 eruption of Merapi Volcano , Java , Indonesia. J. Volcanol. Geotherm. Res. 177, 971–982. doi:10.1016/j.jvolgeores.2008.07.008

Chester, D.K., Degg, M., Duncan, A.M., Guest, J.E., 2000. The increasing exposure of cities to the effects of volcanic eruptions: a global survey. Glob. Environ. Chang. Part B Environ. Hazards 2, 89–103.

Christiansen, R.L., 2001. The Quaternary and pliocene Yellowstone plateau volcanic field of Wyoming, Idaho, and Montana.

Christiansen, R.L., 1984. Yellowstone magmatic evolution: Its bearing on understanding large-volume explosive volcanism. Explos. Volcanism Inception, Evol. Hazards 84–95.

Cioni, R., Gurioli, L., Lanza, R., Zanella, E., 2004. Temperatures of the AD 79 pyroclastic density current deposits (Vesuvius, Italy). J. Geophys. Res. Solid Earth 109.

Clarke, A.B., Voight, B., 2000. Pyroclastic current dynamic pressure from aerodynamics of tree or pole blow-down. J. Volcanol. Geotherm. Res. 100, 395–412.

Clement, B.M., Connor, C.B., Graper, G., 1993. Paleomagnetic estimate of the emplacement

temperature of the long-runout Nevado de Colima volcanic debris avalanche deposit, Mexico. Earth Planet. Sci. Lett. 120, 499–510. doi:10.1016/0012-821X(93)90260-G

Cole, P.D., Calder, E.S., Sparks, R.S.J., Clarke, A.B., Druitt, T.H., Young, S.R., Herd, R.A., Harford, C.L., Norton, G.E., 2002. Deposits from dome-collapse and fountain-collapse pyroclastic flows at Soufrière Hills Volcano, Montserrat. Geol. Soc. London, Mem. 21, 231–262.

Conticelli, S., Boari, E., Avanzinelli, R., De Benedetti, A.A., Giordano, G., Mattei, M., Melluso, L., Morra, V., 2010. Geochemistry, isotopic composition and petrogenetic modelling of the Colli Albani volcanic rocks. Spec. Publ. Soc. LONDON 107–139.

Correia, M., 1974. Mesure, par leur pouvoir reflecteur, des temperatures de carbonisation des bois fossilises dans les formations volcaniques. Bull. Cent. Rech. Pau-SNPA 8, 527–536.

Costa, A., Suzuki, Y.J., Cerminara, M., Devenish, B.J., Ongaro, T.E., Herzog, M., Eaton, A.R. Van, Denby, L.C., Bursik, M., Vitturi, M.D.M., Engwell, S., Neri, A., Barsotti, S., Folch, A., Macedonio, G., Girault, F., Carazzo, G., Tait, S., Kaminski, E., Mastin, L.G., Woodhouse, M.J., Phillips, J.C., Hogg, A.J., Degruyter, W., Bonadonna, C., 2016. Results of the eruptive column model inter-comparison study. J. Volcanol. Geotherm. Res. 326, 2–25. doi:10.1016/j.jvolgeores.2016.01.017

Costa, F., Andreastuti, S., Bouvet, C., Maisonneuve, D., Pallister, J.S., 2013. Petrological insights into the storage conditions , and magmatic processes that yielded the centennial 2010 Merapi explosive eruption. J. Volcanol. Geotherm. Res. 261, 209–235. doi:10.1016/j.jvolgeores.2012.12.025

Cronin, S.J., Lube, G., Dayudi, D.S., Sumarti, S., Subrandiyo, S., 2013. Insights into the October – November 2010 Gunung Merapi eruption (Central Java , Indonesia) from the stratigraphy , volume and characteristics of its pyroclastic deposits. J. Volcanol. Geotherm. Res. 261, 244–259. doi:10.1016/j.jvolgeores.2013.01.005

De Rita, D., Giordano, G., Esposito, A., Fabbri, M., Rodani, S., 2002. Large volume phreatomagmatic ignimbrites from the Colli Albani volcano (Middle Pleistocene, Italy). J. Volcanol. Geotherm. Res. 118, 77–98. doi:10.1016/S0377-0273(02)00251-2

Di Muro, A., Neri, A., Rosi, M., 2004. Contemporaneous convective and collapsing eruptive dynamics: the transitional regime of explosive eruptions. Geophys. Res. Lett. 31.

Doronzo, D.M., 2012. Two new end members of pyroclastic density currents: Forced convection-dominated and inertia-dominated. J. Volcanol. Geotherm. Res. 219–220, 87–91. doi:10.1016/j.jvolgeores.2012.01.010

Doronzo, D.M., Dellino, P., 2013. Hydraulics of subaqueous ash flows as deduced from their deposits: 2. Water entrainment, sedimentation, and deposition, with implications on pyroclastic density current deposit emplacement. J. Volcanol. Geotherm. Res. 258, 176–186.

Doronzo, D.M., Martí, J., Dellino, P., Giordano, G., Sulpizio, R., 2016. Dust storms, volcanic ash hurricanes, and turbidity currents: physical similarities and differences with emphasis on flow temperature. Arab. J. Geosci. 9, 290.

Doronzo, D.M., Valentine, G.A., Dellino, P., de Tullio, M.D., 2010. Numerical analysis of the effect of topography on deposition from dilute pyroclastic density currents. Earth Planet. Sci. Lett. 300, 164–173. doi:10.1016/j.epsl.2010.10.003

Druitt, T.H., 1998. Pyroclastic density currents. Geol. Soc. London, Spec. Publ. 145, 145–182.

Druitt, T.H., 1985. Vent evolution and lag breccia formation during the Cape Riva eruption of

Santorini, Greece. J. Geol. 93, 439–454.

Druitt, T.H., Calder, E.S., Cole, P.D., Hoblitt, R.P., Loughlin, S.C., Norton, G.E., Ritchie, L.J., Sparks, R.S.J., Voight, B., 2002. Small-volume, highly mobile pyroclastic flows formed by rapid sedimentation from pyroclastic surges at Soufrière Hills Volcano, Montserrat: an important volcanic hazard. Geol. Soc. London, Mem. 21, 263–279. doi:10.1144/GSL.MEM.2002.021.01.12

Druitt, T.H., Kokelaar, B.P., 2002. The eruption of Soufrière Hills volcano, Montserrat, from 1995 to 1999. Geological Society of London.

Dufek, J., 2016. The Fluid Mechanics of Pyroclastic Density Currents 459–485. doi:10.1146/annurev-fluid-122414-034252

Dunlop, D.J., Özdemir, Ö., 2001. Rock magnetism: fundamentals and frontiers. Cambridge university press.

Eaton, A.R. Van, Wilson, C.J.N., 2013. The nature, origins and distribution of ash aggregates in a large-scale wet eruption deposit: Oruanui, New Zealand. J. Volcanol. Geotherm. Res. 250, 129–154. doi:10.1016/j.jvolgeores.2012.10.016

Esposti Ongaro, T., Clarke, A.B., Voight, B., Neri, A., Widiwijayanti, C., 2012. Multiphase flow dynamics of pyroclastic density currents during the May 18, 1980 lateral blast of Mount St. Helens. J. Geophys. Res. Solid Earth 117, 1–22. doi:10.1029/2011JB009081

Esposti Ongaro, T., Neri, A., Menconi, G., de'Michieli Vitturi, M., Marianelli, P., Cavazzoni, C., Erbacci, G., Baxter, P.J., 2008. Transient 3D numerical simulations of column collapse and pyroclastic density current scenarios at Vesuvius. J. Volcanol. Geotherm. Res. 178, 378–396. doi:10.1016/j.jvolgeores.2008.06.036

Fardila, D., 2013. Floristic Composition of Groundcover Vegetation after the 2010 Pyroclastic Fire on Mount Merapi XIX, 85–93. doi:10.7226/jtfm.19.2.85

Fisher, R., 1953. Dispersion on a sphere, in: Proceedings of the Royal Society of London A: Mathematical, Physical and Engineering Sciences. The Royal Society, pp. 295–305.

Folkes, C.B., Wright, H.M., Cas, R.A.F., de Silva, S.L., Lesti, C., Viramonte, J.G., 2011. A re-appraisal of the stratigraphy and volcanology of the Cerro Galán volcanic system, NW Argentina. Bull. Volcanol. 73, 1427–1454.

Funiciello, R., Giordano, G., De Rita, D., 2003. The Albano maar lake (Colli Albani Volcano, Italy): Recent volcanic activity and evidence of pre-Roman Age catastrophic lahar events. J. Volcanol. Geotherm. Res. 123, 43–61. doi:10.1016/S0377-0273(03)00027-1

Genareau, K., Cronin, S.J., Lube, G., 2015. Effects of volatile behaviour on dome collapse and resultant pyroclastic surge dynamics : Gunung Merapi 2010 eruption 199–218.

Giordano, D., Russell, J.K., Dingwell, D.B., 2008. Viscosity of magmatic liquids: A model. Earth Planet. Sci. Lett. 271, 123–134. doi:10.1016/j.epsl.2008.03.038

Giordano, G., 1998. The effect of paleotopography on lithic distribution and facies associations of small volume ignimbrites: The WTT Cupa (Roccamonfina volcano, Italy). J. Volcanol. Geotherm. Res. 87, 255–273. doi:10.1016/S0377-0273(98)00096-1

Giordano, G., Doronzo, D.M., 2017. Sedimentation and mobility of PDCs: a reappraisal of ignimbrites' aspect ratio. Scientific Reports. 1–7. doi:10.1038/s41598-017-04880-6

Giordano, G., Benedetti, A.A.D.E., Diana, A., Diano, G., Esposito, A., Fabbri, M., Gaudioso, F.,

Marasco, F., Mazzini, I., Miceli, M., 2010. Stratigraphy, volcano tectonics and evolution of the Colli Albani volcanic field. In: Funiciello, R., Giordano, G. (Eds.), The Colli Albani Volcano Special Publication of IAVCEI 3. The Geological Society, London, pp. 43-97.

Giordano, G., De Benedetti, A.A., Diana, A., Diano, G., Gaudioso, F., Marasco, F., Miceli, M., Mollo, S., Cas, R.A.F., Funiciello, R., 2006. The Colli Albani mafic caldera (Roma, Italy): Stratigraphy, structure and petrology. J. Volcanol. Geotherm. Res. 155, 49–80. doi:10.1016/j.jvolgeores.2006.02.009

Giordano, G., Dobran, F., 1994. Computer simulations of the Tuscolano Artemisio's second pyroclastic flow unit (Alban Hills, Latium, Italy). J. Volcanol. Geotherm. Res. 61, 69–94. doi:10.1016/0377-0273(94)00013-1

Gurioli, L., Houghton, B.F., Cashman, K. V, Cioni, R., 2005. Complex changes in eruption dynamics during the 79 AD eruption of Vesuvius. Bull. Volcanol. 67, 144–159.

Gurioli, L., Sulpizio, R., Cioni, R., Sbrana, A., Santacroce, R., Luperini, W., Andronico, D., 2010. Pyroclastic flow hazard assessment at Somma–Vesuvius based on the geological record. Bull. Volcanol. 72, 1021–1038.

Harrison, R.J., Feinberg, J.M., 2008. FORCinel: An improved algorithm for calculating first-order reversal curve distributions using locally weighted regression smoothing. Geochemistry, Geophys. Geosystems 9. doi:10.1029/2008GC001987

Hoblitt, R.P., Miller, C.D., Vallance, J.W., 1981. Origin and stratigraphy of the deposit produced by the May 18 directed blast. US Geol. Surv. Prof. Pap 1250, 401–420.

Hudspith, V.A., Scott, A.C., Wilson, C.J.N., Collinson, M.E., 2010. Charring of woods by volcanic processes: An example from the Taupo ignimbrite, New Zealand. Palaeogeogr. Palaeoclimatol. Palaeoecol. 291, 40–51. doi:10.1016/j.palaeo.2009.06.036

Jenkins, S., Komorowski, J., Baxter, P.J., Spence, R., Picquout, A., Lavigne, F., 2013. The Merapi 2010 eruption : An interdisciplinary impact assessment methodology for studying pyroclastic density current dynamics. J. Volcanol. Geotherm. Res. 261, 316–329. doi:10.1016/j.jvolgeores.2013.02.012

Karner, D.B., Marra, F., Renne, P.R., 2001. The history of the Monti Sabatini and Alban Hills volcanoes: groundwork for assessing volcanic-tectonic hazards for Rome. J. Volcanol. Geotherm. Res. 107, 185–215. doi:10.1016/S0377-0273(00)00258-4

Kelfoun, K., Legros, F., Gourgaud, A., 2000. A statistical study of trees damaged by the 22 November 1994 eruption of Merapi volcano (Java, Indonesia): relationships between ash-cloud surges and block-and-ash flows. J. Volcanol. Geotherm. Res. 100, 379–393.

Kent, D. V, Ninkovich, D., Pescatore, T., Sparks, S.R.J., 1981. Palaeomagnetic determination of emplacement temperature of Vesuvius AD 79 pyroclastic deposits. Nature 290, 393–396.

Komorowski, J.C., Jenkins, S., Baxter, P.J., Picquout, A., Lavigne, F., Charbonnier, S., Gertisser, R., Preece, K., Cholik, N., Budi-Santoso, A., Surono, 2013. Paroxysmal dome explosion during the Merapi 2010 eruption: Processes and facies relationships of associated high-energy pyroclastic density currents. J. Volcanol. Geotherm. Res. 261, 260–294. doi:10.1016/j.jvolgeores.2013.01.007

Koyaguchi, T., Woods, A.W., 1996. On the formation of eruption columns following explosive mixing of magma and surface-water. J. Geophys. Res. 101, 5561. doi:10.1029/95JB01687

Koyaguchi, T., Suzuki, Y.J., Kozono, T., 2010. Effects of the crater on eruption column dynamics. J.

Geophys. Res. Solid Earth 115.

Lacroix, A., 1904. La Montagne Pelée et ses éruptions. Masson.

Lesti, C., Porreca, M., Giordano, G., Mattei, M., Cas, R.A.F., Wright, H.M.N., Folkes, C.B., Viramonte, J., 2011. High-temperature emplacement of the Cerro Galán and Toconquis Group ignimbrites (Puna plateau, NW Argentina) determined by TRM analyses. Bull. Volcanol. 73, 1535–1565. doi:10.1007/s00445-011-0536-2

Lube, G., Breard, E.C.P., Cronin, S.J., Jones, J., 2015. Synthesizing large-scale pyroclastic flows: Experimental design, scaling, and first results from PELE. J. Geophys. Res. Solid Earth 1–16. doi:10.1002/2014JB011666.

Mandeville, C.W., Carey, S., Sigurdsson, H., King, J., 1994. Paleomagnetic evidence for high-temperature emplacement of the 1883 subaqueous pyroclastic flows from Krakatau volcano, Indonesia. J. Geophys. Res. 99, 9487–9504. doi:10.1029/94JB00239

Marra, F., Karner, D.B., Freda, C., Gaeta, M., Renne, P., 2009. Large mafic eruptions at Alban Hills Volcanic District (Central Italy): Chronostratigraphy, petrography and eruptive behavior. J. Volcanol. Geotherm. Res. 179, 217–232. doi:10.1016/j.jvolgeores.2008.11.009

Marti, J., Diez-Gil, J.L., Ortiz, R., 1991. Conduction model for the thermal influence of lithic clasts in mixtures of hot gases and ejecta. J. Geophys. Res. Solid Earth 96, 21879–21885.

Mattei, M., Conticelli, S., Giordano, G., 2010. The Tyrrhenian margin geological setting: from the Apennine orogeny to the K-rich volcanism. Colli Albani volcano. Spec. Publ. IAVCEI 3, 7–27.

Maughan, L.L., Christiansen, E.H., Best, M.G., Deino, A.L., Tingey, D.G., Gromme, C.S., 2002. The Oligocene Lund Tuff, Great Basin, USA: a very large volume monotonous intermediate. J. Volcanol. Geotherm. Res. 113, 129 - 157.

McClelland, E.A., Druitt, T.H., 1989. Palaeomagnetic estimates of emplacement temperatures of pyroclastic deposits on Santorini, Greece. Bull. Volcanol. 51, 16–27.

McClelland, E., Wilson, C.J.N., Bardot, L., 2004. Palaeotemperature determinations for the 1.8-ka Taupo ignimbrite, New Zealand, and implications for the emplacement history of a high-velocity pyroclastic flow. Bull. Volcanol. 66, 492–513. doi:10.1007/s00445-003-0335-5

Mcparland, L.C., Collinson, M.E., Scott, A.C., Campbell, G., 2009. The use of reflectance values for the interpretation of natural and anthropogenic charcoal assemblages 249–261. doi:10.1007/s12520-009-0018-z

Newhall, C., Punongbayan, R.S., 1993. Help wanted. Nature 364, 568.

Ogden, D.E., Glatzmaier, G.A., Wohletz, K.H., 2008. Effects of vent overpressure on buoyant eruption columns: implications for plume stability. Earth Planet. Sci. Lett. 268, 283–292.

Ogden, D., 2011. Fluid dynamics in explosive volcanic vents and craters. Earth Planet. Sci. Lett. 312, 401–410.

Palladino, D., Gaeta, M., Marra, F., 2001. A large K-foiditic hydromagmatic eruption from the early activity of the Alban Hills Volcanic District, Italy. Bull. Volcanol. 63, 345–359.

Pallister, J.S., Schneider, D.J., Griswold, J.P., Keeler, R.H., Burton, W.C., Noyles, C., Newhall, C.G., Ratdomopurbo, A., 2013. Merapi 2010 eruption — Chronology and extrusion rates monitored with satellite radar and used in eruption forecasting. J. Volcanol. Geotherm. Res. 261, 144–152. doi:10.1016/j.jvolgeores.2012.07.012

Paterson, G.A., Roberts, A.P., Mac Niocaill, C., Muxworthy, A.R., Gurioli, L., Viramonté, J.G., Navarro, C., Weider, S., 2010. Paleomagnetic determination of emplacement temperatures of pyroclastic deposits: An under-utilized tool. Bull. Volcanol. 72, 309–330. doi:10.1007/s00445-009-0324-4

Paterson, R.R.M., 2006. Ganoderma – A therapeutic fungal biofactory 67, 1985–2001. doi:10.1016/j.phytochem.2006.07.004

Pensa, A., Giordano, G., Cas, R.A.F., Porreca, M., 2015. Thermal state and implications for eruptive styles of the intra-Plinian and climactic ignimbrites of the 4.6 ka Fogo A eruption sequence, São Miguel, Azores. Bull. Volcanol. 77, 99.

Pensa, A., Porreca, M., Corrado, S., Giordano, G., Cas, R., 2015. Calibrating the pTRM and charcoal reflectance (Ro%) methods to determine the emplacement temperature of ignimbrites: Fogo A sequence, São Miguel, Azores, Portugal, as a case study. Bull. Volcanol. 77, 18.

Petrovský, E.D., Kapička, A., 2006. On determination of the Curie point from thermomagnetic curves. J. Geophys. Res. Solid Earth 111, 1–10. doi:10.1029/2006JB004507

Pike, C.R., Roberts, A.P., Verosub, K.L., 1999. Characterizing interactions in fine magnetic particle systems using first order reversal curves. J. Appl. Phys. 85, 6660–6667. doi:10.1063/1.370176

Pittari, A., Cas, R.A.F., Monaghan, J.J., Martí, J., 2007. Instantaneous dynamic pressure effects on the behaviour of lithic boulders in pyroclastic flows: The Abrigo Ignimbrite, Tenerife, Canary Islands. Bull. Volcanol. 69, 265–279. doi:10.1007/s00445-006-0072-7

Porreca, M., Giordano, G., Mattei, M., Musacchio, P., 2006. Evidence of two Holocene phreatomagmatic eruptions at Stromboli volcano (Aeolian Islands) from paleomagnetic data. Geophys. Res. Lett. 33, 1–6. doi:10.1029/2006GL027575

Porreca, M., Mattei, M., MacNiocaill, C., Giordano, G., McClelland, E., Funiciello, R., 2008. Paleomagnetic evidence for low-temperature emplacement of the phreatomagmatic Peperino Albano ignimbrite (Colli Albani volcano, Central Italy). Bull. Volcanol. 70, 877–893. doi:10.1007/s00445-007-0176-8

Rader, E., Geist, D., Geissman, J., Dufek, J., Harpp, K., 2015. Hot clasts and cold blasts: thermal heterogeneity in boiling-over pyroclastic density currents. Geol. Soc. London, Spec. Publ. 396, 67–86. doi:10.1144/SP396.16

Roberts, a. P.A.P., Pike, C.R., Verosub, K.L.K.L., 2000. First-order reversal curve diagrams: A new tool for characterizing the magnetic properties of natural samples. J. Geophys. Res. 105, 461–28. doi:10.1029/2000JB900326

Roche, O., Buesch, D.C., Valentine, G.A., 2016. Slow-moving and far-travelled dense pyroclastic flows during the Peach Spring super-eruption. Nat. Commun. 7, 10890. doi:10.1038/ncomms10890

Rose, W.I., Chesner, C.A., 1985. Dispersal of ash in the great Toba eruption, 75 ka. 913–917.

Scott, A.C., Glasspool, I.J., 2007. Observations and experiments on the origin and formation of inertinite group macerals 70, 53–66. doi:10.1016/j.coal.2006.02.009

Scott, A.C., Glasspool, I.J., 2005. Charcoal reflectance as a proxy for the emplacement temperature of pyroclastic flow deposits. Geology 33, 589–592. doi:10.1130/G21474.1

Scott, A.C., Jones, T.P., 1994. The nature and influence of fire in Carboniferous ecosystems. Palaeogeogr. Palaeoclimatol. Palaeoecol. 106, 91–112.

Scott, A.C., Jones, T.P., 1991. Fossil charcoal: a plant-fossil record preserved by fire. Geol. Today 7, 214–216.

Scott, A.C., Sparks, R.S.J., Bull, I.D., Knicker, H., Evershed, R.P., 2008. Temperature proxy data and their significance for the understanding of pyroclastic density currents. Geology 36, 143–146. doi:10.1130/G24439A.1

Sparks, R.S.J., Barclay, J., Calder, E.S., Herd, R. a., Komorowski, J.-C., Luckett, R., Norton, G.E., Ritchie, L.J., Voight, B., Woods, a. W., 2002. Generation of a debris avalanche and violent pyroclastic density current on 26 December (Boxing Day) 1997 at Soufriere Hills Volcano, Montserrat. Geol. Soc. London, Mem. 21, 409–434. doi:10.1144/GSL.MEM.2002.021.01.18

Steven, T.A., Lipman, P.W., 1975. Calderas of the San Juan volcanic field, southwestern Colorado. US Govt. Print. Off.,.

Sulpizio, R., Bonasia, R., Dellino, P., Mele, D., Di Vito, M.A., La Volpe, L., 2010. The Pomici di Avellino eruption of Somma–Vesuvius (3.9 ka BP). Part II: sedimentology and physical volcanology of pyroclastic density current deposits. Bull. Volcanol. 72, 559–577.

Sulpizio, R., Mele, D., Dellino, P., La Volpe, L., 2007. Deposits and physical properties of pyroclastic density currents during complex Subplinian eruptions: The AD 472 (Pollena) eruption of Somma-Vesuvius, Italy. Sedimentology 54, 607–635. doi:10.1111/j.1365-3091.2006.00852.x

Sulpizio, R., Zanella, E., Macías, J.L., 2008. Deposition temperature of some PDC deposits from the 1982 eruption of El Chichon volcano (Chiapas, Mexico) inferred from rock-magnetic data. J. Volcanol. Geotherm. Res. 175, 494–500.

Sulpizio, R., Zanella, E., Macías, J.L., Saucedo, R., 2015. Deposit temperature of pyroclastic density currents emplaced during the El Chichon 1982 and Colima 1913 eruptions. Geol. Soc. London, Spec. Publ. 396, 35–49. doi:10.1144/sp396.5

Suzuki, Y.J., Costa, A., Cerminara, M., Ongaro, T.E., Herzog, M., Eaton, A.R. Van, Denby, L.C., 2016. Inter-comparison of three-dimensional models of volcanic plumes. J. Volcanol. Geotherm. Res. 326, 26–42. doi:10.1016/j.jvolgeores.2016.06.011

Suzuki, Y.J., Iguchi, M., 2017. Determination of the mass eruption rate for the 2014 Mount Kelud eruption using three-dimensional numerical simulations of volcanic plumes. J. Volcanol. Geotherm. Res.

Suzuki, Y.J., Koyaguchi, T., 2012. 3-D numerical simulations of eruption column collapse : Effects of vent size on pressure-balanced jet / plumes. J. Volcanol. Geotherm. Res. 221–222, 1–13. doi:10.1016/j.jvolgeores.2012.01.013

Suzuki, Y.J., Koyaguchi, T., 2010. Numerical determination of the efficiency of entrainment in volcanic eruption columns 37, 1–4. doi:10.1029/2009GL042159

Trolese, M., Giordano, G., Cifelli, F., Winkler, A., Mattei, M., 2017. Forced transport of thermal energy in magmatic and phreatomagmatic large volume ignimbrites : Paleomagnetic evidence from the Colli Albani volcano , Italy. Earth Planet. Sci. Lett. 478, 179–191. doi:10.1016/j.epsl.2017.09.004

Uehara, D., Cas, R.A.F., Folkes, C., Takarada, S., Oda, H., Porreca, M., 2015. Using thermal remanent magnetisation (TRM) to distinguish block and ash flow and debris flow deposits, and to estimate their emplacement temperature: 1991-1995 lava dome eruption at Mt. Unzen Volcano, Japan. J. Volcanol. Geotherm. Res. 303, 92–111. doi:10.1016/j.jvolgeores.2015.07.019

Van Bemmelen, R.W., 1949. Report on the volcanic activity and volcanological research in Indonesia during the period 1936–1948. Bull. Volcanol. 9, 3–29.

van Otterloo, J., Cas, R.A.F., 2016. Low-temperature emplacement of phreatomagmatic pyroclastic flow deposits at the monogenetic Mt Gambier Volcanic Complex, South Australia, and their relevance for understanding some deposits in diatremes. J. Geol. Soc. London. jgs2015-122. doi:10.1144/jgs2015-122

Voight, B., Davis, M.J., 2000. Emplacement temperatures of the November 22, 1994 nuee ardente deposits, Merapi Volcano, Java. J. Volcanol. Geotherm. Res. 100, 371–377. doi:10.1016/S0377-0273(00)00146-3

Walker, G.P.L., 1983. Ignimbrite types and ignimbrite problems. J. Volcanol. Geotherm. Res. 17, 65–88.

Watkins, S.D., Giordano, G., Cas, R.A.F., De Rita, D., 2002. Emplacement processes of the mafic Villa Senni Eruption Unit (VSEU) ignimbrite succession, Colli Albani volcano, Italy. J. Volcanol. Geotherm. Res. 118, 173–203. doi:10.1016/S0377-0273(02)00256-1

Willcock, M.A.W., Cas, R.A.F., 2014. Primary welding and crystallisation textures preserved in the intra-caldera ignimbrites of the Permian Ora Formation , northern Italy : implications for deposit thermal state and cooling history. doi:10.1007/s00445-014-0819-5

Wilson, C.J.N., 2001. The 26.5 ka Oruanui eruption, New Zealand: An introduction and overview, Journal of Volcanology and Geothermal Research. doi:10.1016/S0377-0273(01)00239-6

Wilson, C.J.N., Hildreth, W., 2003. Assembling an ignimbrite: mechanical and thermal building blocks in the Bishop Tuff, California. J. Geol. 111, 653–670.

Woods, A.W., Bower, S.M., 1995. The decompression of volcanic jets in a crater during explosive volcanic eruptions.

Woods, A.W., Bursik, M.I., Kurbatov, A. V, 1998. The interaction of ash flows with ridges. Bull. Volcanol. 60, 38–51.

Woods, W., 1995. The dynamics of explosive volcanic eruptions. Reviews of Geophysics. 495–530.

Zanella, E., Gurioli, L., Lanza, R., Sulpizio, R., Bontempi, M., 2008. Deposition temperature of the AD 472 Pollena pyroclastic density current deposits, Somma-Vesuvius, Italy. Bull. Volcanol. 70, 1237–1248. doi:10.1007/s00445-008-0199-9

Zanella, E., Sulpizio, R., Gurioli, L., Lanza, R., 2015. Temperatures of the pyroclastic density currents deposits emplaced in the last 22 kyr at Somma-Vesuvius (Italy). Geol. Soc. London, Spec. Publ. 396, 13–33. doi:10.1144/sp396.4

Zijderveld, J.D.A., 1967. AC demagnetization of rocks: analysis of results. Methods Paleomagn. 1, 254–286.